

Doctoral dissertation

Optical sub-diffraction microscopy of the glycine receptor $\alpha 3$ in the plasma membrane

Doctoral dissertation submitted to obtain the degrees of

- Doctor of Biomedical Science at Hasselt University / transnational University Limburg
- Doctor of Sciences: Chemistry (PhD) at K.U.Leuven

to be defended by:

Kristof Notelaers

Promoters: Prof. Dr Marcel Ameloot | Hasselt University /
transnational University Limburg

Prof. Dr Johan Hofkens | K.U.Leuven

Co-promoter: Prof. Dr Jean-Michel Rigo | Hasselt University /
transnational University Limburg

Members of the jury

Prof. Dr. I. Lambrichts , Universiteit Hasselt, Diepenbeek, Belgium	Chairman
Prof. Dr. M. Ameloot , Universiteit Hasselt, Diepenbeek, Belgium	Promoter
Prof. Dr. J. Hofkens , Katholieke Universiteit Leuven, Leuven, Belgium	Promoter
Prof. Dr. J.-M. Rigo , Universiteit Hasselt, Diepenbeek, Belgium	Co-promoter
Prof. Dr. H. Mizuno , Katholieke Universiteit Leuven, Leuven, Belgium	
Prof. Dr. B. Brône , Universiteit Hasselt, Diepenbeek, Belgium	
Prof. Dr. L. Michiels , Universiteit Hasselt, Diepenbeek, Belgium	
Prof. Dr. J. Meier , Max Delbrück Center for Molecular Medicine, Berlin, Germany	
Prof. Dr. T. Gensch , Forschungszentrum Jülich, Jülich, Germany	
Prof. Dr. F. Ramaekers , Maastricht University, Maastricht, The Netherlands	

Preface

The physics of biology studied through chemistry. No single phrase can better describe the multidisciplinary research approach underlying the work presented in this dissertation. From a personal point of view, this story is told by a molecular biologist balancing on a wire. That wire is strung between the rapidly evolving fields of neuronal membrane biology and advanced fluorescence microscopy. With the help of other contemporary science acrobats and those who have gone before me, I sought to form an interdisciplinary bridge. In order to explain the disciplinary scope of my work, I will introduce the different research groups involved in the conception of the project.

All starts with the biophysics group of Professor Ameloot (UHasselt), which studies the properties of proteins in the plasma membrane of the cell. An interesting family of membrane proteins are the cys-loop ligand-gated ion channels, of which the inhibitory GABA and glycine receptors (GlyR) are the main topic of the electrophysiology group of Professor Rigo (UHasselt). Through the contacts between Professor Rigo and Professor Meier (Max Delbrück Center for Molecular Medicine), the GlyR $\alpha 3$ was introduced in the context of RNA splicing and hyperexcitability disorders. The study of GlyR $\alpha 3$ membrane properties, using previously established ensemble average fluorescence techniques, was lead by Doctor Nick Smisdom in Professor Ameloot's group. However, in the last decade, optical sub-diffraction microscopy has become an important tool for studying membrane proteins. It was the intention of Professor Ameloot to integrate this tool into the GlyR research, through collaboration with the photo-chemistry group of Professor Hofkens (KULeuven). The KULeuven group possess the necessary equipment and expertise for optical sub-diffraction microscopy and our 4 year collaboration culminates in this thesis.

The thesis is a composition of three original publications (references 324, 388 and 395), preceded by an introduction and followed by a general discussion. Given that each publication inherently contains an introduction, methodology and discussion, an effort was made to avoid repetition. The preceding introduction aims to convey an integrated view of membrane topology, to address the rudimentary molecular biology of the GlyR and to introduce localization based optical sub-diffraction microscopy. Topics and procedures

extensively explained in the publications are concisely mentioned. The general discussion first handles the application and conclusions of the applied experimental strategies and thereafter their implications are discussed in the biological context of the GlyR. The perspective of the general discussion transcends the individual publications and combines all findings. Subsequently, an elaborate section is devoted to the future perspectives. This item has received little mention in the publications, yet much preliminary work towards their realization has been performed. Finally, the conclusion offers a summary of the achievements and implications of this work.

Table of content

1	Introduction	1
1.1	The cellular plasma membrane	2
1.1.1	Architecture of the cellular plasma membrane	2
1.1.2	Plasma membrane heterogeneity	3
1.1.3	Brownian motion and diffusion	6
1.1.4	Diffusion in the plasma membrane	7
1.2	The glycine receptor, a ligand-gated ion channel	10
1.2.1	The glycine receptor subunits and stoichiometry	11
1.2.2	Glycine receptor membrane dynamics	12
1.2.3	Glycine receptor $\alpha 3$	14
1.3	Single particle optical localization microscopy	17
1.3.1	Localizing and tracking single particles	19
1.3.2	Analysis of single particle trajectories	21
1.3.3	Localization based super-resolution imaging	22
1.3.4	Photoswitching of conventional synthetic fluorophores	23
1.3.5	Analysis of super-resolution images	24
1.4	Research question and hypotheses	27
2	Ensemble and single particle fluorimetric techniques in concerted action to study the diffusion and aggregation of the glycine receptor $\alpha 3$ isoforms in the cell plasma membrane	29
2.1	Abstract	30
2.2	Introduction	31
2.3	Materials and Methods	34
2.3.1	Cell culture	34
2.3.2	Transfection	34
2.3.3	Labeling of exogenous GlyRs	34
2.3.4	Image correlation spectroscopy	35
2.3.5	Direct stochastic optical reconstruction microscopy	35
2.3.6	Fluorescence recovery after photobleaching	36

2.3.7	Raster image correlation spectroscopy	37
2.3.8	Temporal image correlation spectroscopy	37
2.3.9	Single particle tracking	38
2.4	Results	39
2.4.1	GlyR $\alpha 3$ aggregation state	39
2.4.2	Study of GlyR $\alpha 3$ diffusion using ensemble techniques	41
2.4.3	Study of the GlyR $\alpha 3$ diffusion using single particle tracking	44
2.5	Discussion	48
2.5.1	The GlyR $\alpha 3$ isoforms differ in aggregation state	48
2.5.2	GlyR $\alpha 3$ diffusion studied by ensemble techniques	49
2.5.3	SPT reveals anomalous diffusion in GlyR $\alpha 3$ diffusion	50
2.5.4	An integrated view of receptor diffusion	51
2.5.5	Perspectives for the GlyR $\alpha 3$	52
2.6	Supplementary material: Expression and functionality check of glycine receptors	54
2.6.1	Western blot	54
2.6.2	Electrophysiology	54
2.6.3	Functional GlyR $\alpha 3$ expression in HEK 293 cells	55

3 Analysis of $\alpha 3$ GlyR single particle tracking in the cell membrane

57

3.1	Abstract	58
3.2	Introduction	59
3.3	Materials and methods	61
3.3.1	Single particle tracking	61
3.3.2	Ensemble displacement analysis	61
3.3.3	Local displacement analysis	62
3.3.4	Confined motion	62
3.3.5	Directed motion	63
3.3.6	Statistics	64
3.4	Results	65
3.4.1	Multi-component ensemble analysis	65
3.4.2	Local displacement analysis	67
3.5	Discussion	74

3.5.1	Ensemble displacement analysis	74
3.5.2	Local displacement analysis	75
3.6	Supplementary material	79
3.6.1	Multi-component fit of the cumulative square displacement distribution for $\alpha 3K$ GlyRs	79
3.6.2	Determination of thresholds for anomalous diffusion analysis	80
3.6.3	Ensemble displacement analysis for the $\alpha 3L$ GlyR	81
3.6.4	Local displacement analysis parameters using D_e derived from GlyR $\alpha 3L$ ensemble analysis.	83

4 Membrane distribution of the glycine receptor $\alpha 3$ studied by optical super-resolution microscopy **85**

4.1	Abstract	86
4.2	Introduction	87
4.3	Material & methods	90
4.3.1	Cell culture	90
4.3.2	Transfection	90
4.3.3	Labeling	90
4.3.4	Direct stochastic optical reconstruction microscopy	91
4.3.5	Pair correlation analysis	92
4.4	Results	95
4.4.1	GlyR $\alpha 3$ RNA splice variants display differential organization in the membrane	95
4.4.2	Analysis of GlyR $\alpha 3$ membrane distribution using pair correlation analysis	96
4.4.3	GlyR $\alpha 3$ splice variant clustering properties	98
4.4.4	Colocalization of the GlyR $\alpha 3$ splice variants	99
4.5	Discussion	101

5 General discussion **105**

5.1	Discussion	106
5.2	Future perspectives	114
5.3	Conclusion	119

Reference list **121**

List of abbreviations

GPI	= glycosylphosphatidylinositol
GlyR	= glycine receptor
nAChR	= nicotinic acetyl choline receptor
LGIC	= ligand-gated ion channel
GABA	= γ -aminobutyric acid
5-HT ₃	= hydroxytryptamine
TM	= transmembrane domain
CNS	= central nervous system
TLE	= temporal lobe epilepsy
PSF	= point spread function
NA	= numerical aperture
EM-CCD	= electron multiplying charge coupled device
TIRFM	= total internal reflection fluorescence microscopy
SPT	= single particle tracking
MSD	= mean square displacement
fpALM	= fluorescence photo-activation localization microscopy
dSTORM	= direct stochastic optical reconstruction microscopy
ICS	= image correlation spectroscopy
RICS	= raster image correlation spectroscopy
TICS	= temporal image correlation spectroscopy
FRAP	= fluorescence recovery after photobleaching
CLSM	= confocal laser scanning microscope
HEK	= human embryonic kidney
HA	= haemagglutinin
HBS	= HEPES buffered saline solution
DC	= dichroic mirror
PMT	= photomultiplier tube
PFA	= paraformaldehyde
PBS	= phosphate buffered saline
NF	= not feasible
AA	= amino acid
srPSF	= super-resolution point spread function
AMPA	= α -Amino-3-hydroxy-5-methyl-4-isoxazolepropionic acid

List of figures

Figure 1.1:	Historical models of membrane architecture.	5
Figure 1.2:	Membrane model depicting lateral transport modes for transmembrane proteins.	8
Figure 1.3:	Membrane trafficking and postsynaptic anchoring of the glycine receptor.	13
Figure 1.4:	Multiple sequence alignment of selected GlyR subunits.	15
Figure 1.5:	Fluorescence microscope and Airy disk.	18
Figure 1.6:	Fitting single molecule pixel data with a Gaussian signature.	20
Figure 1.7:	Reversible photoswitching mechanism of conventional synthetic fluorophores	24
Figure 2.1:	Schematic representation of the glycine receptor structure.	33
Figure 2.2:	Image correlation spectroscopy of the GlyR $\alpha 3$.	40
Figure 2.3:	Super-resolution clustering analysis of the GlyR $\alpha 3$.	41
Figure 2.4:	Fluorescence recovery after photobleaching of the GlyR $\alpha 3$.	42
Figure 2.5:	RICS of live HEK 293 cells expressing GlyR $\alpha 3K$ (a) and $\alpha 3L$ (b) allows for a coarse mapping of the mobility of the respective receptors.	43
Figure 2.6:	Temporal image correlation spectroscopy of the GlyR $\alpha 3$.	44
Figure 2.7:	Single particle tracking ensemble analysis of the GlyR $\alpha 3$.	45
Figure 2.8:	Single particle trajectory analysis of the GlyR $\alpha 3$.	46
Figure 2.9:	Expression of the GlyR $\alpha 3$ isoforms in HEK 293 cells.	55
Figure 2.10:	Electrophysiology of the GlyR $\alpha 3$ isoforms.	56
Figure 3.1:	Ensemble displacement analysis of GlyR $\alpha 3K$ diffusion in HEK 293.	66
Figure 3.2:	Identification of anomalous diffusion sections in GlyR trajectories using local displacement analysis.	67
Figure 3.3:	Visualization of local displacement trajectory analysis in a representative area of the bottom membrane.	69
Figure 3.4:	Visualization of L_c variation during short time intervals.	70
Figure 3.5:	Quantitative parameters of the anomalous diffusion events.	72
Figure 3.6:	Two examples of trajectories displaying coincident confined and directed motion.	73
Figure 3.7:	Fitting of the cumulative distribution of square displacements.	79

- Figure 3.8: Determination of thresholds for confined and directed motion levels, respectively L_c and L_d . 80
- Figure 3.9: Ensemble displacement analysis of GlyR $\alpha 3L$ diffusion in HEK 293. 82
- Figure 4.1: Micrographs showing the differential distribution of the HA-GlyR $\alpha 3K$ (A-C) and HA-GlyR $\alpha 3L$ (D-F) in the bottom membrane of HEK 293 cells (colormap hot). 96
- Figure 4.2: Pair correlation analysis of the GlyR $\alpha 3K$ (A,C) and GlyR $\alpha 3L$ (B,D) distribution in the bottom membrane. 97
- Figure 4.3: The clustering parameters derived from the autocorrelation fitting (Eq. 4.2) quantify the differential sub-diffraction organization of the GlyR $\alpha 3L$ (blue) and $\alpha 3K$ (red). 99
- Figure 4.4: Co-expression of the GlyR $\alpha 3$ splice variants in HEK 293 cells, micrographs (A-C) and pair cross-correlation analysis (D,E). 100
-

List of Tables

Table 2.1:	ICS analysis performed on fixed cells expressing either GlyR α 3K or GlyR α 3L.	39
Table 2.2:	The average diffusion coefficient (in $\mu\text{m}^2/\text{s}$) as obtained per ensemble microfluorimetric technique.	43
Table 2.3:	Single particle tracking ensemble average parameters for the GlyR α 3.	47
Table 3.1:	Summary of parameter averages from local displacement analysis of α 3 GlyR trajectories from each expression system.	70
Table 3.2:	Summary of parameter averages from local displacement analysis of α 3L GlyR trajectories using different measures for free diffusion.	83
Table 4.1:	Summary of parameters extracted from fitting the autocorrelation according to equation 4.2.	98

1 Introduction

1.1 The cellular plasma membrane

The formation of biological membranes was an essential step in the creation of life [1]. The cell or plasma membrane forms an internal environment which compacts genetic materials and sustains metabolic activity without loss to the surroundings [2]. Since its existence, the plasma membrane has also played a crucial role in generating bio-energy by supporting ionic currents [3]. In eukaryotic cells, membrane-enclosed organelles have also emerged, e.g. endoplasmatic reticulum, Golgi apparatus, mitochondria, etc. with their individual membranes maintaining characteristic differences between the contents of the organel and the cytosol.

1.1.1 Architecture of the cellular plasma membrane

Despite their differing functions, all biological membranes have a common structure: each is a very thin film of lipid and protein molecules, held together mainly by noncovalent interactions [4]. The lipid nature of the cell membrane was discovered at the end of the 19th century. The discovery was based on similar behavior of cells and oil when introduced to water and the permeability of the cell membrane to fat-soluble anesthetics [5-7]. The lipid molecules are arranged in a bilayer with a thickness of approximately 5 nm, primarily composed of phospholipids and cholesterol [8]. Mammalian cells possess many phospholipid species, with phosphatidylcholine, phosphatidylethanolamine, phosphatidylserine and sphingomyelin as the main constituents. Phosphatidylinositol, a minor constituent, performs important signaling functions [9]. The bilayer arrangement of lipids was established by investigating the membrane surface of red blood cells and visually confirmed using electron microscopy [10-12]. The amphipathic nature of the lipid molecules, with a hydrophilic polar headgroup and two hydrophobic fatty acid tails, was formulated as the principle underlying this arrangement [13]. Furthermore, the lipid bilayer was perceived as a fluid mosaic containing freely diffusing membrane proteins [14].

As the lipid bilayer forms a permeability barrier, the embedded membrane proteins are responsible for the transport of matter and information across the cell membrane [15]. Research on red blood cells was again instrumental in the early study of membrane protein organization (**Figure 1.1a**) [16]. Membrane proteins were initially categorized as peripheral or integral membrane proteins,

based on their binding affinity to the lipid bilayer [17]. In a more modern view, peripheral proteins are associated with the cell membrane but do not extend into the hydrophobic core of the bilayer [18]. They can however be strongly attached to the bilayer through covalent anchoring to lipids [19]. Integral membrane proteins on the other hand possess an inherent amphipathic nature, which allows them to directly protrude into the hydrophobic core of the lipid bilayer [20,21]. The membrane segments are made up of alpha helices or beta barrels and single- or multipass formations are possible [22,23]. Hereby, bi- or polytopic transmembrane proteins are formed containing both intra- and extracellular segments. Membrane proteins often form multimeric complexes, assembling in a specific quaternary structure [24].

A last important element of the cell membrane is the sugar coating or carbohydrate rich surface layer, also referred to as glycocalyx [25]. Both membrane lipids and proteins can be modified, or glycosylated, to contain covalently linked oligosaccharides on their noncytosolic side. Lipids exhibiting this modification are called glycolipids and appear only in the outer leaflet of the bilayer [26]. They can also covalently anchor proteins, as previously mentioned [19]. In case the oligosaccharide modification contains sialic acid, the glycolipids are called gangliosides [27]. Membrane proteins extending into the extracellular space are generally glycosylated [28]. This leads to the formation of glycoproteins or, in case the protein is heavily glycosylated with glycosaminoglycans, formation of proteoglycans [29,30]. From the carbohydrate layer, the transition to the extracellular matrix starts through attached oligosaccharide coated proteins not embedded in the plasma membrane (**Figure 1.1b**).

1.1.2 Plasma membrane heterogeneity

The van der Waals attractive forces between the neighboring fatty acid chains ensure the formation of the bilayer, but generally allow for random mixing of the components. The plasma membrane however, displays a strong heterogeneity in composition. First of all, the different phospholipid species are not distributed equally over the inner and outer leaflet of the bilayer [31]. Phospholipid translocator enzymes ensure phospholipids containing an amino group are in the inner leaflet, while phospholipids containing a choline group are in the outer leaflet [32]. Second, the lipid bilayer can be locally unmixed. This was originally

perceived by the presence of liquid ordered domains, showing reduced fluidity by rigid lipid packing, in the liquid disordered plasma membrane [33,34]. The concept of lipid domains was formulated and cholesterol suggested as an important mediator [35,36].

Later on, the term lipid raft was used to describe phase separated sphingolipid (sphingomyelin, glycosphingolipids and gangliosides) and cholesterol enriched domains [37]. The long, largely saturated acyl chain tails of sphingolipids and the rigidity conveyed by cholesterol, which allow tight acyl chain packing, are suggested as the underlying mechanics of raft formation [38]. The concept of lipid rafts was highly controversial due to methodological disputes concerning lipid raft detection *e.g.* detergent resistance, cholesterol depletion and visualization [39]. A pivotal point was reached, when the previously widely varying properties of rafts were condensed to create a singular definition. This definition states the following: "Membrane rafts are small (10-200 nm), heterogeneous, highly dynamic, sterol- and sphingolipid enriched domains that compartmentalize cellular processes. Small rafts can sometimes be stabilized to form larger platforms, through protein-protein or protein-lipid interactions." [40]. At this point, the involvement of protein components in the genesis and organization of lipid heterogeneities had been formulated and therefore the term membrane raft was preferred [41].

The association of proteins with lipid rafts was first established for glycosylphosphatidylinositol(GPI)-anchored proteins, due to their partitioning in detergent resistant membranes [42]. The attachment of a GPI lipid anchor to a protein is considered a lipid modification targeting proteins to rafts. Fatty acylations, such as myristoylation and palmitoylation, are other lipid modifications shown to do the same [43,44]. Proteins with long hydrophobic transmembrane domains may also favor lipid rafts, due to the increased bilayer thickness of cholesterol enriched domains [45,46]. Another possibility is the presence of specific amino acid motifs, targeting proteins to rafts via lipid-protein or protein-protein interactions [47]. The many possibilities for protein association with lipid rafts have been deemed an important source of raft heterogeneity [37]. A special class of raft, named caveolae, is created by rafts containing the cholesterol-binding protein caveolin [48]. Morphologically caveolae show membrane invagination and functionally they contribute to

signaling, exo- and endocytosis [49]. Thereby, caveolin and other proteins have conveyed important functionality for rafts in biological membranes [50,51]. This has led to extensive research into time and spatial scales of the dynamic interplay between lipids and proteins in membrane domains [52,53].

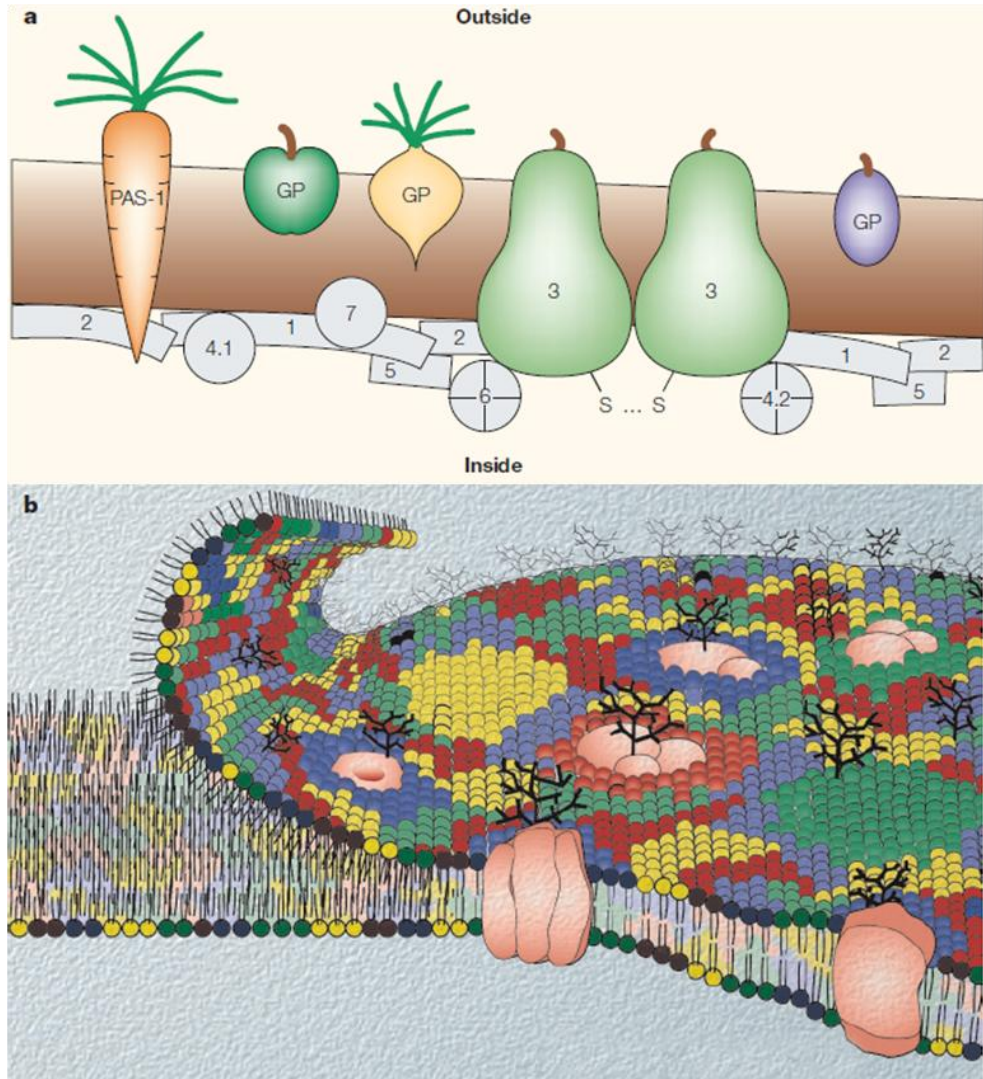


Figure 1.1: Historical models of membrane architecture.

(a) Early view of the red blood cell membrane architecture as postulated by Steck 1974 [16]. (b) An exuberant version of the fluid mosaic model, with extra focus on lipids and lipid rafts (created by P. Kinnunen, Kibron Inc.). Reprinted by permission from Macmillan Publishers Ltd: *Nature reviews molecular cell biology* [54], copyright 2003.

1.1.3 Brownian motion and diffusion

As formulated in the fluid-mosaic model, lipids and proteins diffuse freely in the 2D plane of the membrane [14]. Translational diffusion occurs by the principle of Brownian motion, describing the random motion of particles in liquid or gas. This principle is driven by thermal agitation, which makes particles move and collide, and is applicable to all biological systems [55]. The rate of Brownian diffusion, termed the diffusion coefficient (D), of a spherical particle in a viscous medium is dictated by the Stokes-Einstein equation [56]:

$$D = \frac{k_B T}{6\pi\eta P_h} \quad (1.1)$$

In this equation, k_B represents the Boltzmann constant, T the absolute temperature, η the viscosity of the medium and P_h the radius of the particle. In the numerator the energy of a particle at a given temperature is described, revealing that elevated temperature increases particle energy and its corresponding diffusion coefficient. The denominator is the drag coefficient for a spherical particle, derived from Stokes-law. This coefficient describes the collisional behavior of the particle, showing that increased viscosity or particle size elevates drag, or the number of collisions, and reduces the diffusion coefficient. A last consideration is for the dual nature of temperature, as elevated temperature also decreases viscosity.

The validity of the Stokes-Einstein equation for Brownian motion was experimentally determined by Perrin, who mapped the displacement of colloidal particles over time [57,58]. The average 2D displacement is proportional to the diffusion coefficient according to:

$$\langle r^2 \rangle = 4Dt \quad (1.2)$$

This equation can be derived from Fick's law and allows determination of the diffusion coefficient based on the mean square displacement ($\langle r^2 \rangle$) measured over time (t). Important to realize, is that the random nature of Brownian motion dictates that diffusion is isotropic. This means there is no net displacement for a population of particles at equilibrium.

1.1.4 Diffusion in the plasma membrane

The first evidence for diffusion of membrane components by Brownian motion was derived from rapid intermixing of surface antigens in heterokaryon membranes [59,60]. For translational lateral diffusion of membrane proteins, the original model equation derived from Stokes-Einstein is given by [61]:

$$D = \frac{k_b T}{4\pi\eta_m h} \left(\ln \left(\frac{\eta_m h}{\eta_w P_h} \right) - 0.5772 \right) \quad (1.3)$$

This derivation was based on the model of a cylindrical particle embedded in a lipid bilayer membrane, bounded by aqueous phases on both side. The parameters η_m and η_w represent respectively the viscosity of the membrane and the surrounding fluid, with $\eta_w \ll \eta_m$. The radius P_h is taken to be the radius of the transmembrane cylinder and h represents the thickness of the membrane. Extensions of this formula to encompass larger, micrometer instead of nanometer, membrane structures have been formulated [62]. It has also been suggested that, instead of a weak logarithmic dependence, the diffusion coefficient shows a stronger inverse relation to the radius ($D \propto 1/P_h$) [63]. Effectively using these formulas requires non trivial determination of the viscosities and spatial dimensions of the membrane components. This is further confounded by the membrane heterogeneity described earlier, obstructing free diffusion [64].

However, even before the concept of raft domains was conceived, the structural proteins of the cytoskeleton were already suggested to impede free diffusion in the membrane (**Figure 1.2**) [65,66]. The cytoskeleton is a filamentous network closely apposed to the cytoplasmic face of the plasma membrane [67,68]. Both confined and directed membrane protein motion has been attributed to interactions with the cytoskeleton [69]. The first confinement model was called the "membrane-skeletal fence" and was based on the observation that spectrin and F-actin were capable of corralling membrane proteins [70,71]. A second model described the cytoskeleton membrane anchoring proteins as pickets, transiently confining lipids due to local distortion of the membrane composition [72]. These two models were joined, forming the "picket-fence" model of membrane compartmentalization. From this model the concept of hop-diffusion ensued, based on the hopping of membrane components between the

compartments [73,74]. The findings of directed motion have been coupled to active transport of membrane proteins along cytoskeletal fibers. Slow ($\mu\text{m}/\text{min}$) transport of membrane proteins was shown to occur along actin fibers in motile cells and neuronal growth cones [75,76]. Directed motion of membrane components along microtubules occurs via intracellular vesicles, in relation to long range trafficking [77]. This means the drag of the membrane is no longer relevant and transport is mediated via motor proteins walking on the microtubules [78]. This method of transport resembles saltatory motion and occurs at high speeds ($\mu\text{m}/\text{s}$) [79,80].

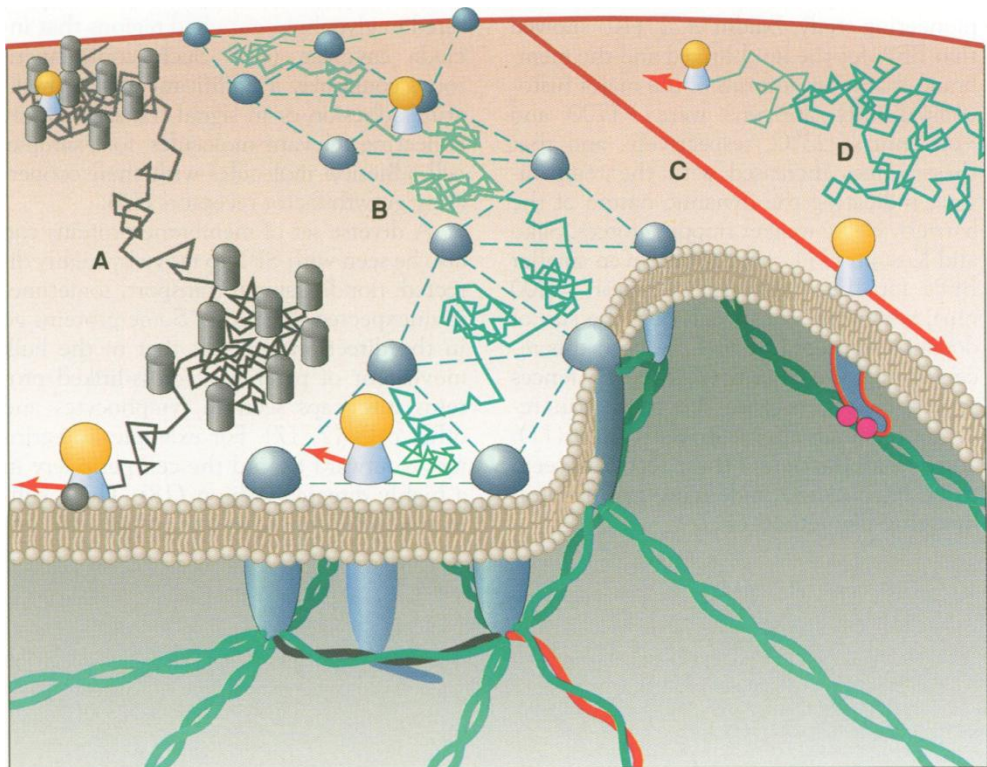


Figure 1.2: Membrane model depicting lateral transport modes for transmembrane proteins.

(A) Transient confinement by obstacle clusters reminiscent of membrane rafts. (B) Confinement by the cytoskeleton according to the picket-fence model. (C) Active directed transport of anchored membrane proteins along the submembranous actin cortex. (D) Free random diffusion of membrane proteins, perhaps the least likely form of diffusion. From K. Jacobson, E.D. Sheets, R. Simson, *Revisiting the fluid mosaic model of membranes*, *Science*, 268 (1995) 1441-1442 [81]. Reprinted with permission from AAAS.

The association of membrane lipids and proteins with rafts was originally not studied from a dynamic viewpoint [42,51]. However, decreased lateral mobility of some lipids in ordered domains of model membranes was observed [82,83]. Hereby, the hypothesis that membrane rafts can influence lateral diffusion of lipids and proteins in biological cells was formulated and some evidence was found in support [84,85]. Nevertheless, a unified model was never developed and the topic of lipid rafts remained controversial [86,87]. Evidence was found for the existence of a lipid shell, selectively targeting membrane proteins to raft domains [88]. This shell constitutes an annulus of motionally restricted lipids arising from differential protein-lipid affinities [89]. In a next step the mobility and dynamic assembly of rafts was shown and the model of raft coalescence triggered by lipid- and/or protein-mediated activation was formulated [90-92]. Cortical actin has also been suggested as a modulator of raft coalescence, thereby bridging raft and cytoskeleton models for membrane compartmentalization [93,94]. Another ordering mechanism, illustrated both via raft association and cytoskeleton anchoring, is oligomerization-induced trapping. Individual proteins diffuse freely, but upon cross-linking or stimulation oligomers are formed, which partition in lipid rafts or display confined diffusion due to anchoring [95,96]. All the aforementioned mechanisms of membrane order strongly increase the complexity of interpreting the spatial organization and diffusion of membrane components.

1.2 The glycine receptor, a ligand-gated ion channel

The glycine receptor (GlyR) is a transmembrane protein complex most famous for mediating fast inhibitory neurotransmission at the synapses in spinal cord, brain stem and other regions of the brain [97]. It was first identified by strychnine binding to synaptic membrane fractions of rat spinal cord [98-100]. This was founded on the recognition of glycine as inhibitory neurotransmitter in the spinal cord and the antagonizing effect of the convulsant strychnine [101]. Upon isolation and purification of the GlyR from rat spinal cord, three polypeptides were found, measuring 48 kDa, 58 kDa and 96 kDa [102]. The 48 kDa polypeptide, responsible for strychnine binding, was termed the α polypeptide [103]. The 58 kDa polypeptide, termed the β polypeptide, and the α polypeptide were found to be glycosylated integral membrane components and were considered as the homologous main components of the receptor [104-106]. The 96 kDa polypeptide was considered a peripheral membrane protein on the cytoplasmic face of the GlyR complex [105,107].

Analysis of the 48 kDa GlyR polypeptide revealed strong homology with the nicotinic acetyl choline receptor (nAChR) subunits [108]. On this basis, the (cys-loop) ligand-gated ion channel (LGIC) super family was born. This receptor family comprises the nAChR, GlyR, γ -aminobutyric acid (GABA) receptors and 5-hydroxytryptamine (5-HT₃) serotonin receptors. All subunits of the LGIC family have strong amino acid homology, with a 15 amino acid cys-loop, formed by a disulfide bridge in the N-terminus, as essential feature. Structurally, LGIC subunits are defined by a large external N-terminus and a smaller external C-terminus, four transmembrane domains (TM1-4) and a cytoplasmic loop between TM3 and TM4 [109]. Quaternary structure analysis revealed the GlyR, similar to all LGIC, forms a channel by symmetric pentameric assembly of homologous subunits, with the TM2 segment contributing to the inner wall of the ion channel [110]. The GlyR ion channel displays anion selectivity and chloride is the mediator of glycinergic effects [111,112]. The chloride flux may cause either depolarization or hyperpolarization, dependent on the chloride equilibrium potential and the cell resting potential. The GlyR is known as a hyperpolarizing, inhibitory receptor, but during embryonic development neuronal chloride concentrations lead to a depolarizing effect of glycine [113,114].

1.2.1 The glycine receptor subunits and stoichiometry

The subunit diversity for the GlyR main channel is limited compared to GABA receptors, the other main inhibitory neurotransmitter receptor of the central nervous systems (CNS) [115]. The originally isolated 48 and 58 kDa polypeptides were identified as the alpha (α) and beta (β) subunits respectively, sharing approximately 47% sequence homology [108,116]. Four genes (*GLRA1-4*) coding different types of α subunits (α 1-4) have been found, with the subunits displaying approximately 80% amino acid homology [117,118]. The α 4 subunit was originally identified in mice and has also been retrieved in chick and zebrafish [117,119,120]. In humans, no evidence of the α 4 subunit has been found and the *GLRA4* gene is suggested to be a pseudogene [121]. Further diversity in subunits is generated by alternative splicing of the α subunit RNAs, as demonstrated for the α 1, α 2 and α 3 subunits [122]. All α subunits have been shown to form functional homomeric receptors in both *Xenopus* oocyte and HEK 293 mammalian cell expression systems [117,123,124]. Biochemical evidence for pentameric assembly of homomeric (α 1) GlyRs and the possibility for different α subunits to assemble as α heteromers has been provided [125,126]. The expression of the α subunits in the rat CNS shows a postnatal switch from α 2 to α 1 as the main subunit, although in some brain regions the α 2 subunit persists [127,128].

In contrast to the α subunit, there is only one gene (*GLRB*) coding for β subunit [116]. Recombinant expression of the β subunit alone does not generate glycine-induced currents and does not lead to the formation of homomeric receptors [111,126]. The β subunit forms heteromeric GlyRs with the α subunits and these can be distinguished from homomeric (α) GlyRs by decreased sensitivity to the antagonist picrotoxin and altered single-channel conductance [129-131]. The stoichiometry of heteromeric GlyRs is disputable, as recently evidence has been found for both a $3\alpha:2\beta$ and a $2\alpha:3\beta$ configuration [132,133]. The β subunit is broadly distributed throughout the CNS, but shows increased postnatal expression [127]. An important source of diversity between α and β subunits is the gephyrin binding domain present in the cytoplasmatic loop of the β subunit [134]. Gephyrin is the 98 kDa polypeptide originally also co-purified with the GlyR complex and functions as a GlyR-Tubulin linker protein [135,136].

1.2.2 Glycine receptor membrane dynamics

Nearly all research concerning GlyR dynamics has aimed at discovering how GlyRs accumulate at postsynaptic sites in neurons (**Figure 1.3**) [137]. This work pertains to $\alpha 1:\beta$ heteromeric receptors, which mediate the bulk of the glycine-evoked inhibitory neurotransmission [138]. These GlyRs are shown to associate intracellularly with gephyrin shortly after synthesis and appearing as a complex in vesicles [134,139]. These vesicles are transported over long distances using gephyrin as a cargo adaptor for kinesin driven anterograde and dynein driven retrograde microtubule transport [140-142]. At sub-membrane sites, actin microfilaments and myosin are suggested to serve as a platform for delivery and internalization of GlyRs [143]. Exocytosis of GlyRs is thought to occur at extrasynaptic sites and endocytosis is shown to be ubiquitination and dynamin-dependent [144-146].

Once inserted in the membrane, GlyRs show lateral diffusion in the membrane and can be reversibly trapped by gephyrin [146,147]. Gephyrin is an essential scaffold protein for clustering of heteromeric GlyRs at postsynaptic sites [148,149]. Diffusion measurements using primary neurons revealed rapid exchange of endogenous GlyRs between synaptic and extrasynaptic compartments, with fast extrasynaptic diffusion and slow confined motion at synaptic sites [150]. The cytoskeleton was also shown to have a profound influence on both synaptic and extrasynaptic GlyR diffusion [151]. Further diffusion measurements reported that GlyR diffusion can also be influenced by gephyrin outside the synapse and suggest multiple association states governing GlyR diffusion in- and outside the synapse [152]. Control of lateral diffusion and transient trapping are now regarded as an important means of regulating the structure and function of the synapse [153].

For homomeric receptors, little is known about their membrane dynamics. It is assumed that they are extrasynaptic, as they cannot bind gephyrin. The $\alpha 2$ GlyRs present during embryonic stages, even before synaptogenesis, are proven to be homomeric [138]. They are however suggested to play a role in the development of glycinergic synapses and may undergo anchoring due to connections with actin-filament bundles [154,155]. Although extrasynaptic GlyRs have also been found in the adult CNS, little electrophysiological evidence

has been found to support homomeric GlyRs on the cell bodies of neurons. The GlyRs on presynaptic terminals however, have been postulated to be homomeric receptors and a homomeric configuration is suggested to convey axonal targeting [156-160].

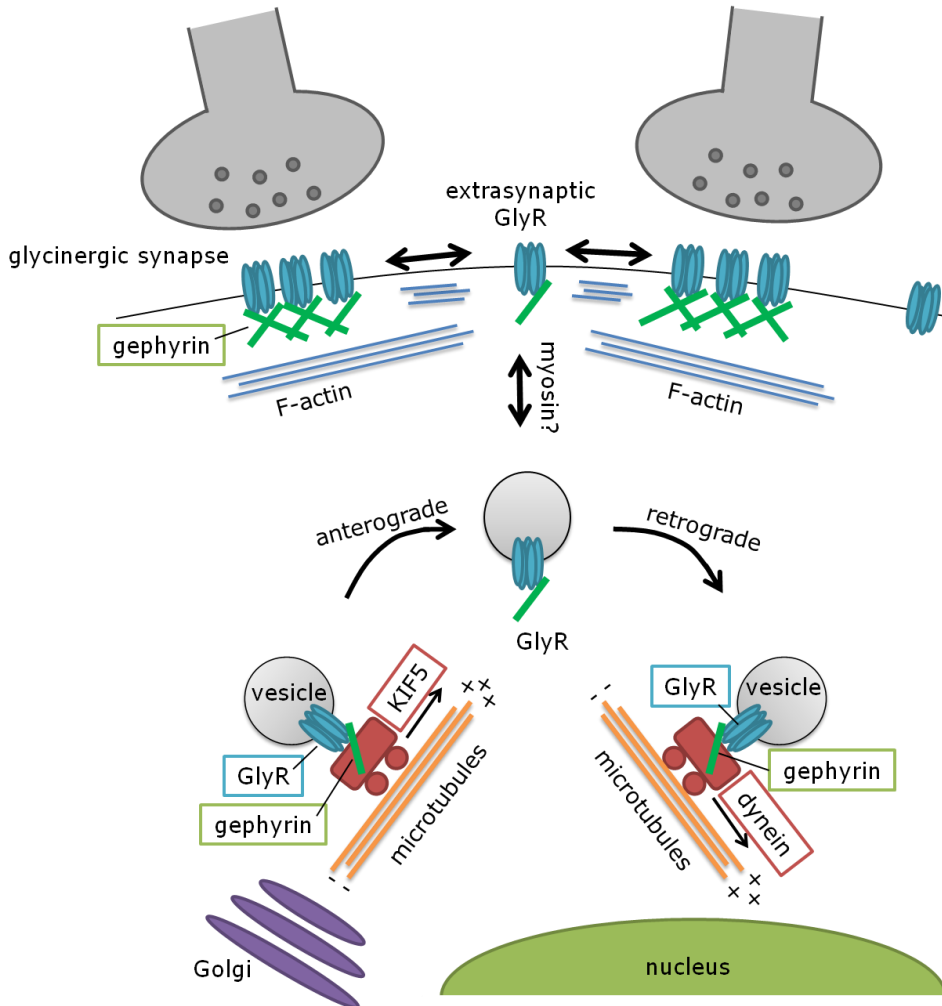


Figure 1.3: Membrane trafficking and postsynaptic anchoring of the glycine receptor.

Newly synthesized glycine receptors (GlyRs) can associate intracellularly with gephyrin and are transported to and from the membrane by motor protein driven microtubular transport. Myosins may play a role in navigating the GlyRs via the sub-membrane actin cortex. Exo- and endocytosis is believed to occur at extrasynaptic sites and the gephyrin scaffold is responsible for GlyR anchoring at postsynaptic sites. Anchoring can either lead to stable fixation of receptors or be a transient event actively controlling the population of receptors at the synapse. Gephyrin association is also believed to influence extrasynaptic receptors, which can also occur dissociated from gephyrin. Based on Dumoulin et al. 2009 [137].

1.2.3 Glycine receptor $\alpha 3$

The GlyR $\alpha 3$ subunit was first identified by homology screening of a rat cDNA library and shown to be a low glycine affinity variant with the same postnatal expression profile as the $\alpha 1$ subunit [161]. The $\alpha 3$ subunit is also referred to as the “sensory” subunit, due to its expression in CNS regions associated with sensory processing. At present, this is manifested by $\alpha 3$ subunit detection in the mouse retina, the rat cochlea and the dorsal horn of the spinal cord; suggesting a role in processing of visual, acoustic and pain stimuli [162-164]. In these processes, signal transduction is, in part, mediated by synaptic $\alpha 3$ subunit-containing GlyRs.

The $\alpha 3$ subunit is also, to a lesser extent, found in the hippocampus, where it is associated with a novel pathophysiological role in temporal lobe epilepsy (TLE) [127,165]. This is related to the RNA editing and splicing properties of the *GLRA3* gene transcript [166,167]. RNA editing has been shown to produce a high agonist affinity GlyR $\alpha 3^{P185L}$ subtype, capable of mediating tonic glycinergic inhibition at ambient glycine concentrations [168,169]. Just as the GlyR $\alpha 3^{P185L}$ subtype is upregulated in TLE, so is GlyR $\alpha 3$ alternate RNA splicing [168,170]. The RNA splicing of the human *GLRA3* gene transcript generates two variants named $\alpha 3K$ and $\alpha 3L$, with the latter containing an additional 15 amino acid sequence “TEAFALKFYRFSDM” in the large cytoplasmatic loop between TM3 and TM4 (**Figure 1.4**) [167]. In some severe cases of TLE an upregulation of the $\alpha 3K$ variant at the expense of the $\alpha 3L$ variant was found [170].

Interestingly, when expressed in HEK 293 cells the $\alpha 3L$ variant shows slow desensitization and membrane clustering, while the $\alpha 3K$ variant shows faster desensitization and diffuse membrane organization [167,170]. When exogenously introduced into $\alpha 3$ subunit deficient primary neurons, the differential membrane organization of the $\alpha 3$ variants persists and leads to alternate synaptic localization, even when co-expressed with the β subunit [170]. An association between clustering and desensitization kinetics has been revealed for $\alpha 1$ GlyRs, yet no causal relationship has been revealed [171].

<i>GlyR</i> α_3L	MAHVRHFRTLVSQGFYFWEAALLLSLVATKETDSAR-----SRSAPMSPSDF	46
<i>GlyR</i> α_3K	MAHVRHFRTLVSQGFYFWEAALLLSLVATKETDSAR-----SRSAPMSPSDF	46
<i>GlyR</i> α_1	---MYSFNTL--RLYLWETIVFFSLAASKEAEEAR-----SAPKPMSPSDF	41
<i>GlyR</i> β	MKFLLTAFLLI-LISLWVEEAYSKEKSSKKGKQYLCPSSQQAEDLARVPANSTSI	59
	: * : : * : : : * : : : : : : : : : : : : : : : : * : : *	
<i>GlyR</i> α_3L	LDKLMGRSTSGYDARIRPNFKGPPVNVTCNIFINSFGSIAETTM DYRVNIFLRQKWNDPRL	106
<i>GlyR</i> α_3K	LDKLMGRSTSGYDARIRPNFKGPPVNVTCNIFINSFGSIAETTM DYRVNIFLRQKWNDPRL	106
<i>GlyR</i> α_1	LDKLMGRSTSGYDARIRPNFKGPPVNVSCNIFINSFGSIAETTM DYRVNIFLRQKWNDPRL	101
<i>GlyR</i> β	LNRRLL---VSYDPRIIRPNFKGIPVDVVNIFINSFGSIQETTM DYRVNIFLRQKWNDPRL	116
	* : : : * : : * : : * : : * : : * : : * : : * : : * : : * : : * : : *	
<i>GlyR</i> α_3L	AY-SEYPD-DSLDDLPSMLDSIWKPDFFFANEKGANFHEVTTDNKLLRIFKNGNVLYSIR	164
<i>GlyR</i> α_3K	AY-SEYPD-DSLDDLPSMLDSIWKPDFFFANEKGANFHEVTTDNKLLRIFKNGNVLYSIR	164
<i>GlyR</i> α_1	AY-NEYPD-DSLDDLPSMLDSIWKPDFFFANEKGAHFHEITTDNKLIRSRNGNVLYSIR	159
<i>GlyR</i> β	KLPSDFRGSALTVDPMTYKCLWKPDFFFANEKSANFHDVTQENILLFIRFDGDLVLSMR	176
	: : : * : * : * : * : * : * : * : * : * : * : * : * : * : * : * : *	
	Cys-loop	P185L
<i>GlyR</i> α_3L	LTLTLLSCPMDLKNFPMDVQTCIMQLESFGYTMNDLIFEWQDEAPVQVAEGLTL	224
<i>GlyR</i> α_3K	LTLTLLSCPMDLKNFPMDVQTCIMQLESFGYTMNDLIFEWQDEAPVQVAEGLTL	224
<i>GlyR</i> α_1	ITLTLACPMDLKNFPMDVQTCIMQLESFGYTMNDLIFEWQEQGAVQVADGLTL	219
<i>GlyR</i> β	LSITLLSCPLDLTLFPMDTQRCMKQLESFGYTTDDLRFIWQSGDPVQL-EKIAL	235
	: : : * : * : * : * : * : * : * : * : * : * : * : * : * : * : * : *	
	TM1	
<i>GlyR</i> α_3L	EK-DLRYCTKHYN-TGKFTCEIVRFHLERQMGYYLIQMYIPSLLVILSWVSWFINMDAA	282
<i>GlyR</i> α_3K	EK-DLRYCTKHYN-TGKFTCEIVRFHLERQMGYYLIQMYIPSLLVILSWVSWFINMDAA	282
<i>GlyR</i> α_1	EK-DLRYCTKHYN-TGKFTCEIARFHLERQMGYYLIQMYIPSLLVILSWISWFINMDAA	277
<i>GlyR</i> β	EDIEYGNCTKYKGTGYTTCVEVIFTLRRQVGFYMMGVYAPTLLIVVLSWLSWFINPDAS	295
	* : * : * : * : * : * : * : * : * : * : * : * : * : * : * : *	
	TM2	TM3
<i>GlyR</i> α_3L	PARVALGITVTLTMTTQSSGSRASLPKVSYVKAIDIWMAVCLLFVFSALLEYAAVNFVSR	342
<i>GlyR</i> α_3K	PARVALGITVTLTMTTQSSGSRASLPKVSYVKAIDIWMAVCLLFVFSALLEYAAVNFVSR	342
<i>GlyR</i> α_1	PARVGLGITVTLTMTTQSSGSRASLPKVSYVKAIDIWMAVCLLFVFSALLEYAAVNFVSR	337
<i>GlyR</i> β	AARVPLGIFSVLSLASECTTLAAELPKVSYVKALD VWLIACLFLGFASLVYAVVQVMLN	355
	. * * * * * : * : * : * : * : * : * : * : * : * : * : * : * : * : * : *	
<i>GlyR</i> α_3L	QHKELLRFR-----RKRKNK-----TEAFALEKRYRFSMDDEVE	376
<i>GlyR</i> α_3K	QHKELLRFR-----RKRKNK-----TEAFALEKRYRFSMDDEVE	361
<i>GlyR</i> α_1	QHKELLRFR-----RKRHH-----KSPM-LNLF-----QEDEA	365
<i>GlyR</i> β	NPKRVEAEKARIAKAEQADGKGNVAKKNTVNGTGPVHISTLQVGETRCKKVCTSKSDL	415
	: * : : : : : : : : : * : : : : : : : : : : : : : : : : * : : *	
<i>GlyR</i> α_3L	RESRFSF-----TAYGMGP-CLQAKDGMTPKGPN-----HPVQVMPKSPDEMRKV	420
<i>GlyR</i> α_3K	RESRFSF-----TAYGMGP-CLQAKDGMTPKGPN-----HPVQVMPKSPDEMRKV	405
<i>GlyR</i> α_1	GEGRFNF-----SAYGMGPAQLQAKDGISVKGANNSTNTNPPAPSKSPEEMRKL	415
<i>GlyR</i> β	RSNDFSI VGS LPRDFELS NYDCYKPIEVNNGLGKSQAKNN-----KPPPAKPV	465
	. . * : : : : * : : : : * : : : : * : : : : * : : : : * : : : *	
	TM4	
<i>GlyR</i> α_3L	FIDRAKKIDTISRACFPFLAFILFNIFYWVIYKILRHEDIHQQQD	464
<i>GlyR</i> α_3K	FIDRAKKIDTISRACFPFLAFILFNIFYWVIYKILRHEDIHQQQD	449
<i>GlyR</i> α_1	FIQRAKKIDKISRIGFPMFLIFNMFYWIIYKIVRREDVHNQ--	457
<i>GlyR</i> β	IPTAAKRIDLYARALFPFCFLFFFNVIYWSIYL-----	497

Figure 1.4: Multiple sequence alignment of selected GlyR subunits.

The primary protein structures of four human GlyR subunits are compared, comprising GlyR α_3L (NP_006520), GlyR α_3K (NP_001036008), GlyR α_1 (NP_001139512), and GlyR β (NP_000815). These sequences were aligned using ClustalW. Stars (*) indicate identical amino acids, colons (:) indicate conserved amino acids and points (.) indicate semi-conserved amino acids. The 15 amino acid difference between the GlyR α_3 splice variants is indicated by the red box. The sequence of the β subunit that holds the interaction site with gephyrin is highlighted in green. Transmembrane domains are marked by blue boxes, while the characteristic cys-loop is marked by a yellow box. Amino acid numbering of the human protein sequence incorporates the signal peptide [167], leading to a 33 amino acid shift compared to the originally reported rat sequence [161]. Therefore the proline involved in P185L RNA editing is located at position 218, marked in pink [169]. Figure courtesy of Nick Smidom.

It is tempting to speculate that the $\alpha 3L$ variant insert produces a direct binding capability for the receptor, as transient stabilization by scaffolds is common for neurotransmitter receptors [137]. However, no anchoring properties have ever been associated with GlyR α subunits. The cytoplasmatic region between TM3 and TM4 is the region of highest sequence diversity between the GlyR α subunits, as well as other members of the LGIC family [122]. In case of the $\alpha 3$ subunit, the loop is known to carry a nuclear localization signal, involved in subunit sorting. A phosphorylation site is also present, involved in regulating the ligand binding site conformation and in mediating prostaglandin disinhibition of pain stimuli [163,172,173]. The insert of the $\alpha 3L$ variant also carries a phosphorylation site, stabilizes the overall spatial structure of the domain and presents a control unit to regulate gating of the ion channel [167,174]. Recently a preferential interaction of exocyst protein Sec8 with the $\alpha 3L$ subunit variant was also demonstrated to equip $\alpha 3L$ GlyRs with axonal and presynaptic trafficking signals [175].

1.3 Single particle optical localization microscopy

The capacity to study single particles with microscopy has led to a revolution across the physical, chemical and biological sciences [176]. The possibility to directly view molecular interactions at an appropriate nanoscopic scale has strongly emphasized the principle of “seeing is believing” in research. In order to achieve the visualization of single particles in optical microscopy, a system is needed that allows imaging of the desired components with good contrast. The principle of fluorescence microscopy is ideally suited to comply with these needs, as explained in the next steps: First, the desired entities must be endogenously fluorescent or specifically labeled with a fluorophore. Subsequently they are placed in the optical system and are excited with narrow wavelength light, suited to the excitation properties of the fluorophore. Due to Stokes’ shift and radiative energy decay, the fluorophores emit fluorescent light of a longer wavelength. Finally, by means of a dichroic mirror, emission filter and a light detector, the fluorescence is captured without interference from the excitation light. This provides an image that brightly displays the desired entity over a dark background [177].

In order for an organic molecule to act as a fluorophore, it must have highly delocalized electrons. This means it will have alternating single and double bonds, typically in the form of aromatic ring structures. The wavelength at which the molecule absorbs light is determined by the size of the conjugated system and is typically within the visible region of the spectrum. Larger conjugated systems are capable of absorbing light of longer wavelengths, even beyond the visible range (> 700 nm) [178]. However, due to unfavorable photochemical properties these dyes lack stability and brightness. Furthermore the capacity to see the emission light by eye is often requisite. The excitation light needs to be of a shorter wavelength and microscopy lenses generally show bad transmission properties for ultraviolet light. Thereby excitation is usually achieved by near-UV or short wavelength visible light, with the lower limit around 350 nm [179]. Next to organic fluorophores semiconductor nanocrystals, named quantum dots, also have the desired properties for fluorescence microscopy. They possess a broad, continuous excitation and narrow size-dependent emission spectrum. Just like organic fluorophores quantum dots can be coupled to other molecules, yet they are more photochemically stable allowing for longer observation times [180].

The term microscopy of course implies an enlarged view is made of a small (microscopic) sample. In a wide-field optical microscope, this is achieved by using lenses which channel the light to the sample and transfer a magnified image of the emission on a detector array. The modulation of light using lenses is governed by a point spread function (PSF), describing how a single point emitter is depicted by the optical system. Due to nature of light as a wave, a point source imaged by a lens-based system with a circular aperture will be depicted as a blurred spot or Airy disk (**Figure 1.5**). This phenomenon imposes a lower limit of discernible detail on an optical system, known as the diffraction limit or resolution (d). The diffraction limit is described by Abbe's formula [181]:

$$d = \lambda/2n \sin \alpha \quad (1.4)$$

This shows the diffraction limit is dependent on the wavelength of the light (λ), the refractive index of the medium (n) and the aperture angle of the lens (α). The composite $n \sin \alpha$ is referred to as the numerical aperture (NA) of the objective. In practice the highest NA obtainable for an objective is around 1.4 and emission light is typically around 550 nm. This results in a theoretical diffraction limit of approximately 200 nm [182,183].

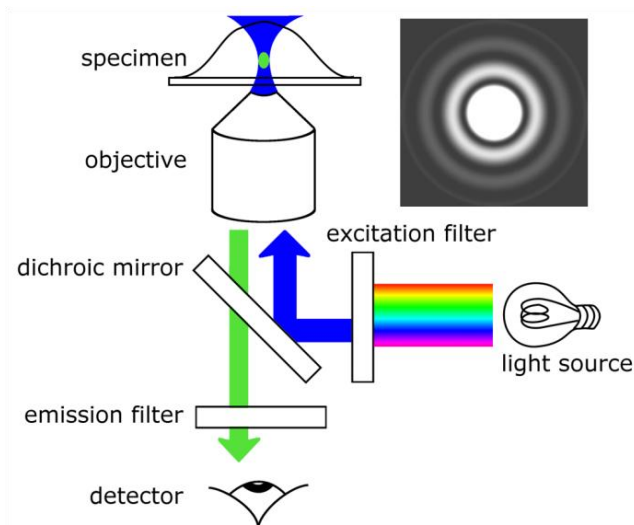


Figure 1.5: Fluorescence microscope and Airy disk.

Optical detection scheme for conventional wide-field fluorescence microscopy is depicted. This set-up is also referred to as an epi-fluorescence microscope, as both excitation and emission light pass through the objective. Courtesy of Nick Smisdom. The inset displays the diffraction pattern associated with a circular aperture; the central part is referred to as the Airy disk.

1.3.1 Localizing and tracking single particles

The capability to observe bio-molecular dynamics using microscopy warranted tools for particle localization. To this end several algorithms were developed, including cross-correlation, determining the center of mass and Gaussian fitting [184-186]. Although the most appropriate method depends on the dynamics and size of the observed particles, Gaussian fitting has emerged as the most commonly implemented strategy for localizing sub-diffraction particles (**Figure 1.6**) [187,188]. These point sources are depicted according to the PSF of the microscope, which can be approached by a two 2D Gaussian profile. In order to apply 2D Gaussian fitting, sub-images are created based on local maxima, which are then used for the fitting procedure. The 2D Gaussian function is of the form:

$$G(x, y) = BG + A \exp \left[-\frac{(x - x_0)^2 + (y - y_0)^2}{2\sigma^2} \right] \quad (1.5)$$

Hereby the position of the molecule corresponds to the central position (x_0, y_0) of the Gaussian peak. The amplitude (A) is determined by the peak intensity and the width (σ) is proportional to the resolution of the optical system (Eq. 1.4). Furthermore the intensity profile of the particle is assumed to be superimposed on a background (BG) of uniform intensity. The accuracy (σ_{xy}) with which each particle can be localized mainly depends on the number of photons (N) collected from the particle and the background photons (b) in the image. In case imaging is performed with a pixelated camera detector, σ_{xy} is described as follows [189]:

$$\sigma_{xy}^2 = F \left\{ \frac{16(\sigma^2 + a^2/12)}{9N} + \frac{8\pi b^2(\sigma^2 + a^2/12)}{a^2 N^2} \right\} \quad (1.6)$$

The factor F is 1 in case no electron multiplication is used for imaging or 2 in case imaging is done with an EM-CCD (electron multiplying charge coupled device) camera. The finite camera pixel size (a) also contributes through pixelation noise. It is apparent that the localization precision improves if more photons can be collected against a low background. Detection schemes such as total internal reflection fluorescence microscopy (TIRFM) or light sheet illumination facilitate this by limiting the excitation volume [190,191]. Emission of individual emitters has to be spatially isolated to ensure reliable fitting of the Gaussian signature to the emission profile. This can be achieved by allowing only a limited subset of labeled particles to fluoresce at a given time.

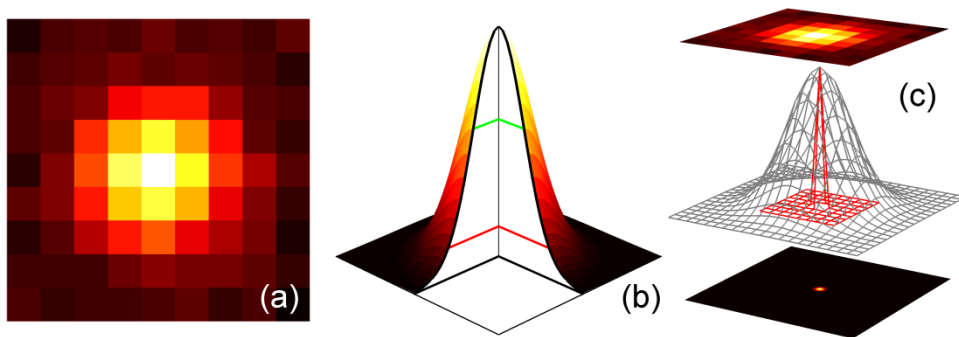


Figure 1.6: Fitting single molecule pixel data with a Gaussian signature.

(a) Single particle emission pattern as detected by the camera. (b) 2D Gaussian profile used to detect the center of the emission pattern. The typical width used to denote the PSF (half width at $1/e^2$, red) and the Gaussian function (σ , green) are shown. (c) Flow chart representing the localization procedure.

Once the particles have been localized, they need to be linked in subsequent frames to establish trajectories. In order to connect the dots, all particles in image i are circumscribed by a circle with radius R_{max} and if exactly one molecule is found within this circle in image $i + 1$, it is connected to the original particle. In case of conflict either the nearest neighbour is selected or the trajectory is terminated. Both solutions are not optimal for trajectory construction and thereby selection of R_{max} and particle density are critical. The former is dependent on the dynamic behavior of the particles and can be determined as a function of the diffusion coefficient (D) and the time between consecutive images (t) via:

$$R_{max} = 2.55\sqrt{4Dt} \quad (1.7)$$

At this value of R_{max} , trajectory construction allows for reliable reproduction of the original diffusion coefficient as empirically determined [192]. Considering the probability distribution of the displacement size, $\sim 86\%$ of all displacements can be found within a radius of R_{max} . This approach works best if the displacement size is significantly smaller than the interparticle distance, thereby putting confines on the particle density depending on the diffusion coefficient. Due to the blinking nature of some single particle tracking (SPT) probes or out-of-focus movements, an off time is often incorporated [193]. Thus a memory is added, which allows the particle to go missing for a limited duration. If the particle returns at the same position within the off time, it will be considered as the same particle and the trajectory will be continued.

1.3.2 Analysis of single particle trajectories

Once the trajectories have been established, the square displacement size can be determined for further quantification. A trajectory can be parameterized by the total number of displacements N , coordinates r_i with $i = 0 \dots N$ and the available time steps $n = 1 \dots N$. The distance traveled during n frames can thus be determined by $(r_{i+n} - r_i)^2$ $i=0 \dots N-n$ of $N - n + 1$ measures. Notice that if $n > 1$, the measures are not independent, which has to be taken into account when determining the error of the mean square displacement (MSD) per time step. The statistical error (var) for MSD determination is given by [194]:

$$var = (4Dnt)^2(2n^2 + 1)/3n(N - n + 1) \quad (1.8)$$

This expression shows that the error in a given trajectory increases for larger time steps and the error for a given time step decreases with longer trajectories. There are two general ways in which the population of square displacements can be further analyzed. Either an ensemble of all square displacements is analyzed per time step or the MSD versus time step relationship is evaluated for each individual trajectory.

In the case of pure Brownian motion, the cumulative probability of the population of square displacements r^2 at time step t , with diffusion coefficient D , is given by a function with a single exponential component [184]:

$$P(r^2, t) = 1 - \exp(-r^2/4Dt) \quad (1.9)$$

In case there are multiple mobile fractions, multiple exponential components can be fitted to determine the different diffusion coefficients. Although each of the mobile fractions can diffuse normally, this can be considered as anomalous given that the total population does not undergo uniform Brownian motion according to a single hydrodynamic radius [195].

If the trajectories are analyzed individually, each provides an estimator of the diffusion coefficient. Given the stochastic nature of diffusion, the accuracy of the estimation is dependent on the length of the trajectory and number of time steps used in the determination (Eq. 1.8). Assuming that short time steps are relatively free of anomalous diffusion, the corresponding MSD can be analyzed according to equation 1.2 to yield an initial diffusion coefficient [196]. If transient anomalous diffusion is present, trajectories can be segmented for local

analysis of displacement size and radius of gyration [197-199]. In case of anomalous diffusion, a non-linear relationship can also be used to describe the MSD with $\langle r^2 \rangle \propto t^\alpha$. This non-phenomenological model indicates sub-diffusion if $\alpha < 1$ and super-diffusion if $\alpha > 1$ [200,201]. If trajectories of sufficient length can be obtained, as by application of quantum dots, more advanced anomalous diffusion functions can be applied to analyze the trajectories [202-204]. Often a constant offset is incorporated into all aforementioned functions, to correct for the finite localization precision [205]. If there is significant movement of the particle during the exposure time of the camera, this can also be corrected during the MSD analysis [206].

1.3.3 Localization based super-resolution imaging

In order to study the dynamics of a bio-molecule, it can be sufficient to image just a few at a given moment and do multiple recordings. However, if we want to study the spatial distribution of a bio-molecule in a fixed state, as many molecules as possible need to be identified in a single image. Spatial organization of nanometer sized bio-molecules, such as membrane proteins, is often obscured by the diffraction limit [182]. Consequently, excitation will make all labeled molecules emit simultaneously, creating overlapping emission profiles and making Gaussian fitting impossible [183]. This problem was solved by different strategies capable of separating emission from individual labels in time using photoswitching [207]. If the photoswitching labels used, are fluorescent proteins, the technique is referred to as (fluorescence) photo-activation localization microscopy ((f)PALM) [208,209]. In case synthetic organic fluorophores are photoswitched, the technique is referred to as (direct) stochastic optical reconstruction microscopy ((d)STORM) [210,211].

Both methods switch the fluorophore between ON and OFF emissive states, allowing only a small stochastic subset of fluorophores to enter the ON state from the stable OFF state [212]. In case the OFF state is a non-emissive dark state, switching to the ON state is referred to as photo-activation. On the other hand, if both states are emissive, yet at spectrally distinguishable wavelengths, switching is termed photo-conversion. In both cases switching can be reversible, allowing a single fluorophore to turn ON and OFF multiple times. For fluorescent proteins, the photoswitching capabilities are inherent to the structure of the

protein [213,214]. Synthetic organic fluorophores however, are also used in conventional ensemble fluorescence microscopy and require a special aqueous environment for OFF state switching [210,215,216].

1.3.4 Photoswitching of conventional synthetic fluorophores

The mechanism of photoswitching for conventional fluorophores is best described for rhodamine and oxazine dyes (most Alexa Fluor dyes), the main classes of the standard fluorophores (**Figure 1.7a**) [217]. It is based on interactions between thiol (RSH) compounds added to the aqueous buffer and fluorophores in the triplet state (3F). The latter state can be achieved by the fluorophore via intersystem crossing from the excited state and can be sustained long enough to allow interactions. The interaction occurs as a reduction of the triplet state by the thiolate anion (RS^-) present at physiological pH, due to a pK_a of 8-9 for most thiol compounds (RSH/RS^-). The thiolate must compete with oxygen (O_2) for interaction with the triplet state, requiring 10-100 mM concentration of thiolate for efficient production of radical anions and thiyl radicals ($^3F+RS^- \rightarrow ^3F\cdot + RS^*$). The fluorophore radical anion is very unreactive and can survive for several seconds even in the presence of molecular oxygen [215]. Some fluorophores can even be further reduced to form the corresponding leuco dye (FH) [217]. Both of the stable OFF states ($^3F\cdot$ and FH) can be oxidized back to the ground state, a process facilitated by irradiation with ~ 400 nm light (**Figure 1.7b**) [215,217]. In case of carbocyanine dyes (Alexa Fluor 647), photoswitching is dramatically improved by adding oxygen scavengers [210]. These dyes are more easily oxidized and removal of oxygen stabilizes the fluorophore radical anion, which absorbs ~ 500 nm and UV light [210,217,218].

Based on the switching mechanism, the photoswitching rate of conventional fluorescent dyes can be manipulated by the excitation intensity, thiol concentration and pH. These parameters must be used to transfer the bulk of the fluorophores to the OFF state and to allow only a limited subset to be stochastically activated to the ON state [219]. This ensures the majority of the fluorophores in the ON state will be spaced further apart than the diffraction limit, making Gaussian fitting possible. The ON state molecules are subsequently transferred back to the OFF state and new stochastic subsets are activated and

imaged. This process must be repeated multiple times, until enough fluorophores are detected to adequately visualize the bio-molecular structure at high resolution [220]. Recordings with multiple color channels are also possible, combining different synthetic fluorophores and/or fluorescent proteins as fluorophores [221-223]. Several distinct methods have also been developed to obtain 3D super-resolution information, thereby not only sharpening the lateral, but also the axial dimension [224-227].

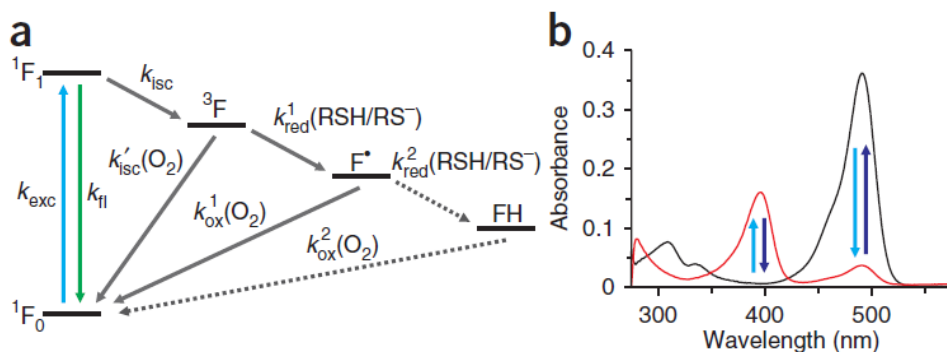


Figure 1.7: Reversible photoswitching mechanism of conventional synthetic fluorophores

(a) Upon irradiation ground state fluorophores (1F_0) are transferred to the excited state (1F_1), where they can either fluoresce or undergo intersystem crossing to the triplet state (3F). The triplet state can react with molecular oxygen or thiolate (RSH/RS^-) and in the instance of the latter transform to a radical anion (F^*). The radical anion can be oxidized or undergo another reduction to create the leuco-dye form (FH). (b) After irradiation with 488 nm light (light blue) in the presence of 100 mM thiolate, absorption of Alexa Fluor 488 at 488 nm (black line) disappears and the radical anion, absorbing at 400 nm appears (red line). The fluorescent state is recovered upon excitation with 400 nm light (dark blue). Reprinted by permission from Macmillan Publishers Ltd: Nature Protocols [217], copyright 2011.

1.3.5 Analysis of super-resolution images

Localization of bio-molecules in super-resolution imaging is identical to SPT. However, instead of creating trajectories, a super-resolution image is made by compiling all localizations in a single plane. The first merit of a super-resolution image is that it can uncover structural details previously obscured by the diffraction limit [228,229]. Hereby, accurate estimations of conformation and size of supra-molecular assemblies can be done [133,230]. However, for some bio-molecules the presence of a higher order assembly is speculative and multiple organizational conformations can be possible [231,232]. Therefore a quantification of intermolecular organization is needed and the pointillistic nature of localization based super-resolution images provides an ideal substrate [233].

A point pattern analysis can be done to compare the measured point distribution to a random distribution. A primary approach, used frequently in super-resolution imaging, is the application of Ripley's K-function designed for statistical inference from spatial processes [234-237]. This function represents the expected number of points N within a distance r of another point, normalized by the number of points per area λ [238]:

$$K(r) = \frac{1}{n} \sum_{i=1}^n N_{p_i} / \lambda \quad (1.10)$$

where p_i is the i th point and the sum is taken over n points [239]. The K-function can be further linearized and normalized to zero, defining the H-function [240]:

$$H(r) = \sqrt{\frac{K(r)}{\pi}} - r \quad (1.11)$$

This function indicates the presence of clustering by positive values and dispersion by negative values, over the available length scale [240,241]. In some instances the cluster size has been determined using this method [231,236]. However, the use of Ripley functions to quantify domain size is found not to be straightforward [239]. Furthermore, modern optical fluorescence super-resolution techniques also generate artifacts capable of influencing conventional spatial point pattern analysis [242,243]. Therefore, a new method was recently developed named pair correlation analysis [244]. This method uses correlation functions to test for fluctuations in spatial organization of point patterns [245]. The major advantage, is that pair correlation analysis incorporates the presence of a super-resolution PSF arising due to overcounting [246]. The results from pair correlation analysis also provide estimates of both the spatial scale and the occupation density of clustering retrieved from point patterns [247,248].

1.4 Research question and hypotheses

The main research question addressed by this work is as follows: Can optical sub-diffraction microscopy be used to study RNA splicing effects on the GlyR $\alpha 3$ membrane properties? Considering that optical sub-diffraction microscopy gives direct access to details obscured by the diffraction limit of conventional microscopy, the hypothesis corresponding to the main research questions can be formulated as follows: RNA splicing alters membrane order of the GlyR $\alpha 3$ on a nanoscopic scale. Two questions remain regarding the translation of this hypothesis to actual research: (1) How do we define membrane properties to infer order? (2) Which optical sub-diffraction technique(s) will we apply?

The first question can be solved by dividing membrane behavior in dynamic lateral diffusion and static distribution. These two elements are related and thus expected to correlate. Lateral diffusion of membrane proteins is prone to anomalous diffusion, occurring when interactions in the membrane environment alter the physical nature of protein diffusion. The distribution of membrane proteins is prone to higher order organization into clusters. By this division, the hypothesis can also be specified in 3 sub-hypotheses: (1) RNA splicing is responsible for differential lateral anomalous diffusion of the GlyR $\alpha 3$. (2) RNA splicing is responsible for differential higher order clustering of the GlyR $\alpha 3$. (3) Anomalous lateral diffusion and higher order clustering of the GlyR $\alpha 3$ are correlated on a nanoscopic scale.

The decision of which techniques to use, was made via an agreement between the groups of Professor Ameloot and Professor Hofkens. In the former group, fluorescently labeled antibodies were used for the conventional microscopy of the GlyR $\alpha 3$. This was due to lack of a suitable fluorescent protein fusion analogue. At the same time, the group of Professor Hofkens acquired the expertise for photoswitching conventional fluorophores used in antibody labeling, also known as direct stochastic optical reconstruction microscopy (dSTORM). The use of a quasi identical label across all techniques was also considered favorable, by limiting label induced variation in the results. Therefore, single particle tracking diffusion measurements were done with conventional fluorophores, instead of more photostable labels, and the super-resolution dSTORM method was chosen as imaging modality to study clustering.

2 Ensemble and single particle fluorimetric techniques in concerted action to study the diffusion and aggregation of the glycine receptor $\alpha 3$ isoforms in the cell plasma membrane

Kristof Notelaers*, Nick Smisdom*, Susana Rocha, Daniel Janssen, Jochen C. Meier, Jean-Michel Rigo, Johan Hofkens, Marcel Ameloot

* authors contributed equally

Journal:

Biochimica et Biophysica Acta (BBA) – Biomembranes 2012

Volume 1818, Issue 12, Pages 3131-3140

doi: 10.1016/j.bbamem.2012.08.010

2.1 Abstract

The spatio-temporal membrane behavior of glycine receptors (GlyR) is known to be of influence on receptor homeostasis and functionality. In this work, an elaborate fluorimetric strategy was applied to study the GlyR $\alpha 3K$ and L isoforms. Previously established differential clustering, desensitization and synaptic localization of these isoforms implies that membrane behavior is crucial in determining GlyR $\alpha 3$ physiology. Therefore diffusion and aggregation of homomeric $\alpha 3$ isoform-containing GlyRs were studied in HEK 293 cells. A unique combination of multiple diffraction-limited ensemble average methods and sub-diffraction single particle techniques was used in order to achieve an integrated view of receptor properties. Static measurements of aggregation were performed with image correlation spectroscopy (ICS) and, single particle based, direct stochastic optical reconstruction microscopy (dSTORM). Receptor diffusion was measured by means of raster image correlation spectroscopy (RICS), temporal image correlation spectroscopy (TICS), fluorescence recovery after photobleaching (FRAP) and single particle tracking (SPT). The results show a significant difference in diffusion coefficient and cluster size between the isoforms. This reveals a positive correlation between desensitization and diffusion and disproves the notion that receptor aggregation is a universal mechanism for accelerated desensitization. The difference in diffusion coefficient between the clustering GlyR $\alpha 3L$ and the non-clustering GlyR $\alpha 3K$ cannot be explained by normal diffusion. SPT measurements indicate that the $\alpha 3L$ receptors undergo transient trapping and directed motion, while the GlyR $\alpha 3K$ displays mild hindered diffusion. These findings are suggestive of differential molecular interaction of the isoforms after incorporation in the membrane.

2.2 Introduction

The diffusion and aggregation of receptors in the cell membrane have received considerable attention in the last decade.[249-252] In addition to endo- and exocytotic cycling of these membrane proteins, their movement and distribution in the plasma membrane can considerably contribute to the homeostasis of these receptors in the membrane.[253-255] In this way, the cell possesses extra tools to fine-tune receptor-mediated signaling events.[50,171,256] An example of this, is surface trapping of neurotransmitter receptors at postsynaptic sites for the facilitation of neurotransmission.[169,257-259] Hence, a study of the spatiotemporal membrane behavior of neurotransmitter receptors is important in fully comprehending the physiological receptor function.

The transmembranous glycine receptor (GlyR) $\alpha 3$ is a neurotransmitter receptor subtype for which membrane properties are implicated in regulating signaling events. Post-transcriptional processing of the *GLRA3* gene transcript [161] gives rise to two isoforms identified as the GlyR $\alpha 3K$ and $\alpha 3L$ [167]. The former is the short isoform exhibiting a diffuse membrane staining and fast desensitization kinetics, while the latter contains a 15 amino acid insert (**Figure 2.1a**), exhibits a clustered membrane appearance and slow desensitization kinetics.[167,170] An altered expression ratio of these isoforms has been measured in patients with a severe form of temporal lobe epilepsy (TLE).[166,168,170] A differential synaptic localization of the isoform subunits, has been associated with this observation.[170] In order to improve the understanding of these isoform-related characteristics, this work investigates the spatiotemporal membrane behavior of homomeric[138] (**Figure 2.1b**) $\alpha 3K$ or $\alpha 3L$ GlyRs on different time and spatial scales.

The GlyR $\alpha 3$ diffusion and aggregation were studied by means of both ensemble average and single particle fluorimetric techniques, either static or dynamic. Earlier work combining fluorescence recovery after photobleaching (FRAP)[260,261] and single particle tracking (SPT)[184,192,204,262,263] measurements for characterization of protein diffusion was inspirational for our fluorimetric approach.[194,200,264] In this way an integrated view of receptor properties is obtained and possible technical bias in the interpretation is reduced. However both the confocal laser scanning microscope (CLSM)[265,266]

and total internal reflection fluorescence microscope (TIRFM)[191,267,268], used respectively for FRAP and SPT, provide several more techniques for receptor characterization, without requiring drastic changes to the set-up. In this work the CLSM was used not only for FRAP, but also for image correlation spectroscopy (ICS)[269,270] and raster image correlation spectroscopy (RICS)[271,272]. The range of techniques applied on the TIRFM was extended beyond SPT, with temporal image correlation spectroscopy (TICS)[273,274] and single particle based localization microscopy[208,209,275-277], in this case direct stochastic optical reconstruction microscopy (dSTORM)[210,215,217].

The aggregation state of both $\alpha 3$ isoforms was investigated by ICS and dSTORM. ICS has the advantage that it can be applied on a commercial CLSM and that it can determine the aggregation state of membrane proteins with very low detection limits. However, ICS is diffraction-limited and does not allow for the direct estimation of the cluster size. This hurdle was overcome by dSTORM, which generates a sub-diffraction image. Since the biological samples of both techniques are identical, except for the addition of a reducing agent to the measuring solution, the extra workload to apply both techniques is minimal once they are operational. The diffusion of the receptors was studied at various length and time scales using, in order of decreasing scale, FRAP ($>1 \mu\text{m}$, seconds to minutes), TICS (diffraction limited, ms to s), RICS (diffraction limited, μs to s) and SPT (sub-diffraction technique, ms to s). In addition to the different scales they cover, two fundamentally different types of results are obtained: FRAP, TICS and RICS return all an ensemble averaged result, while SPT generates individual information for every tracked particle. For all fluorescence based techniques employed, an organic fluorophore coupled to a primary antibody was used for receptor labeling, allowing for the use of similarly sized labels for all techniques. Furthermore all dynamic measurements were carried out at 37°C , in order to mimic the effect of body temperature on receptor movement and membrane viscosity.

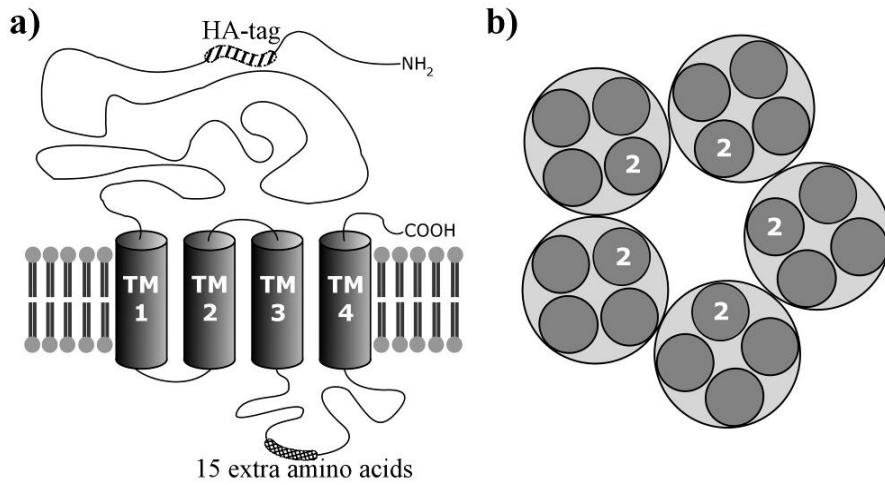


Figure 2.1: Schematic representation of the glycine receptor structure.

a) General structure of a GlyR subunit showing the four transmembrane α helices (TM1 – TM4) and the large, extracellular N-terminal domain. The location of the HA-tag used in this study is indicated, as well as the region of the 15 extra amino acids of the L isoform. b) A functional, homomeric GlyR comprises five subunits, with TM2 of each subunit lining the pore.

2.3 Materials and Methods

2.3.1 Cell culture

Human embryonic kidney 293 cells (HEK 293, kindly provided by Dr. R. Koninckx, Jessa Hospital, Hasselt, Belgium) were maintained at 37°C in a humidified incubator at 5% CO₂ in Dulbecco's modified eagle's medium (Ref. 41966, Gibco BRL, Paisley, UK) supplemented with 10% fetal calf serum (Biochrom AG, Berlin, Germany) and a penicillin (100 IU/ml)-streptomycin (100 µg/ml) mixture (Invitrogen, Merelbeke, Belgium). The cells used for microscopic observation were plated two days before the experiment in 8-well Lab-Tek™ II chambered coverglass (Nalge Nunc International, Rochester, NY, USA) seeded at a density of 20,000 cells per well in transfection medium. This is Dulbecco's modified eagle's medium (Ref. 41965, Gibco BRL, Paisley, UK) supplemented with 10% fetal calf serum but without the penicillin/streptomycin mixture.

2.3.2 Transfection

After overnight incubation, the cells were transfected using calcium phosphate co-precipitation with plasmids encoding for the haemagglutinin (HA)-tagged (**Figure 2.1a**) splice variants α 3K and α 3L of the mouse GlyR α 3.[170] The HA-tag was located in the extracellular N-terminal domain between amino acids 35 and 36.[170] The plasmids were diluted in 250 mM CaCl₂ buffer at a concentration of 20 ng/µl and an equal amount of HEPES buffered saline solution (HBS, pH 7.05) was added dropwise. After incubation of 15 minutes, this mixture was added to the culture medium of the cells. All cell recipients used in the various experiments received a final amount of DNA of 0.21 µg/cm². After 6 hours, the transfection medium was replaced with transfection medium supplemented with 200 nM strychnine. All measurements occurred within 24 to 36 hours after transfection.

2.3.3 Labeling of exogenous GlyRs

A chicken polyclonal anti-HA antibody (Bethyl lab Inc, Montgomery, TX, USA) was used to stain the HA-tagged GlyRs. This antibody was directly labeled with Alexa Fluor 488 (Alexa 488) or Alexa Fluor 647 (Alexa 647) using a commercial Alexa Fluor 488/647 tetrafluorophenyl labeling kit (Molecular Probes/Invitrogen) according to the manufacturer's protocol. Two vials of reactive fluorochrome

were used to increase the degree of labeling. The degree of labeling was determined using a Nanodrop ND-1000 spectrophotometer (Thermo Scientific, Wilmington, DE, USA) at 3.9 (Alexa 488) and 4.4 (Alexa 647) labels per antibody. Cells transfected with the GlyR $\alpha 3$ were rinsed twice with HEPES-buffered DMEM without phenol red (Ref. 21063, Gibco), abbreviated as MWPR (medium without phenol red), and incubated for 10 minutes at 37°C with a 4 $\mu\text{g}/\text{ml}$ (Alexa 488) and 2 $\mu\text{g}/\text{ml}$ (Alexa 647) antibody solution. Afterwards, cells were rinsed three times with MWPR and used for live cell imaging (FRAP, RICS, TICS, SPT) or fixed for 10 minutes using 4% (w/v) paraformaldehyde (PFA) in phosphate buffered saline (ICS, dSTORM).

2.3.4 Image correlation spectroscopy

Bottom membrane images of fixed cells were acquired using a Zeiss LSM 510 META (Carl Zeiss, Jena, Germany) CLSM on an inverted epifluorescence Axiovert 200M motorized frame equipped with an α PLAN-APOCHROMAT 100x/1.46 objective (Carl Zeiss). 150 fs pulsed laser light of a Titanium:Sapphire laser (Mai Tai, Spectra-Physics, Irvine, CA, USA) tuned at an output wavelength of 930 nm (1.4 W output power) with 1.5 mW on the stage was used to excite Alexa 488. The emission light was detected using non-descanned detection: the fluorescence was directed using a dichroic mirror (DC) FT685, a short-pass KP685 and a band-pass BP495-545 towards a photomultiplier tube (PMT; Hamamatsu 7422, Herrsching am Ammersee, Germany). This PMT was connected to an SPC830 card (Becker and Hickl, Berlin, Germany) synchronized by the scan pulses from the CLSM. Data were acquired in FIFO imaging mode. The resulting images have a 512 by 512 resolution, a pixel size of 22 nm, and a pixel dwell time of 51.2 μs . Data were analyzed using in-house developed routines written in a MATLAB® environment (R2010b, The Mathworks, Gouda, The Netherlands) according to a published protocol for ultrasensitive detection.[270]

2.3.5 Direct stochastic optical reconstruction microscopy

Transfected cells were stained with Alexa 488 and fixed prior to incubation with a buffered solution containing 100 mM cysteamine (Sigma-Aldrich). dSTORM was carried out on these cells at room temperature using an inverted epifluorescence microscope (Olympus IX71 frame S1F-3, Olympus Optical, Tokyo,

Japan) equipped with a PlanApo 60x oil objective (NA 1.45; Olympus Optical). The beams of a 100 mW 488 nm (Excelsior 488, Spectra-Physics) and a 100 mW 405 nm (Cube Coherent) diode laser were consecutively selected by mechanical shutters during respectively 50 and 40 ms at a repetition rate of 10 Hz. This light was directed by the DC (z405/491rdc; Chroma, Bellow Falls, VT, USA) towards the objective in off-axis mode to obtain total internal reflection. Excitation light was removed using the DC and a HQ500LP emission filter (Chroma). The 488 nm excitation light was used to excite the Alexa 488 and to obtain a suitable OFF switching rate. The ON switching rate was controlled by the 405 nm laser light with 40 ms exposure time in the overall sequence.[278] The images were recorded at 10 Hz using an EM-CCD camera (ImageEM, Hamamatsu) with 50 ms integration time, a resolution of 512×512 and an image pixel size of 80 nm. The camera was synchronized with the exposure time of the 488 nm laser light, reducing additional background introduced by the 405 nm light exposure. Using home-developed software the particle positions were determined and mapped out on a 20 nm pixel grid corresponding to the localization precision[189,279]. Multi-distance spatial clustering analysis was performed on the obtained point maps using Ripley's H-function[240]. This function is derived from Ripley's K-function[280,281], but represents clustering and dispersions by means of positive and negative values respectively.

2.3.6 Fluorescence recovery after photobleaching

FRAP measurements were performed using a Zeiss LSM 510 META CLSM (Carl Zeiss) on an epifluorescence Axiovert 200M motorized frame. The Alexa 488 was excited with the 488 nm line (selected by a 488 ± 10 nm interference-base laser cleanup filter) of the 30 mW air-cooled argon ion laser (5.5 A tube-current) under the control of an AOTF (set at 0.8% transmission). The excitation light was directed to the sample via a DC (HFT 488) and a Plan-Neofluar 40x/1.3 oil immersion objective (Carl Zeiss). The fluorescence light was detected in descanned mode through the DC and a long-pass LP505 emission filter to the PMT. The pinhole size was set to 3 Airy units and the image size was typically set to 512×512 pixels with a pixel size of 63 nm. The interval between the start of subsequent frames was determined as $1/3 \tau_D$. Each time series typically comprised 2 pre-bleach frames and 18 recovery frames. Cells were kept at 37°C by means of a small stage incubator and an objective heater (Pecon, Erbach,

Germany). Resulting time series were analyzed using custom written routines in a MATLAB environment based on published software components.[261] A new approach was introduced to select a reference region that comprises the bleach region of interest (ROI) and its perimeter in which the fluorescence can be assumed to be constant after bleaching occurred. This approach allows extraction of the recovery curve without user biased selection of a reference region and finds its origin in a procedure suggested by Phair[282,283]. Two FRAP models are used in the analysis step: the uniform disk model[284] and the generalized disk model[261]. The latter model was implemented with the instrumental resolution factor fixed at the estimated value of $0.07 \mu\text{m}^2$.

2.3.7 Raster image correlation spectroscopy

The RICS measurements were performed with the identical setup as used for ICS. A small stage incubator and an objective heater (Pecon) were used to keep the cells at $37 \text{ }^\circ\text{C}$. Besides the α Plan-Apochromat 100x/1.46 objective (Carl Zeiss), also a LD C-Apochromat 40x/1.1 W Korr UV-VIS-IR objective (Carl Zeiss) was used. Pixel sizes were respectively 22.1 nm and 54.8 nm and image resolution was 512×512 . Pixel dwell times (τ_p) of 163.9 μs , 102 μs , 51.8 μs , 25.6 μs and 6.4 μs were used. This range of scan speeds was used to explore possible fast motion of the receptors. The associated line times can be calculated as $1200\tau_p n_{tracks}$, where n_{tracks} is the number of times each line is sequentially scanned before proceeding to the next line. These multiple scanning of each line was applied to increase the line time to further expand the dynamic range of the technique. Image analysis was performed in the MATLAB environment as published elsewhere.[285]

2.3.8 Temporal image correlation spectroscopy

Transfected cells were stained as described and kept at 37°C through the use of a commercial stage incubator (Pecon GmbH, Erbach, Germany). Cargille type 37 (Cargille Labs, Cedar Grove, NJ, USA) was used as immersion oil. All images were acquired using the setup as described for dSTORM, but without the 405 nm laser light. Two neutral density filters (optical density 2.5 and 0.1) were introduced to minimize photobleaching of Alexa 488 as much as possible. To reduce the photobleaching even further, a shutter in the beam path, which also triggered the camera, was used to block the laser light between consecutive

images. The exposure time of the camera was kept constant at 50 ms and the EM gain was set at 149. Images were acquired at various acquisition rates ranging from 50 ms to 5 s. Data analysis was performed using custom written software in the MATLAB environment according to published approaches.[273,286] A correction for photobleaching was applied as described.[273]

2.3.9 Single particle tracking

The SPT measurements were carried out on the set-up that also accommodated the dSTORM and TICS measurements.[287] Alexa 647 was used with excitation from a 60 mW 642 nm diode laser (Excelsior 642, Spectra-Physics), a z647rdc DC and a 665LP emission filter (Chroma). The exposure time of the camera was kept constant at 50 ms and the EM gain was set at 610. Bottom membrane images were acquired at 10 Hz with shuttered exposure to minimize photobleaching. Live cells were kept at 37°C through the use of a commercial stage incubator (Pecon) and Cargille type 37 was used as immersion oil. Particle detection and localization, trajectory construction and calculation of the mean square displacements ($\langle r^2 \rangle$) for each time lag (t_{lag}) were done by in-house developed MATLAB® routines. Only trajectories with a minimum of 16 time steps were considered. The localization precision (σ), determined by tracking of Alexa 647 labeled GlyRs at 37°C in cell membranes fixed for 10 minutes with 4% PFA, was kept fixed. For short time range diffusion, the diffusion coefficient was determined by fitting the first three time lags (D_{1-3}) of trajectories with the linear function $\langle r^2 \rangle = 4Dt_{lag} + 4\sigma^2$. [196] For long time range diffusion, fitting of the first quarter [196] of the displacement data was done using the non-linear function $\langle r^2 \rangle = 4D't_{lag}^\alpha + 4\sigma^2$ [200,201], with D' and α as freely adjustable fitting parameters. The exponent (α) allows for a time-dependent diffusion coefficient (D'), which improved fitting significantly. Tracks were considered immobile if the $\langle r^2 \rangle < 4\sigma^2$ for any time lags in the fit or if $\langle r^2 \rangle_{t_{lag}=1} > \langle r^2 \rangle_{t_{lag}>1}$.

2.4 Results

Each experimental technique was applied to two separate expression systems. Each system comprised the expression of a different $\alpha 3$ (K or L) subunit isoform in HEK 293 cells. For both isoforms individual expression of the subunit lead to the formation of functional transmembrane receptors. This was verified by analyzing protein expression with western blot and measuring glycine-evoked membrane currents using whole-cell patch-clamp (SM **Figure 2.9**, SM **Figure 2.10**).

2.4.1 GlyR $\alpha 3$ aggregation state

The membrane aggregation state of the GlyR $\alpha 3$ isoforms in fixed samples was studied by using ICS and dSTORM. ICS analysis was carried out on regions of the bottom membrane with an apparent homogeneous distribution of fluorescent entities (**Figure 2.2**). The average brightness (counts/s per entity) was determined by combining the measured average density of fluorescent entities together with the associated average fluorescence intensity of the image (**Table 2.1**). [270] Using this analysis, the fluorescent entities of GlyR $\alpha 3L$ are found to be approximately 8 times (7.5 ± 0.4) brighter as compared to their GlyR $\alpha 3K$ counterparts. Assuming that the brightness of the fluorescent labels is independent of the aggregation state of the receptor and that each fluorescent entity of GlyR $\alpha 3K$ corresponds to an individual receptor, it can be concluded that each fluorescent entity of GlyR $\alpha 3L$ corresponds with a cluster comprising eight times more labeled receptors. The size of the GlyR $\alpha 3L$ clusters is below the diffraction limit as the observed radial beam radius ω_0 is essentially constant (**Table 2.1**).

Table 2.1: ICS analysis performed on fixed cells expressing either GlyR $\alpha 3K$ or GlyR $\alpha 3L$.

Particle density and brightness were corrected for background intensity and non-specific binding of the antibody.

Splice variant ^a	Density (entities/ μm^2)	Brightness (counts/s entity)	ω_0 (nm)
GlyR $\alpha 3K$	5.9 ± 0.8^b	0.28 ± 0.04	$43 \times 10 \pm 8 \times 10$
GlyR $\alpha 3L$	1.3 ± 0.3	2.1 ± 0.4	$40 \times 10 \pm 2 \times 10$

^a For each isoform 9 cells were measured

^b Errors are reported as standard error of the mean

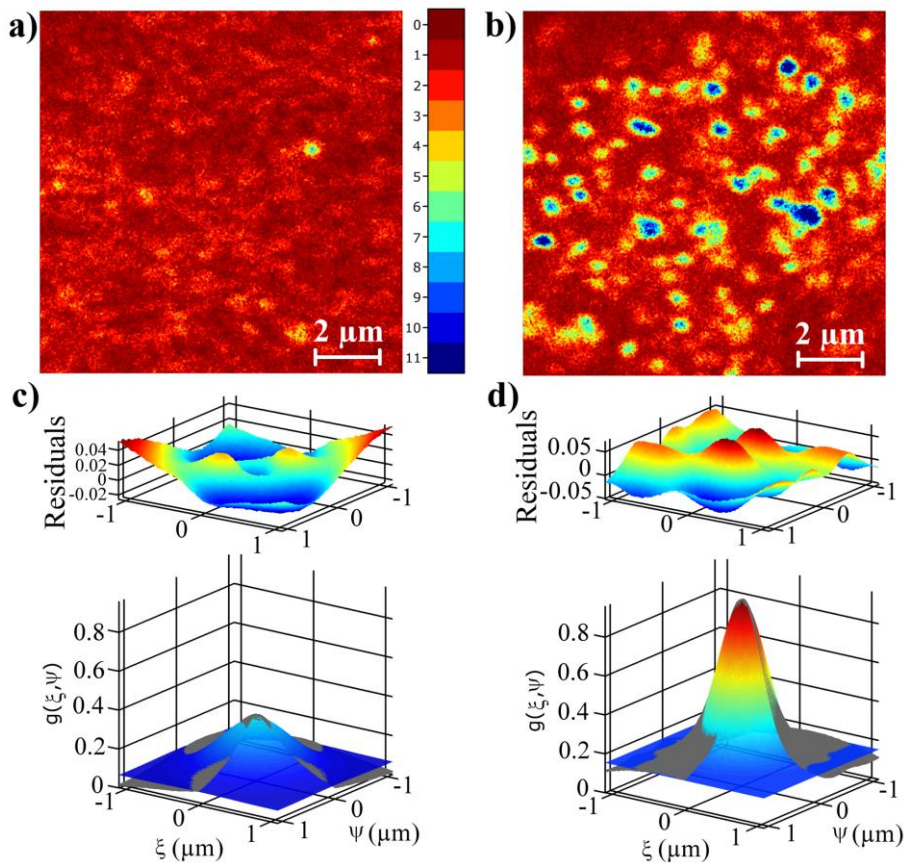


Figure 2.2: Image correlation spectroscopy of the GlyR $\alpha 3$.

Representative images obtained from respectively GlyR $\alpha 3K$ and $\alpha 3L$ in fixed HEK 293 cells are shown by (a) and (b). Both images have the same intensity scale. Qualitative inspection reveals a diffuse staining of the K splice variant and a punctate pattern of GlyR $\alpha 3L$. (c) and (d) are the experimentally obtained spatial autocorrelation function (gray shade, facing quadrant removed) of respectively GlyR $\alpha 3K$ and $\alpha 3L$, together with the best fit (colored surface). The plot of the weighted residuals is indicated above the corresponding spatial autocorrelation function.

dSTORM experiments yield point accumulation images representing a map of GlyR $\alpha 3$ locations in the bottom membrane (**Figure 2.3a, b**). Analysis of these point locations by Ripley's H-function indicates a clear deviation from random distribution for the GlyR $\alpha 3L$, and this in contrast to the GlyR $\alpha 3K$. The GlyR $\alpha 3L$ point distribution yields positive values for the H-function, up to 1 μm and with the maximum of the H-function at 280 nm. For the GlyR $\alpha 3K$ the maximum of the H-function is at a distance of ≈ 20 nm, which is of the same order as the localization precision.

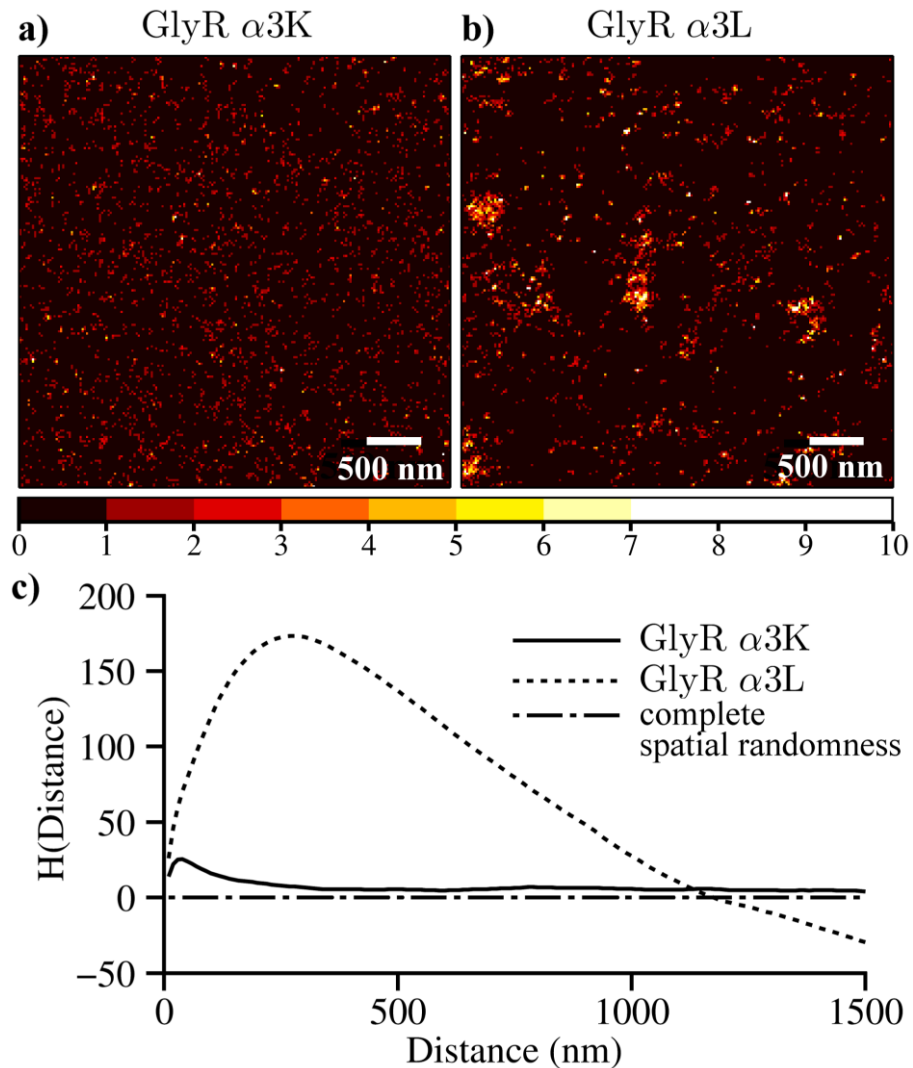


Figure 2.3: Super-resolution clustering analysis of the GlyR $\alpha 3$.

Representative accumulated point map images obtained from respectively the GlyR $\alpha 3K$ (a) and the GlyR $\alpha 3L$ (b) in fixed HEK 293 cells using dSTORM. Both images have the same intensity scale. Ripley's multi-distance spatial clustering analysis (c) reveals profound clustering of the GlyR $\alpha 3L$ compared to the GlyR $\alpha 3K$.

2.4.2 Study of GlyR $\alpha 3$ diffusion using ensemble techniques

FRAP experiments analyzed using the uniform disk model and the new reference method yielded a diffusion coefficient of $0.15 \pm 0.01 \mu\text{m}^2/\text{s}$ with a mobile fraction of 0.93 ± 0.04 for the GlyR $\alpha 3K$ (Figure 2.4a). Variations in ROI size did not reveal changes in diffusion coefficient (Figure 2.4c) nor in mobile

fraction (data not shown). Unfortunately, due to the low density of the bright clusters from GlyR $\alpha 3L$, applying FRAP to this isoform was unsuccessful (**Figure 2.4b**). Movement of these bright clusters in and out of the bleach region dramatically affects the recovery curve and renders it unsuitable for further analysis.

Analysis of diffusion measurements carried out with RICS reveals a difference in diffusion coefficient of more than an order of magnitude between the GlyR $\alpha 3K$ and $\alpha 3L$ (respectively $0.11 \pm 0.02 \mu\text{m}^2/\text{s}$ and $0.008 \pm 0.002 \mu\text{m}^2/\text{s}$). Coarse spatial mapping of receptor diffusion in the bottom membrane, displays variations that are relatively small compared to the inter-isoform difference (**Figure 2.5a, b**). Application of several scan speeds confirmed that no faster moving fraction of both types of receptors existed.

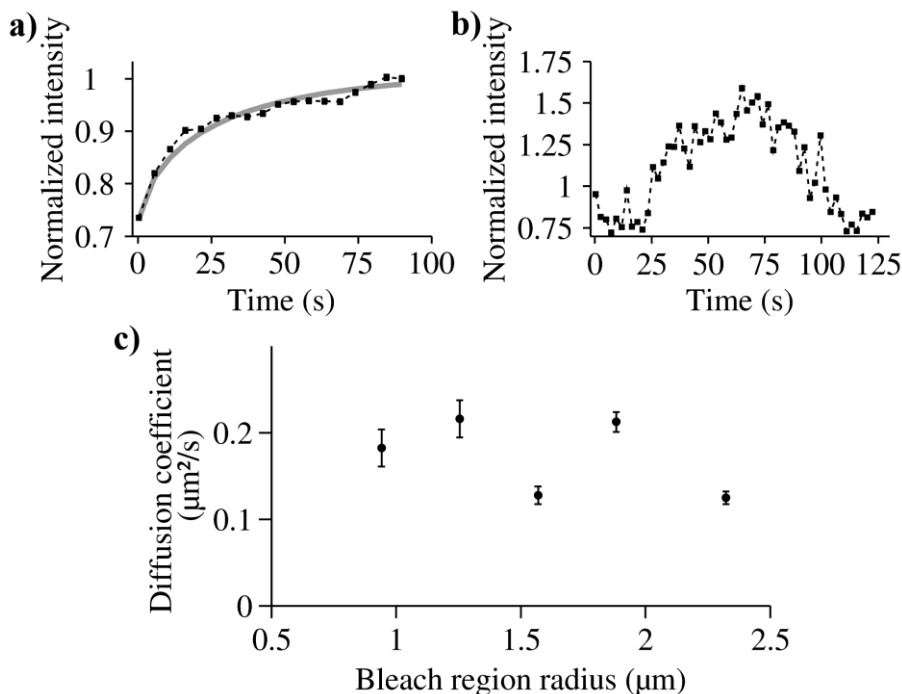


Figure 2.4: Fluorescence recovery after photobleaching of the GlyR $\alpha 3$.

Representative fluorescence recovery from respectively GlyR $\alpha 3K$ and $\alpha 3L$ expressed in HEK 293 cells are shown by (a) and (b). For the GlyR $\alpha 3K$, the model properly fit the curve, while fitting the recovery curve of GlyR $\alpha 3L$ was unsuccessful. Diffusion coefficients for the GlyR $\alpha 3K$ obtained from 31 cells and analyzed using the uniform disk model are plotted as the average and standard deviation per ROI radius (c). The overall average of the diffusion coefficient is $0.15 \pm 0.01 \mu\text{m}^2/\text{s}$ and of the mobile fraction is 0.93 ± 0.04 .

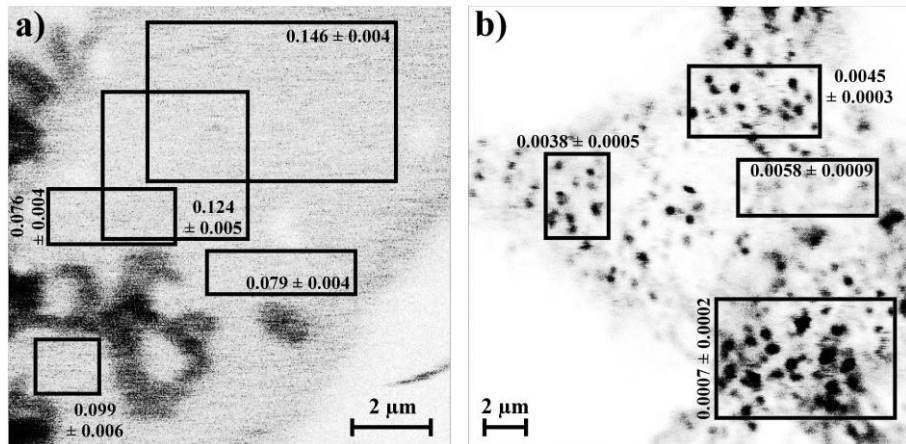


Figure 2.5: RICS of live HEK 293 cells expressing GlyR α 3K (a) and α 3L (b) allows for a coarse mapping of the mobility of the respective receptors.

Each white rectangular box represents an analyzed area with the obtained diffusion coefficient [in $\mu\text{m}^2/\text{s}$] and standard error reported. In general, there was a difference of over one decade between the diffusion coefficients of both splice variants. In addition, there was also variation of the diffusion coefficient within a single cell, albeit to a lesser extent. An identical color map was applied for both images.

TICS experiments performed on the GlyR α 3K and α 3L revealed that both splice variants contain two species of receptor diffusion (**Figure 2.6**). Due to bleaching and the limitations of the photobleaching correction, only the diffusion of the fastest species could be reliably characterized. The average values across the experiments for these species are $0.16 \pm 0.07 \mu\text{m}^2/\text{s}$ for the GlyR α 3K and $0.021 \pm 0.009 \mu\text{m}^2/\text{s}$ for the GlyR α 3L. In summary, all ensemble techniques yield similar diffusion coefficients for each individual isoform (**Table 2.2**).

Table 2.2: The average diffusion coefficient (in $\mu\text{m}^2/\text{s}$) as obtained per ensemble microfluorimetric technique.

Splice variant	FRAP	RICS	TICS
GlyR α 3K ^a	0.15 ± 0.01^c	0.11 ± 0.02	0.16 ± 0.07
GlyR α 3L ^b	Not Feasible	0.008 ± 0.002	0.021 ± 0.009

^a Cells analyzed per technique. FRAP: 31, RICS: 6, TICS: 6

^b Cells analyzed per technique. FRAP: 0, RICS: 6, TICS: 6

^c Errors are represented as standard error of the mean

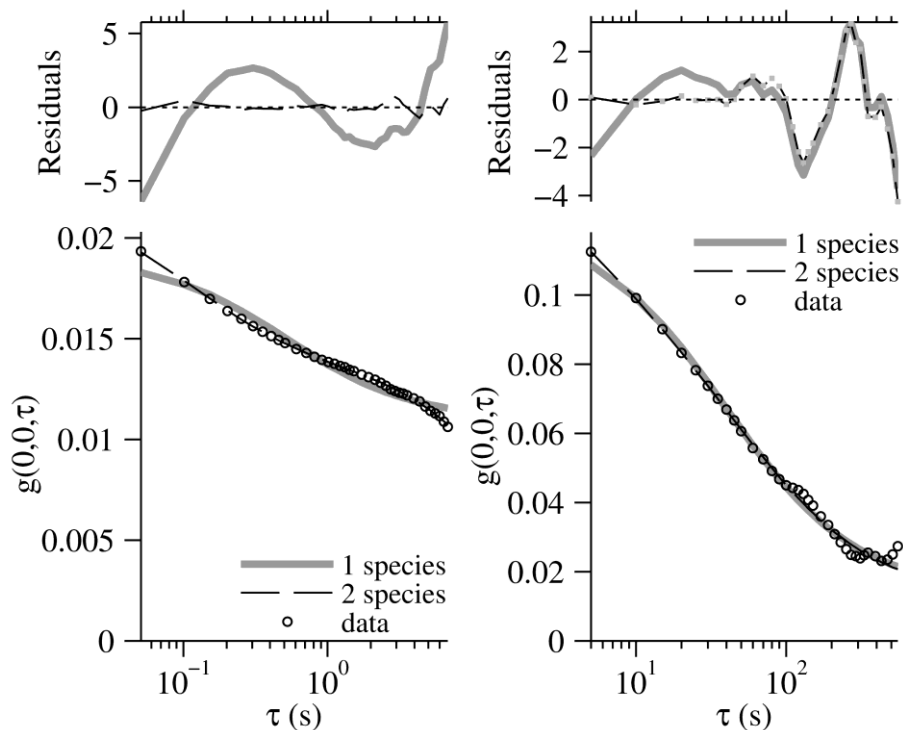


Figure 2.6: Temporal image correlation spectroscopy of the GlyR $\alpha 3$.

The temporal autocorrelation function obtained in TICS analysis of GlyR $\alpha 3K$ (a) and $\alpha 3L$ (b) are plotted, together with the 1 species and 2 species fit. The upper panels show the weighted residuals.

2.4.3 Study of the GlyR $\alpha 3$ diffusion using single particle tracking

The diffusing GlyR $\alpha 3$ isoforms were monitored by tracking individual fluorescent features in the bottom membrane (**Figure 2.7a, b**). The obtained distribution for short time range D_{1-3} is shifted towards faster diffusion for the GlyR $\alpha 3K$ compared to the GlyR $\alpha 3L$, with respective averages of $0.13 \mu\text{m}^2/\text{s}$ and $0.044 \mu\text{m}^2/\text{s}$ (**Figure 2.7c**). For longer time ranges, a time-dependent diffusion coefficient better suited the data. This implied that the average α -exponents were indicative of anomalous diffusion ($\alpha \neq 1$), equaling 0.87 for the GlyR $\alpha 3K$ and 0.73 for the GlyR $\alpha 3L$. The α -exponents exhibit a broad distribution due to imperfect sampling[194]. Nevertheless a clear distinction can be made between the GlyR $\alpha 3K$ and $\alpha 3L$. The distribution of the former has a zero skewness centered on normal diffusion ($\alpha = 1$), yet contains more weight on anomalous sub-diffusion ($\alpha < 1$) (**Figure 2.7d**). The distribution of the latter has positive non-zero skewness, with the center on anomalous sub-diffusion and with a long

tail to the right suggesting the presence of anomalous super-diffusion ($\alpha > 1$) (**Figure 2.7d**). For both receptor types a fraction of the analyzed trajectories was designated as immobile within the time-dependent diffusion model approach. This concerned 5% of the trajectories for the GlyR $\alpha 3K$ and 15% for the GlyR $\alpha 3L$ (**Table 2.3**).

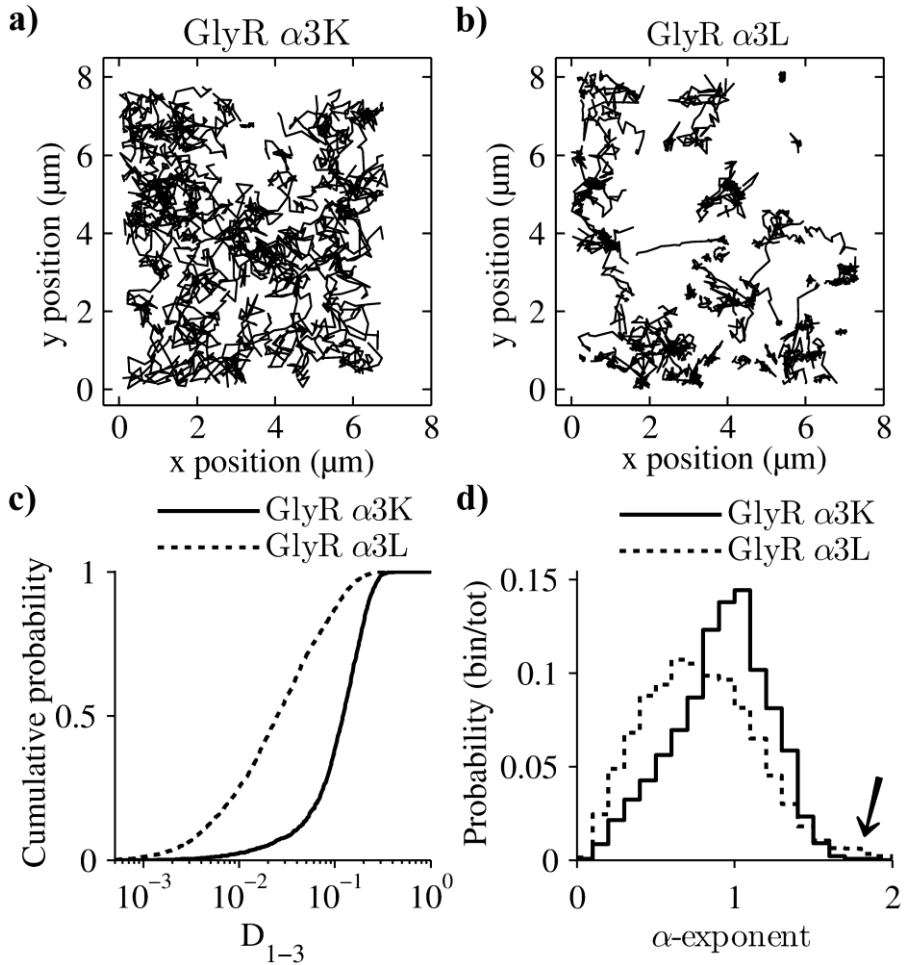


Figure 2.7: Single particle tracking ensemble analysis of the GlyR $\alpha 3$.

Representative trajectory plots, shown for the GlyR $\alpha 3K$ (a) and $\alpha 3L$ (b). Comparison of the cumulative distributions of short time range D_{1-3} shows faster overall diffusion for the GlyR $\alpha 3K$ compared to the GlyR $\alpha 3L$ (c). The distribution of α -exponents indicates anomalous sub-diffusion in both receptor populations (d). For the GlyR $\alpha 3L$, a subset of tracks also displays anomalous super-diffusion (arrow). (bin = number of elements in bin, tot = total elements in distribution)

Upon inspection of single trajectories, it can be ascertained that transient trapping is present for particles displaying tracks with anomalous sub-diffusion (**Figure 2.8a, b**). This was observed for both $\alpha 3K$ and $\alpha 3L$ receptors. On the other hand, tracks corresponding with anomalous super-diffusion reflect clear directed motion combined with local trapping (**Figure 2.8c, d**). The latter type of complex particle motion was only observed for the GlyR $\alpha 3L$.

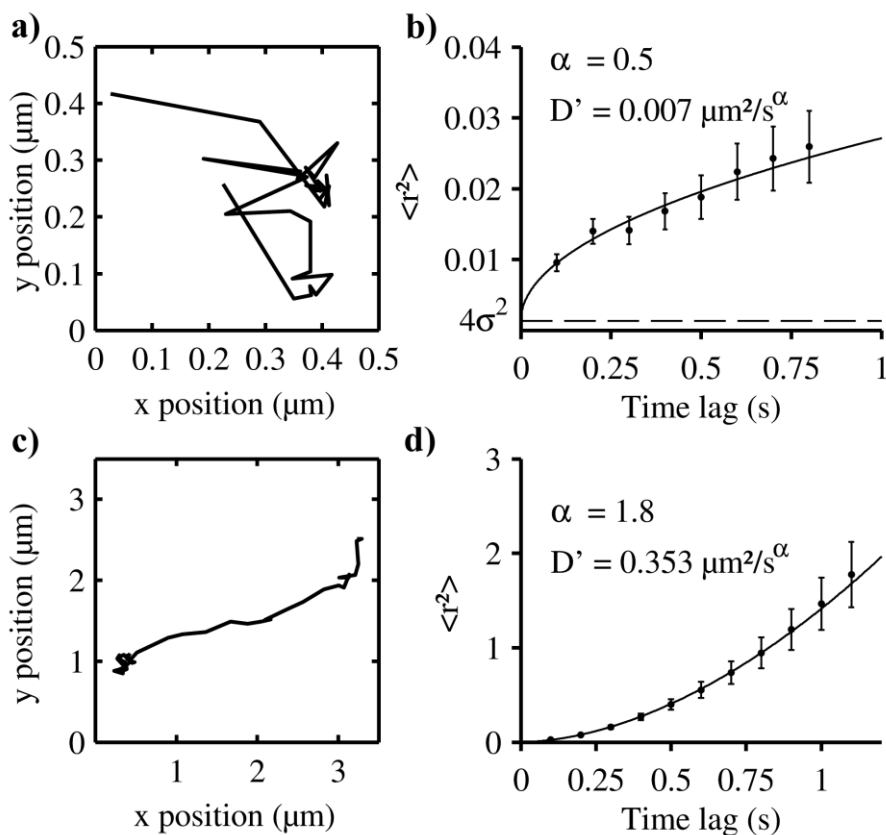


Figure 2.8: Single particle trajectory analysis of the GlyR $\alpha 3$.

To interpret the deviation from normal diffusion, representative tracks from particles with anomalous α -exponents are shown (a, c). Particles with an α -exponent < 1 exhibit diffusion with transient trapping (a), the localization precision is also represented (dashed line, b). Particles with an α -exponent > 1 show a heterogeneous displacement pattern (c), where the proportion of super-diffusion outweighs the sub-diffusion (d).

Table 2.3: Single particle tracking ensemble average parameters for the GlyR $\alpha 3$.

The average short time range D_{1-3} (in $\mu\text{m}^2/\text{s}$) are reported for both isoforms. The averages of the free fit parameters (D' , α -exponents) from the non-linear fit of diffusion at longer time range are represented together with the immobile fraction.

SPT	Short time range	Long time range		
		$\langle D' \rangle$	α -exponent	Immobile fraction ^d
Splice variant	$\langle D_{1-3} \rangle$			
GlyR $\alpha 3K^a$	0.129 ± 0.002^c	0.133 ± 0.003	0.866 ± 0.008	5%
GlyR $\alpha 3L^b$	0.0436 ± 0.0008	0.042 ± 0.001	0.736 ± 0.006	15%

a Number of cells measured: 7, number of trajectories analyzed: 1629

b Number of cells measured: 9, number of trajectories analyzed: 4291

c Errors are represented as standard error of the mean

d See materials and methods for criteria

2.5 Discussion

In this study, differential diffusion and aggregation of the homomeric GlyR $\alpha 3$ related to the isoform composition were investigated. The difference in aggregation states of the GlyR isoforms $\alpha 3K$ and $\alpha 3L$ was confirmed using ICS and dSTORM. The differences in receptor diffusion were studied with a variety of fluorimetric techniques. Further discussion pertains to the integrated view of receptor diffusion achieved by combining ensemble and single particle fluorimetric techniques. Finally, the results are placed in a physiological context and the perspectives for further study of the GlyR $\alpha 3$ are outlined.

2.5.1 The GlyR $\alpha 3$ isoforms differ in aggregation state

The difference between the diffuse staining pattern of GlyR $\alpha 3K$ and the punctate staining pattern of GlyR $\alpha 3L$ is obvious, even through regular microscopic observation. This differential staining pattern reflects the different aggregation state of both receptor isoforms. Eichler *et al.* estimated the cluster size of GlyR $\alpha 3L$ in transfected primary hippocampal neurons ($1.07 \pm 0.5 \mu\text{m}$), but the number of receptors per cluster could not be determined.[170] In order to estimate this number and to enable the detection of even smaller differences in aggregation state, the application of ICS and dSTORM to the current expression systems was explored. Both methods start from a static snapshot of the cellular model obtained through chemical fixation.

The ICS results revealed that each GlyR $\alpha 3L$ cluster comprised on average 8 labeled receptors assuming the exclusive presence of individual receptors for GlyR $\alpha 3K$ and a constant brightness per receptor. When aggregation reduces this brightness, as could well occur by steric hindrance of bound antibody, 8 will be a lower limit. Furthermore, the size of the detected GlyR $\alpha 3L$ clusters was still below the diffraction limit, as indicated by the lack of increment of the average observation profile radius ω_0 retrieved in ICS (**Table 2.1**). This is consistent with the estimated number of labeled receptors in combination with the size of the GlyR, which should be close to the published 8.5 nm radial diameter of the structurally related nicotinic acetylcholine receptor.[288,289]

In addition to the diffraction-limited ICS, the super-resolution method dSTORM was applied to obtain sub-diffraction resolution images of the receptors. Analysis

of these data using Ripley's H-function indicates a clear difference in aggregation state between the isoforms. While the GlyR α 3L displays a non-uniform clustering distribution, any clustering seen with the GlyR α 3K is minimal and barely exceeds artifacts generated by the repeated localization of identical particles.[242] The maximum of Ripley's H-function cannot be used as a rigorous estimate of the mean cluster size as this maximum depends on the cluster separation.[239] Also, a distribution of cluster sizes cannot be excluded and the higher number of detected events for larger clusters can introduce a bias.

2.5.2 GlyR α 3 diffusion studied by ensemble techniques

The diffusion of GlyR α 3K was successfully studied by FRAP. Two models for free diffusion, which differ in their assumption of the shape of the bleaching beam, were cautiously applied. It is known that a model for free diffusion might yield incorrect results in presence of anomalous diffusion while apparently being correct based on the quality of the fit.[290] However, the low immobile fraction observed by both models in the experiments reflects the suitability of the free diffusion model and suggests that the motion of the GlyR α 3K receptors is close to that of free diffusion. Furthermore, for receptors undergoing anomalous diffusion, the immobile fraction would be much higher upon analysis with a constant diffusion coefficient. Finally, the lack of dependency of both D and the immobile fraction on the ROI size are also indicative for the absence or limited contribution of anomalous diffusion. The results of both models did not differ significantly. Unfortunately, GlyR α 3L could not be studied by FRAP due to the presence of clusters. Movement of clusters in and out the ROI dramatically affects the fluorescence intensity inside the ROI. A similar effect is seen when the concentration of fluorophores is too low.[291]

While RICS in a biological context is mainly used to measure the diffusion of proteins in the cytoplasm [271,292], this technique has been previously used by us to characterize diffusion of membrane components[285,293]. The low diffusion coefficients of membrane proteins force the application of low scan speeds near the limit of the capabilities of our CLSM set-up. Coarse spatial mapping achieved with RICS revealed a limited spatial dependency of the diffusion coefficient for each individual isoform over the cell surface.[272,285] In contrast to FRAP, RICS was able to measure the diffusion coefficient of both

isoforms, with a good agreement for both techniques for the K isoform. The difference in magnitude of the obtained diffusion coefficients of both isoforms is larger than expected based on their difference in aggregation state estimated with ICS and dSTORM. This provides evidence for an influence, not inherent to the receptors, such as the membrane constitution or submembranous structures.

TICS was originally applied on a CLSM [273], but the available frame rate would not allow to resolve the large, fast moving fractions of the proteins. Therefore, we used a TIRFM with a frame rate optimized for the time scale of the expected kinetics. From simulated data, it is shown that for the observed bleaching rate, the experimental data can be corrected appropriately so that reliable estimates for the diffusion coefficient of the fastest species can be obtained. The use of TICS revealed the presence of an apparent slower diffusing species, but due to the bleaching rate this information could not unambiguously be interpreted.

2.5.3 SPT reveals anomalous diffusion in GlyR α 3 diffusion

The short time range D_{1-3} derived from SPT confirm faster diffusion for the GlyR α 3K in comparison to the GlyR α 3L. This could be explained by cluster formation of α 3L receptors, as seen by ICS and dSTORM, resulting in large complexes exhibiting slow but normal membrane diffusion. However, the observation that for a longer time range the diffusion coefficient becomes time-dependent, suggests that a larger hydrodynamic radius due to clustering of the GlyR α 3L cannot be the only determining factor. The average of the α -exponents ($\alpha < 1$) indicates that both receptor isoforms undergo sub-diffusion. The fact that this is more pronounced for the GlyR α 3L, which also displays a larger immobile fraction and a higher degree of clustering, supports the idea of local transient trapping of receptors in small regions.[199,294] This can be qualitatively confirmed by visual inspection of the GlyR α 3L tracks. A lower degree of sub-diffusion for the GlyR α 3K could indicate that these receptors are transiently trapped in larger regions. However, the size and the distribution of these regions has to be consistent with the nearly uniform distribution of the GlyR α 3K observed with dSTORM. An alternative assumption is that the α 3K isoform is less prone to trapping and therefore resides less in the trapped state. A higher degree of interaction determining the motion of GlyR α 3L is corroborated by the presence of anomalous super-diffusion[295] in the receptor motion. The

combination of trapping and super-diffusion, as found in the trajectories of the GlyR $\alpha 3L$, is likely to represent receptors actively being transported from, to or between different locations in the membrane.

2.5.4 An integrated view of receptor diffusion

Given the spatio-temporal properties of the GlyR $\alpha 3$ diffusion, SPT allowed for the most detailed characterization. However, the possible presence of bias inherent to SPT or the application of SPT to live cells warrants a combination with ensemble techniques. A first aspect is that highly mobile particles are more difficult to track compared to their slower moving counterparts, meaning a possible bias towards types of sub-diffusion can be present. Upon observation of sub-diffusion, as for the GlyR $\alpha 3$, a comparison with FRAP experiments is of importance, to estimate the relevance on the cellular level. In the instance of the GlyR $\alpha 3K$ this revealed a minimal impact of the sub-diffusion measured by SPT, on large scale receptor motion measured with FRAP.[290] Second, due to the bleaching of the particles, a bias towards fresh molecules diffusing into the bottom membrane from outside the measurement plane can arise. A comparison of the diffusion parameters measured with techniques requiring minimal measurement bleaching, such as TICS and FRAP, can resolve whether representative fractions are measured. In our case a good agreement between diffusion coefficients from single molecule tracking (D_{1-3}) and ensemble techniques was found. Moreover, a good agreement between the immobile fractions measured with FRAP and SPT was measured. Furthermore, coarse spatial mapping with RICS confirmed homogeneous diffusion patterns on the cellular level. Third, in choosing cells for SPT measurements, a selection bias can occur towards cells yielding the highest fluorescence signal or containing bright fluorescent entities. Cells showing an overall high level of protein expression after transfection are usually unhealthy[296] and the presence of bright fluorescent entities can bias particle detection parameters. Again, comparing the results obtained with SPT to those obtained with ensemble techniques, where cells are selected based on the ensemble fluorescence signal, decreases the risk of biased sampling. Exemplary is the detection of multiple species with TICS, which confirms that the complex GlyR $\alpha 3$ motion found with SPT is not a technique related artifact.

2.5.5 Perspectives for the GlyR $\alpha 3$

The diffusion coefficients reported here for the GlyR $\alpha 3$ are within the range expected for proteins diffusing in the cell membrane.[63,73] However, experimental parameters such as the applied cell line, measurement temperature and time of measurement, given their influence on membrane viscosity, thermal agitation, expression level and molecular interactions, are key factors when comparing protein diffusion. Variations in these parameters hamper a comparison with reported values for other GlyR subtypes.[150-152] Nevertheless the results can be placed in a biological context. Receptor diffusion plays an essential role in neuronal function as it allows for renewal of receptors in the desensitized state and regulation of postsynaptic receptor pool size.[258,297] Homomeric GlyR $\alpha 3K$ channels were shown to contribute to tonic inhibition of neuronal excitability, which requires receptors in the non-desensitized state.[168,169] Compared with $\alpha 3L$, GlyR $\alpha 3K$ desensitizes more rapidly[167] and, therefore, its faster diffusion makes sense as it increases the probability of receptor cycling between endocytic and cell plasma membrane compartments, which will facilitate receptor renewal.[258] Furthermore, this study adds to the understanding of receptor desensitization mechanisms. In fact, it was shown that increased GlyR $\alpha 1$ receptor density in gephyrin-dependent clusters facilitates desensitization, whereas in case of GlyR $\alpha 3L$ just the opposite was observed.[167,171] Thus, GlyR clustering is not a universal mechanism of desensitization but also involves receptor conformation depending on primary structure or receptor associated proteins other than gephyrin.[97,298]

A next step towards understanding the role of RNA splicing in GlyR $\alpha 3$ function will be the identification of proteins that interact with the RNA splice insert TEAFALKFYRFSDT located in the large cytosolic loop between transmembrane domains 3 and 4 of GlyR $\alpha 3L$. A similar fluorimetric strategy as formulated here can be used to explore different biological settings. Pharmacological breakdown of the cytoskeleton has been shown to influence GlyR dynamics in cultured neurons.[151,152] Another option is depleting membrane cholesterol, thereby influencing the different types of lipid rafts which have been reported in HeLa cells.[236] Disturbance of lipid rafts can lead to dissociation of raft induced protein aggregation and altered protein function.[299,300] An alternative

approach for studying GlyR $\alpha 3$ interactions involves site-directed mutagenesis of the insert region. This has previously been applied for studying the regulatory capabilities of the splice insert on channel gating and domain structure.[174] By probing all these conditions, mechanisms determining the GlyR $\alpha 3$ behavior can be better understood.

An appropriate exploratory strategy for examining any transmembrane protein should maximize efficiency in screening multiple conditions and minimize the risk of overlooking any changes in receptor behavior. Therefore labor intensity, applicability and spatio-temporal sampling should be considered when developing a screening approach. This report offers a strong foundation for making these considerations.

2.6 Supplementary material: Expression and functionality check of glycine receptors

2.6.1 Western blot

The heterologous expression of GlyR α 3K and α 3L was compared with the expression of wild type GlyR by means of western blot analysis. For each condition, 3 million cells were plated in small culture flasks (25 cm²). Transfection of the cells occurred as described above. After 24 hours of transfection, cells were rinsed with cold (4°C) phosphate buffered saline (PBS) and trypsinated. The cell suspensions were centrifuged and rinsed again with PBS. After a second centrifugation step, cells were lysed by addition of RIPA buffer (Sigma-Aldrich, Bornem, Belgium). Protein concentrations were determined using the BCATM Protein Assay kit (Pierce, Rockford, IL, USA). For each condition, 10, 25 and 50 μ g of total protein content was subjected to precast 8% Novex® Tris-Glycine gel electrophoresis using an XCell SureLockTM Mini-Cell. The proteins were subsequently transferred onto a nitrocellulose transfer membrane via the iBlotTM Dry blotting System (Invitrogen/Molecular Probes). After blocking with 2% non-fat milk in PBS (overnight at 4°C), the membranes were incubated with mAb4a (1:500, Pfeiffer *et al.* 1984, Synaptic Systems, Goettingen, Germany) followed by a peroxidase-conjugated secondary antibody (Rabbit anti-mouse 1:1000, Dakocytomation, Heverlee, Belgium) and finally the bands were visualized using a 3,3'-Diaminobenzidine (DAB, Sigma-Aldrich).

2.6.2 Electrophysiology

Cells seeded in 35 mm dishes, were transfected as described above and whole-cell patch-clamp recordings were performed (EPC 10, HEKA Elektronik, Lambrecht, Pfalz, Germany). The standard extracellular solution for HEK cells (HES) had a composition of (in mM) 150 NaCl, 5.4 KCl, 2 CaCl₂, 1 MgCl₂, 10 HEPES, and 10 glucose (Sigma-Aldrich). The intracellular solution (HIS) contained (in mM): 120 CsCl, 2 Na₂ATP, 2 MgATP, 10 EGTA, and 10 HEPES. To measure the dose-response to glycine, different glycine concentrations (1 μ M, 10 μ M, 30 μ M, 100 μ M, 300 μ M and 1 mM) in HES were bath-applied onto the cell surface during 10 s at a holding potential of -60 mV. The average

normalized maximum current as a function of concentration was fit to the *Hill* equation to yield the EC_{50} of both splice variants (GraphPad Prism, La Jolla, CA, USA). The desensitization of the responses was measured by fitting a mono-exponential to the desensitization phase of the glycine response at room temperature.

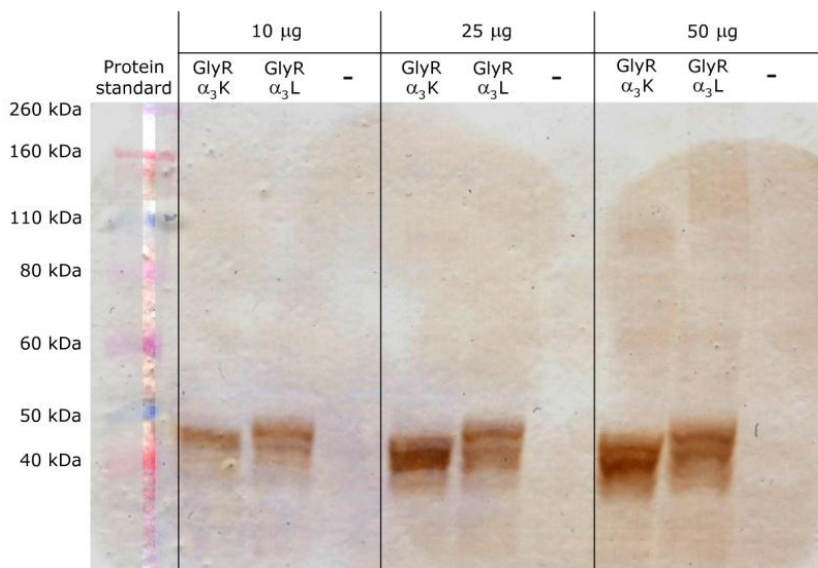


Figure 2.9: Expression of the GlyR α_3 isoforms in HEK 293 cells.

The expression of both GlyR α_3 K and α_3 L subunits after transfection was confirmed using western blot. The band of both receptors is located between 40 and 50 kDa, as expected. Furthermore, due to the extra amino acids, the band of GlyR α_3 L is located at higher molecular weights as compared to GlyR α_3 K. The antibody mAb4a was used to recognize all GlyRs present in the cell lysates. No significant expression was detected of endogenous GlyRs by wild-type HEK 293 cells. (The contrast of a small stripe of the protein standard lane was digitally enhanced to improve the visualization of the protein standard.)

2.6.3 Functional GlyR α_3 expression in HEK 293 cells

Expression of both heterologous HA-GlyR α_3 isoforms was confirmed by western blot analysis (**Figure 2.9**). The measured molecular weight of the receptors between 40 and 50 kDa is as expected, with the band of GlyR α_3 L slightly elevated compared to that of GlyR α_3 K due to the presence of extra amino acids [108,116]. No endogenous GlyR expression is found by the mAb4a antibody, which recognizes an endogenous epitope common to all glycine receptor α -subunits [106,301,302].

The functionality of the expressed receptors was evaluated by whole-cell patch-clamp. Current traces exhibited a dose-dependent response to glycine for both subunit isoforms, with an EC₅₀ of $47 \pm 10 \mu\text{M}$ ($n=6$) for GlyR $\alpha 3\text{K}$ and $52 \pm 24 \mu\text{M}$ ($n=6$) for GlyR $\alpha 3\text{L}$ (**Figure 2.10a, b, c**). The time constant (τ) of the receptor desensitization for the HA-GlyR $\alpha 3\text{L}$ ($\tau = 7.86 \pm 0.09 \text{ s}$ at $100 \mu\text{M}$ and $5.3 \pm 0.7 \text{ s}$ at $300 \mu\text{M}$ glycine) was significantly longer as compared to the HA-GlyR $\alpha 3\text{K}$ ($\tau = 2.3 \pm 0.9 \text{ s}$ at $100 \mu\text{M}$ and $1.8 \pm 0.4 \text{ s}$ at $300 \mu\text{M}$ glycine) (**Figure 2.10d**). This is in agreement with published results [167].

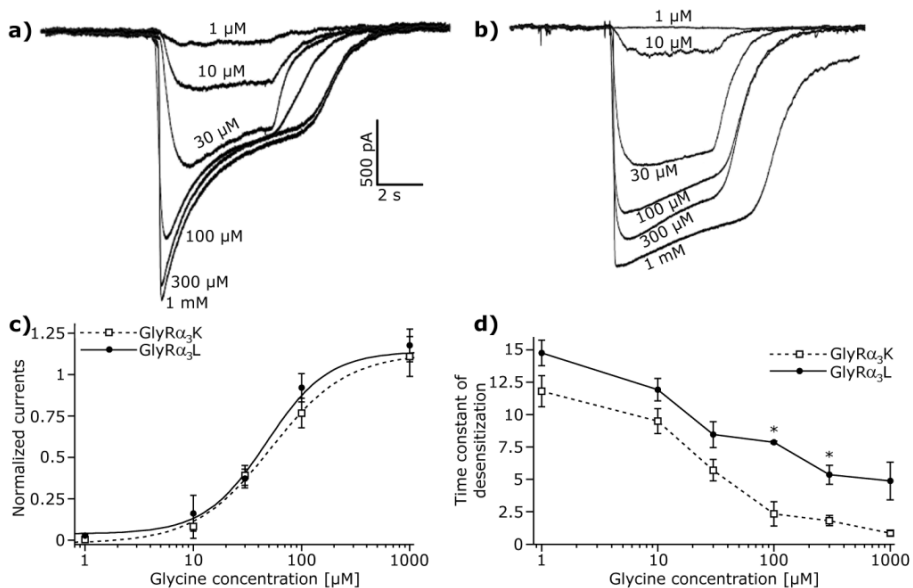


Figure 2.10: Electrophysiology of the GlyR $\alpha 3$ isoforms.

Current traces of responses were induced by different concentrations of glycine for GlyR $\alpha 3\text{K}$ (a) and GlyR $\alpha 3\text{L}$ (b). The dose-response curve of both receptors is shown in (c). Mean values \pm SEM are plotted. A non-linear fit according to the Hill equation revealed an EC₅₀ of $47 \pm 10 \mu\text{M}$ and Hill slope 1.5 ($n=6$) for the K splice variant and an EC₅₀ $52 \pm 24 \mu\text{M}$ and Hill slope 1.2 ($n=6$) for the L splice variant. The time constant of the desensitization as a function of the glycine concentration of the two isoforms is plotted in (d). A dose-dependent desensitization was present. Moreover, GlyR $\alpha 3\text{L}$ desensitized more slowly than GlyR $\alpha 3\text{K}$. (*: $P < 0.05$)

3 Analysis of $\alpha 3$ GlyR single particle tracking in the cell membrane

Kristof Notelaers, Susana Rocha, Rik Paesen, Nick Smisdom, Ben De Clercq, Jochen C. Meier, Jean-Michel Rigo, Johan Hofkens, Marcel Ameloot

Journal:

Biochimica et Biophysica Acta (BBA) - Molecular Cell Research 2014

Volume 1843, Issue 3, Pages 544-553

doi: 10.1016/j.bbamcr.2013.11.019

3.1 Abstract

Single particle tracking (SPT) of transmembrane receptors in the plasma membrane often reveals heterogeneous diffusion. A thorough interpretation of the displacements requires an extensive analysis suited for discrimination of different motion types present in the data. Here the diffusion pattern of the homomeric $\alpha 3$ -containing glycine receptor (GlyR) is analyzed in the membrane of HEK 293 cells. More specifically, the influence of the $\alpha 3$ RNA splice variants $\alpha 3K$ and $\alpha 3L$ on lateral membrane diffusion of the receptor is revealed in detail. Using a combination of ensemble and local SPT analysis, free and anomalous diffusion parameters are determined. The GlyR $\alpha 3$ free diffusion coefficient is found to be $0.13 \pm 0.01 \mu\text{m}^2/\text{s}$ and both receptor variants display confined motion. The confinement probability level and residence time are significantly elevated for the $\alpha 3L$ variant compared to the $\alpha 3K$ variant. Furthermore, for the $\alpha 3L$ GlyR, the presence of directed motion was also established, with a velocity matching that of saltatory vesicular transport. These findings reveal that $\alpha 3$ GlyRs are prone to different types of anomalous diffusion and reinforce the role of RNA splicing in determining lateral membrane trafficking.

3.2 Introduction

The trafficking of proteins after insertion in the cell membrane is crucial for cell homeostasis and functionality [249,251,303]. Rudimentary movement of membrane proteins is governed by Brownian motion and can be modeled as diffusion in a 2D fluid plane [14]. The corresponding diffusion coefficient is dependent on the temperature, the radius of the membrane-spanning segment and the membrane viscosity [61,63]. Diffusion is a stochastic process, yet several cellular mechanisms exist which are capable of steering protein movement in the cell membrane [253-255,304]. The movement of proteins susceptible to these mechanisms deviates from normal diffusion and is termed anomalous diffusion [305-307]. Deviations from normal diffusion can signify either a restriction of protein diffusion in space or non-random travel of proteins along an imposed path. The former is termed sub-diffusion, hindered diffusion or confined motion, while the latter is termed super-diffusion, flow or directed motion [295,308-310].

Anomalous diffusion is frequently revealed when studying the dynamics of membrane proteins [73,311]. Especially the increasing application of Single Particle Tracking (SPT) has furthered the understanding of protein trafficking in the membrane [192,204]. SPT has given access to nanometer accuracy on millisecond time-scales, allowing the monitoring of fast protein dynamics with high spatial resolution [184,194,312,313]. When monitoring a transmembrane receptor in a complex biological system, it is important to correctly represent and quantify the SPT data. Therefore, many efforts have already gone into the representation of SPT data and determination of an appropriate diffusion model [308,314,315].

In synaptic biology, anomalous diffusion of membrane proteins has been monitored extensively using SPT [316]. Effective neurotransmission requires neurotransmitter receptors to be located at the postsynaptic membrane and a turnover of these receptors to maintain sensitivity [137,258,317]. These properties impose a strong regulation of neurotransmitter receptor trafficking and lateral mobility. For many neurotransmitter receptors, interacting proteins have been identified which form scaffolds or chaperones [149,318-321]. In order to elucidate the nature of these interactions, accurate quantification of receptor diffusion is crucial [152,322].

The glycine receptor (GlyR) is a neurotransmitter receptor of the cys-loop ligand-gated ion channel (LGIC) family [122]. It functions as a pentameric chloride channel, leading to developmentally regulated neuronal hyperpolarisation upon activation [138,323]. The GlyR $\alpha 3$ has attracted significant attention as it is involved in inflammatory pain sensitization [163]. Nevertheless, little is known about the molecular basis governing membrane diffusion of the GlyR $\alpha 3$. From the *GLRA3*-gene transcript, two $\alpha 3$ -subunit variants are generated via post-transcriptional processing [167]. These variants are identified as the short $\alpha 3K$ and long $\alpha 3L$ GlyR, with the latter containing an extra 15 amino acid insert in the large intracellular loop between transmembrane segments 3 and 4 (TM 3-4). This protein region is instrumental to receptor trafficking and regulation of synaptic localization [170], receptor desensitization [167] and channel gating [174]. In the hippocampus of patients with temporal lobe epilepsy, GlyR $\alpha 3L$ is the preponderant RNA splice variant [166,168]. Detailed knowledge about the (anomalous) diffusion properties of the GlyR $\alpha 3$ RNA splice variants and how they function and dysfunction will advance our understanding of pathogenic mechanisms in epilepsy and inflammatory pain sensitization.

In previous work, a variety of nano- and micro-fluorimetric techniques were used to characterize homomeric $\alpha 3$ GlyR diffusion and aggregation on multiple time and length scales [324]. The results showed RNA splice variant dependent aggregation of $\alpha 3$ GlyRs, accompanied by differential diffusion dynamics. The measurements done on short time and length scales, especially by SPT, indicated that the differential diffusion dynamics are associated with anomalous diffusion. The results showed the putative presence of confined GlyR $\alpha 3$ motion, with additional directed motion for $\alpha 3L$. In this work, the GlyR $\alpha 3$ anomalous diffusion is verified and quantified by focusing on the SPT analysis. After determination of the free diffusion coefficient, confined and directed motion were identified by local displacement analysis [325,326]. This was based on respectively the displacement size and the asymmetry of the trajectories. By providing a detailed view on GlyR $\alpha 3$ motion in the cell membrane, valuable insights on RNA splicing dependent dynamics are acquired.

3.3 Materials and methods

3.3.1 Single particle tracking

Single particle tracking experiments were executed as described elsewhere [324]. Briefly, transient transfection of HEK 293 cells by calcium phosphate co-precipitation was used for the expression of HA-tagged $\alpha 3K$ and $\alpha 3L$ splice variants of the mouse GlyR $\alpha 3$. After 24 hours the receptors were labeled using a polyclonal anti-HA antibody directly labeled with Alexa 647. Images of the bottom membrane were acquired at 10 Hz using total internal reflection fluorescence (TIRF)-microscopy with an EM-CCD camera, while the cells were incubated at 37°C. Particle detection, trajectory reconstruction and all consequent analysis were performed by in-house developed MATLAB® (R2010b, The Mathworks, Gouda, The Netherlands) routines. Only particle trajectories with at least 16 consecutive displacements were considered and the average localization precision (σ) was 18 nm. In subsequent analysis immobile trajectories were not removed and σ was kept fixed.

3.3.2 Ensemble displacement analysis

In order to quantify GlyR diffusion on the ensemble level, the mean square displacement (MSD) was determined from the cumulative distributions of square displacements over consecutive time lags. A single-component function failed to accurately describe the data and therefore fitting was done with a two-component function (see supp. mat. S1) [327]:

$$P(r^2, t) = 1 - \sum_{i=1,2} A_i \exp\left(-\frac{r^2}{r_i^2}\right) \sum_{i=1,2} A_i = 1 \quad (3.1)$$

For each time lag this equation yields two MSD (r^2) with $r_1^2 > r_2^2$ and two respective fractions (A_1, A_2). Fitting of the first component was done with a linear function, representing a free diffusion model, yielding D_e :

$$\langle r^2 \rangle = 4D_e t + 4\sigma^2 \quad (3.2)$$

For the second component a non-linear model was used, representing an anomalous diffusion model, yielding a transport factor D'_e and anomalous exponent α_e :

$$\langle r^2 \rangle = 4D_e' t^{\alpha_e} + 4\sigma^2 \quad (3.3)$$

In case of $\alpha_e < 1$ the particle undergoes sub-diffusion, in case of $\alpha_e > 1$ the particle is subjected to super-diffusion.

3.3.3 Local displacement analysis

To determine sections of trajectories displaying confined or directed motion, each trajectory was analyzed in a sliding segment fashion. The sliding window parameters for section identification are scaled to the minimum number of time lags in a trajectory ($N = 16$). Parameter values for confined and directed motion identification are selected based on the nature of the respective anomalous process, as further explained below. The final thresholds were selected based on detecting $\leq 0.1\%$ anomalous displacements in the simulated data (SM **Figure 3.8**).

3.3.4 Confined motion

In order to detect confined motion, the method as described by Simson R. *et al.* was applied [326]. To this end the cumulative probability $\Psi(R,t)$, *i.e.* the probability of a diffusing particle staying in a region R as a function of time t , was determined as follows [197]:

$$\log(\Psi) = 0.2048 - 2.5117 Dt/R^2 \quad (3.4)$$

The parameter D_e from the ensemble displacement analysis was used as an estimate for D . R^2 was determined for each segment as the maximum squared displacement from the initial point of that segment. The time span of the sliding segment was 8 time lags ($t = 0.8$ s), which gave robust averaging for even the shortest trajectories. The confinement probability was transformed into a confinement probability level (L_c) according to:

$$L_c = \begin{cases} -\log(\Psi) - 1 & \Psi \leq 0.1 \\ 0 & \Psi > 0.1 \end{cases} \quad (3.5)$$

For each displacement, an individual L_c was determined by averaging over all segments containing the displacement. In order to be considered as a confinement region, a minimum of 10 consecutive displacements were required

to have $L_c > 1.6$, corresponding to $\Psi(R, t) = 0.0025$. Each confinement region was quantified by the radius (ρ) of the smallest circle enclosing all corresponding confined displacements and the *residence time* was determined by the time span of the confined trajectory section.

3.3.5 Directed motion

Directed motion was identified by analyzing the asymmetry of the ellipse of gyration[328], calculated over segments of 6 time lags. This was chosen as a compromise between averaging and short time scale sensitivity. The asymmetry parameter (a_2), becomes 0 for linear trajectories and 1 for circular trajectories and is calculated as follows:

$$a_2 = R_2^2/R_1^2 \quad (3.6)$$

with R_1^2 and R_2^2 being the major and minor eigenvalues, respectively, of the radius of gyration tensor (T) calculated from the x and y position of the particle throughout the segment:

$$T = \begin{pmatrix} \frac{1}{N} \sum_{j=1}^N (x_j - \langle x \rangle)^2 & \frac{1}{N} \sum_{j=1}^N (x_j - \langle x \rangle)(y_j - \langle y \rangle) \\ \frac{1}{N} \sum_{j=1}^N (x_j - \langle x \rangle)(y_j - \langle y \rangle) & \frac{1}{N} \sum_{j=1}^N (y_j - \langle y \rangle)^2 \end{pmatrix} \quad (3.7)$$

The cumulative probability of a_2 [$Pr(a_2)$] occurring for a randomly diffusing particle was interpolated from values given by Saxton M.J.[197]. A directed motion probability level (L_d) was calculated for values of a_2 within the provided range of $Pr(a_2)$:

$$L_d = \begin{cases} -\log(Pr(a_2)) - 0.3578 & Pr(a_2 \leq 0.43871) \\ 0 & Pr(a_2 > 0.43871) \end{cases} \quad (3.8)$$

An individual L_d for each displacement was determined, by averaging over all segments containing the displacement. In order for a section to be considered as directed motion, a minimum of 7 consecutive displacements were required to have $L_d > 1.52$, corresponding to $Pr(a_2) = 0.0132$. Furthermore, asymmetrical

displacements also exhibiting confinement ($L_c > 1.6$) were eliminated. Finally, the resulting sections were required to show a net square displacement exceeding the mean square displacement given by the time span of the section and D_e (Eq. 3.2). The quantification of the identified directed motion was done by calculating the *distance*, *travel time* and *speed* of the directed motion sections. The *distance* was determined by the sum of all first order displacements. The *travel time* was determined by the time span. The *speed* was obtained by dividing *distance* by *travel time*. The *prevalence* of confined and directed motion was determined by the percentage of trajectories displaying the respective motion type. Furthermore, for confined motion, the *confined fraction* is determined by the percentage of confined displacements. A displacement is considered confined only when it belongs to a confined trajectory section.

3.3.6 Statistics

The individual output parameters reported in this work are represented either by showing the full distribution and/or the mean with standard error. The full distributions are made up by grouping all values for the corresponding parameter over all experiments from a single expression system. The range reported for each distribution is the 1st to the 99th percentile. Unless stated otherwise, the mean with standard error for a parameter is calculated by averaging the mean parameter value from each individual experiment (n) for a single expression system. For the $\alpha 3K$ -variant 7 cells were measured ($n = 7$) generating 1629 trajectories, while for the $\alpha 3L$ -variant 9 cells were measured ($n = 9$) generating 4291 trajectories. Statistically significant differences were evaluated by means of a t-test.

3.4 Results

The influence of RNA splicing on GlyR $\alpha 3$ biophysical membrane behavior was investigated by analyzing separate SPT measurements of both splice variants $\alpha 3K$ and $\alpha 3L$. First multi-component ensemble analysis was performed to assess the possible presence of anomalous diffusion and to determine the free diffusion coefficient. Next a local displacement analysis was applied to detect individual deviations from free diffusion, incorporating the previously determined value of the free diffusion coefficient. The presence of both confined and directed motion is established and quantified. In a last step, the coincidence of these two motion types was evaluated.

3.4.1 Multi-component ensemble analysis

The $\alpha 3K$ GlyR square displacement distribution for each individual experiment could be accurately fit with a two-component function for consecutive time lags (Eq. 3.1). The first component showed a linear relationship between the MSD and time over consecutive time lags. This was characterized by a free diffusion model with $D_e = 0.13 \pm 0.01 \mu\text{m}^2/\text{s}$ according to eq. 3.2 (**Figure 3.1A**). The MSD of the second component could only be fitted with an anomalous diffusion model, according to eq. 3.3. The recovered parameters were $\alpha_e = 0.62 \pm 0.06$ and $D'_e = (5.0 \pm 0.5) \times 10^{-3} \mu\text{m}^2/\text{s}^\alpha$ (**Figure 3.1B**). The fractions are stable on the time scale of the analysis and reveal that the fraction of the first component dominates over that of the second component (**Figure 3.1C**). In case of the $\alpha 3L$ square displacement distribution, a two-component function did not accurately describe the data. Using a three-component function improved fitting, yielding a first component with $D_e = 0.09 \pm 0.01 \mu\text{m}^2/\text{s}$ according to eq. 3.2 (SM **Figure 3.7**). Given that in theory, the free diffusion coefficient for both variants should be similar, we decided to use D_e from $\alpha 3K$ GlyRs as the standard for free diffusion of $\alpha 3$ GlyRs. Moreover, using D_e from the $\alpha 3L$ GlyR had little impact on the subsequent local displacements analysis (SM **Figure 3.9**).

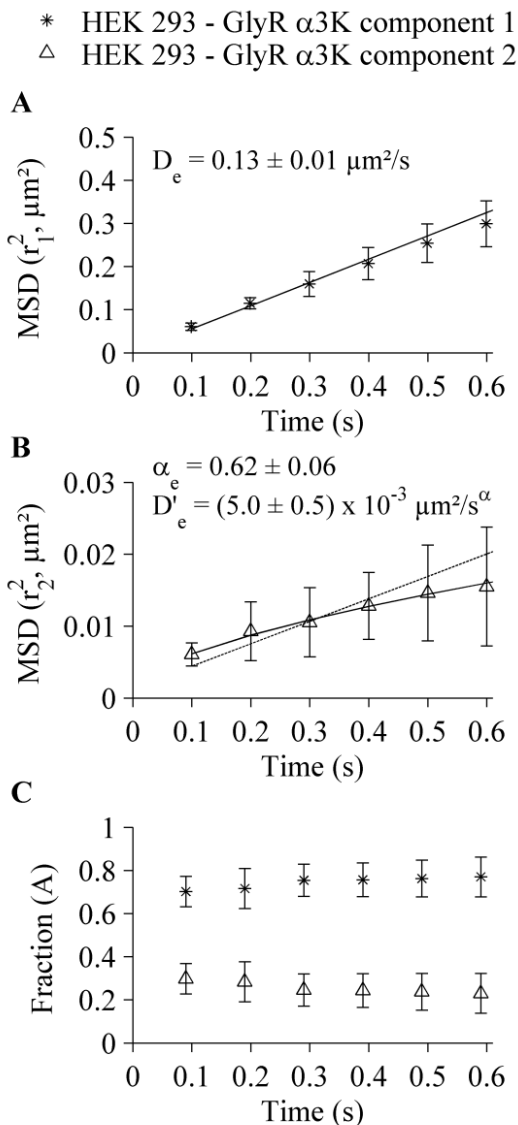


Figure 3.1: Ensemble displacement analysis of GlyR α 3K diffusion in HEK 293.

A two-component function (Eq. 3.1) was used, yielding two MSDs ($r_1^2 > r_2^2$) with their respective fractions (error bars represent standard deviation). A. The MSD of the first component over consecutive time lags. A free diffusion model (Eq. 3.2, full line) was applied to determine the diffusion coefficient (D_e , indicated with 95% confidence interval). B. The MSD of the second component over consecutive time lags. A free diffusion model was not suitable for quantification (dotted line). Instead an anomalous diffusion model was applied (Eq. 3.3, full line), with α_e characterizing the deviation from normal diffusion (α_e and D_e' indicated with 95% confidence interval) C. The relative fractions of each component in the ensemble population.

3.4.2 Local displacement analysis

In order to identify local deviations from normal diffusion, all trajectories were analyzed over a sliding window. Within the sliding window, the local displacement properties were calculated and compared to values expected for free diffusion. The analysis aimed at detecting both confined motion and directed motion. Confined motion was defined by regions where the receptors resided longer than expected for free diffusion. In order to identify these regions, L_c was determined, based on the ratio of the local maximum square displacement and D_e from the ensemble analysis (**Figure 3.2A**). In order to determine directed motion, the trajectory form was evaluated by the asymmetry of the gyration matrix T , used to calculate L_d (**Figure 3.2B**). In order for a trajectory section to be recognized as true directed motion, a minimum square displacement was also required.

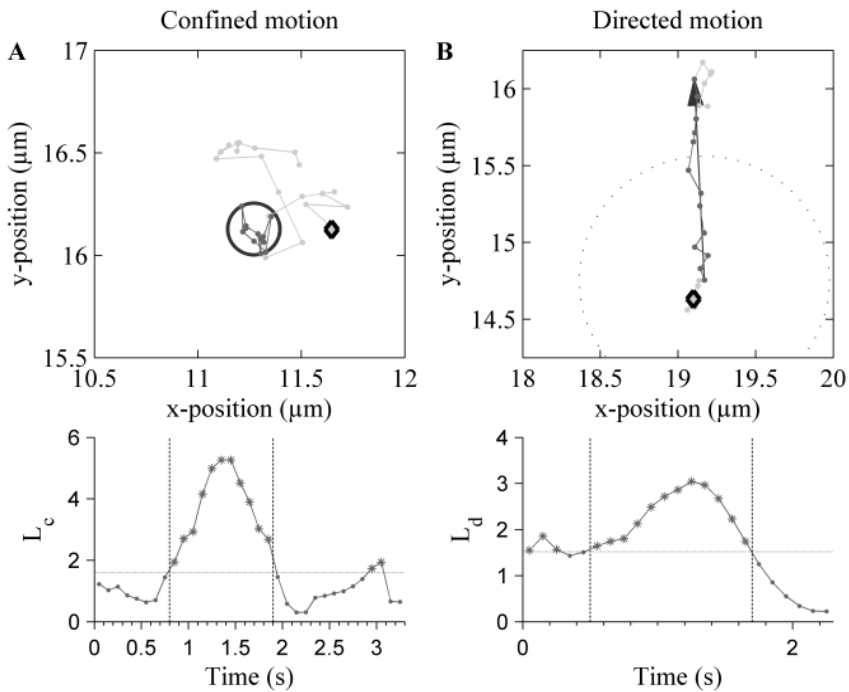


Figure 3.2: Identification of anomalous diffusion sections in GlyR trajectories using local displacement analysis.

A. Detection of confined motion based on the confinement probability level (L_c). Upper: Representative trajectory of the GlyR $\alpha 3K$ in HEK 293 cells containing a confinement region (circle). Lower: This region was identified by detecting trajectory sections with $L_c > 1.6$ (horizontal line, *) for at least 10

consecutive displacements (vertical lines). B. Detection of directed motion (arrow), based on the directed motion probability level (L_d). Upper: Representative trajectory of the GlyR $\alpha 3L$ in HEK 293 cells containing directed motion (arrow). The minimum displacement required for directed motion is also indicated (dotted circle). Lower: The directed motion was identified by detecting trajectory sections with $L_d > 1.52$ (horizontal line, *) for at least 7 consecutive displacements (vertical lines). The starting point of each trajectory is indicated (\diamond).

In order to visualize the results from the local displacement analysis, first a section of the membrane is selected (**Figure 3.3**). Plotting the trajectories in a color scheme indicating free diffusion (black), confined motion (red) or directed motion (green) shows that for the $\alpha 3K$ variant (117 tracks) there is mainly free diffusion with occasional entry to the confined state. For $\alpha 3L$ (223 tracks) on the other hand, confined motion is dominant, resulting in very localized trajectories covering only a small area of the membrane. Free diffusion and directed motion of this variant mainly occur around the areas of confinement. (**Figure 3.3A**). **Figure 3.3B** shows the appearance of confined and directed motion in time. Sections of confined (circles) or directed motion (lines) are represented by color coding according to the central frame of the occurrence. The markers do not reflect the exact spatial dimensions. However, it becomes clear, especially for the L-variant, that some membrane areas contain multiple events spaced in time (black rectangles). Furthermore the occurrences of the anomalous diffusion events are spread out over the full timescale of the recording. Mapping of L_c indicates that the more frequent occurrence of confined motion for $\alpha 3L$ is also coupled to higher values of L_c (**Figure 3.3C**). When observing the spatial pattern of L_c for $\alpha 3L$, small high intensity interspersed peaks can be observed (red rectangles). Interestingly these areas show strong overlap with membrane areas containing reoccurring confined motion.

In order to visualize the dynamics creating the irregular patterns of L_c in areas with reoccurring confined events, trajectories and L_c were mapped for short time intervals. This illustrates that steep gradients in confinement strength are found in the motion of individual trajectories, a phenomenon which can occur for several receptors in the same area (e.g. red box) spaced over time. The trajectories in these areas show a high presence of confined motion, occasionally transitioning to or from free diffusion or directed motion (**Figure 3.4**).

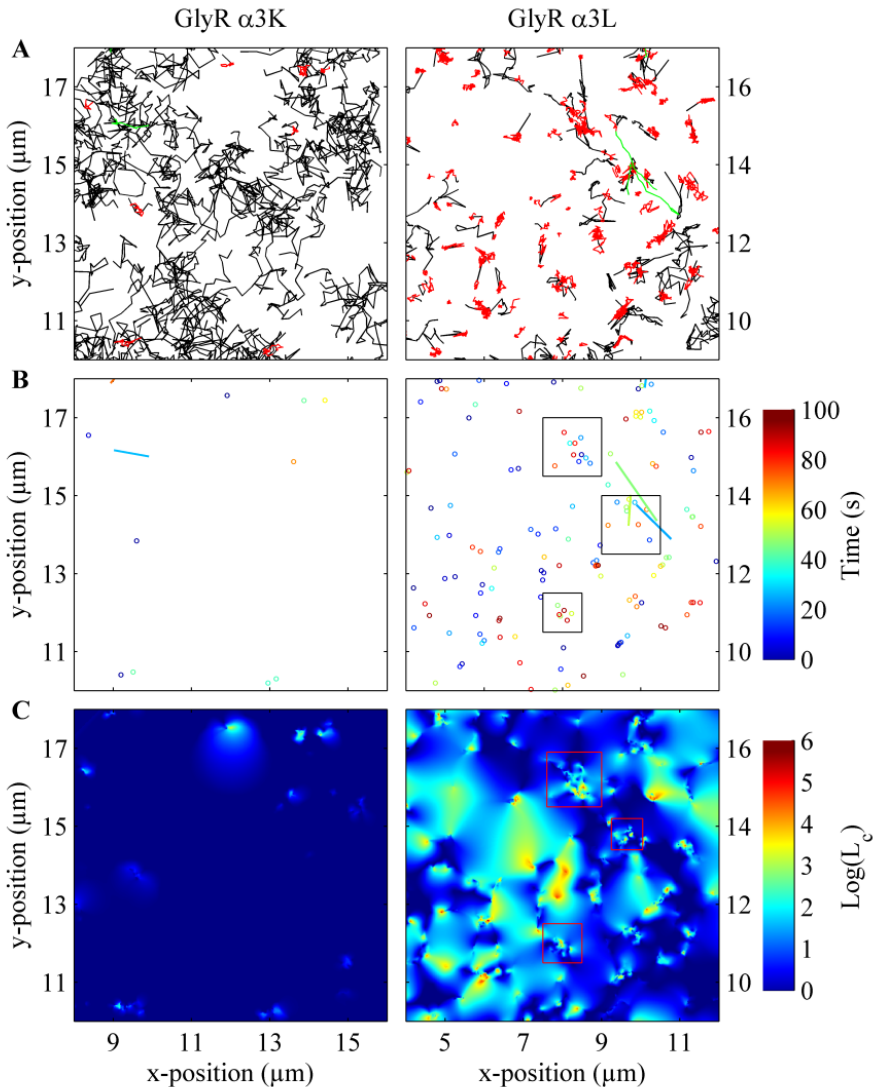


Figure 3.3: Visualization of local displacement trajectory analysis in a representative area of the bottom membrane.

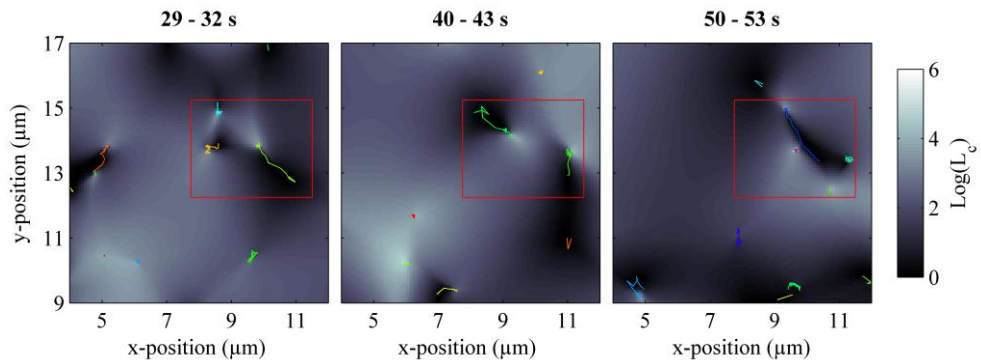
Identical color coding was used for the α 3K (117 tracks) and α 3L (223 tracks). A. Trajectory mapping indicating free diffusion (black), confined motion (red) and directed motion (green). B. Mapping of the confined motion (circles) and directed motion events (lines) in time. For confined motion the location represents the centroid of the confinement area. For directed motion, the start and end coordinates of each segment were connected by a straight line. The central frame of the occurrence was used as a time reference. Exemplary membrane areas with reoccurring events are marked by black rectangles. C. Mapping of L_c . The center coordinates of all displacements were used and the corresponding $\log(L_c)$ values were interpolated over the surface. Exemplary membrane areas showing irregular high intensity patterns of L_c are marked by red rectangles. (L_c = confinement probability level)

Table 3.1: Summary of parameter averages from local displacement analysis of $\alpha 3$ GlyR trajectories from each expression system.

For confined motion residence time, confined fraction and ρ are reported. For directed motion travel time, distance and speed are reported. (***: p -value < 0.001, NF: Not Feasible)

Motion	Parameters ^a	HEK 293	
		GlyR $\alpha 3K$	GlyR $\alpha 3L$
Confined	Prevalence (%)***	24 \pm 3	78 \pm 4
	Residence time (s)***	1.9 \pm 0.1	2.8 \pm 0.2
	Confined fraction (%)***	20 \pm 3	74 \pm 4
	ρ (μm)	0.153 \pm 0.004	0.156 \pm 0.003
Directed	Prevalence (%)***	1.1 \pm 0.2	2.7 \pm 0.3
	Travel time (s)	NF	1.00 \pm 0.04
	Distance (μm)	NF	1.7 \pm 0.1
	Speed ($\mu\text{m/s}$)	NF	1.77 \pm 0.09

^a Mean \pm standard error (HEK 293 $\alpha 3K$ $n = 7$, HEK 293 $\alpha 3L$ $n = 9$)

**Figure 3.4: Visualization of L_c variation during short time intervals.**

The color map was adapted to improve visibility of the plotted trajectories. Trajectories are individually color coded in each time interval to facilitate distinction. The red box demarcates an area showing high variations in confinement strength occurring in multiple individual trajectories spread over time. (L_c = confinement probability level)

Quantitative parameters of the anomalous diffusion events were also determined (**Table 3.1**). The average *prevalence* of confined motion was $24 \pm 3\%$ for $\alpha 3K$ and was significantly elevated for $\alpha 3L$ with $78 \pm 4\%$. Similarly, the *confined fraction* constituted $20 \pm 3\%$ and $74 \pm 4\%$ of all displacements for $\alpha 3K$ and $\alpha 3L$ respectively. For each confined motion section *residence time* and ρ were determined. The distributions of *residence time* show a range of 1 s to 6.3 s for $\alpha 3K$ and 1 s to 13.4 s for $\alpha 3L$. The distribution of *residence time* for the $\alpha 3L$ variant is right shifted compared to the $\alpha 3K$ (**Figure 3.5A**). As expected, the average *residence time* is significantly elevated for the $\alpha 3L$ variant (2.8 ± 0.1 s), compared to $\alpha 3K$ (1.9 ± 0.1 s). The distributions of ρ range from $0.050 \mu\text{m}$ to $0.290 \mu\text{m}$ and 0.046 to $0.341 \mu\text{m}$ for respectively $\alpha 3K$ and $\alpha 3L$ in HEK 293 cells. (**Figure 3.5B**). These distributions were markedly similar and also the average ρ did not show any significant difference with $0.153 \pm 0.004 \mu\text{m}$ for $\alpha 3K$ and $0.156 \pm 0.003 \mu\text{m}$ for $\alpha 3L$.

Sections with directed motion were rare compared to sections with confined motion, with a *prevalence* of only $1.1 \pm 0.2\%$ for the trajectories described by $\alpha 3K$ and $2.7 \pm 0.3\%$ for the $\alpha 3L$ trajectories. Given the low prevalence, the directed motion could only be quantified adequately for $\alpha 3L$. This was done by calculating the *travel time*, *distance* and *speed*. The process of directed motion was short lived, with an average *travel time* of 1.00 ± 0.04 s and a maximum of 2.4 s. The distribution of *distance* ranged from 0.75 to $4.8 \mu\text{m}$, with the average *distance* measuring $1.7 \pm 0.1 \mu\text{m}$ (**Figure 3.5C**). The distribution of *speed* at which the directed motion occurred ranged from $0.81 \mu\text{m/s}$ to $3.5 \mu\text{m/s}$, with an average *speed* of $1.77 \pm 0.09 \mu\text{m/s}$.

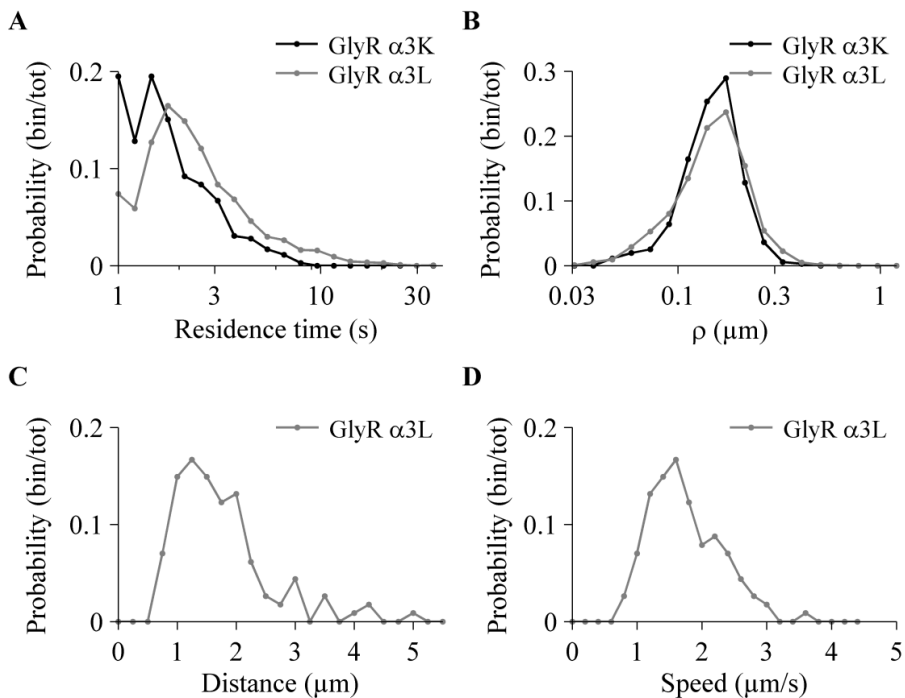


Figure 3.5: Quantitative parameters of the anomalous diffusion events.

A. The distribution (log scale) of the residence times for the confined motion sections. B. The distribution (log scale) of ρ for the confined motion sections. C. The distributions of the distance calculated for all the directed motion sections. D. The distributions of the speed calculated for all the directed motion sections. (bin = number of elements in bin, tot = total elements in distribution, ρ = radius of the confinement area)

Based on the gradients in L_c occurring in individual trajectories, the coincidence of directed and confined motion was assessed (**Figure 3.6**). Directed motion is the least prevalent form of anomalous diffusion and therefore coincidence was calculated as the percentage of trajectories with directed motion, which also contained confined motion. In the $\alpha 3L$ GlyR population displaying directed motion, $51 \pm 7\%$ also displayed confined motion. The grouped population characteristics of trajectories containing coincident directed and confined motion were further quantified. Both transitions from confined to directed (C - D) and directed to confined (D - C) motion occurred, with an equal $50 \pm 12\%$ probability. Furthermore, the transition time (tt) was determined by the time span between subsequent events. The average tt was 0.15 ± 0.06 s for C - D transitions, while for D - C transitions this was 0.3 ± 0.1 s.

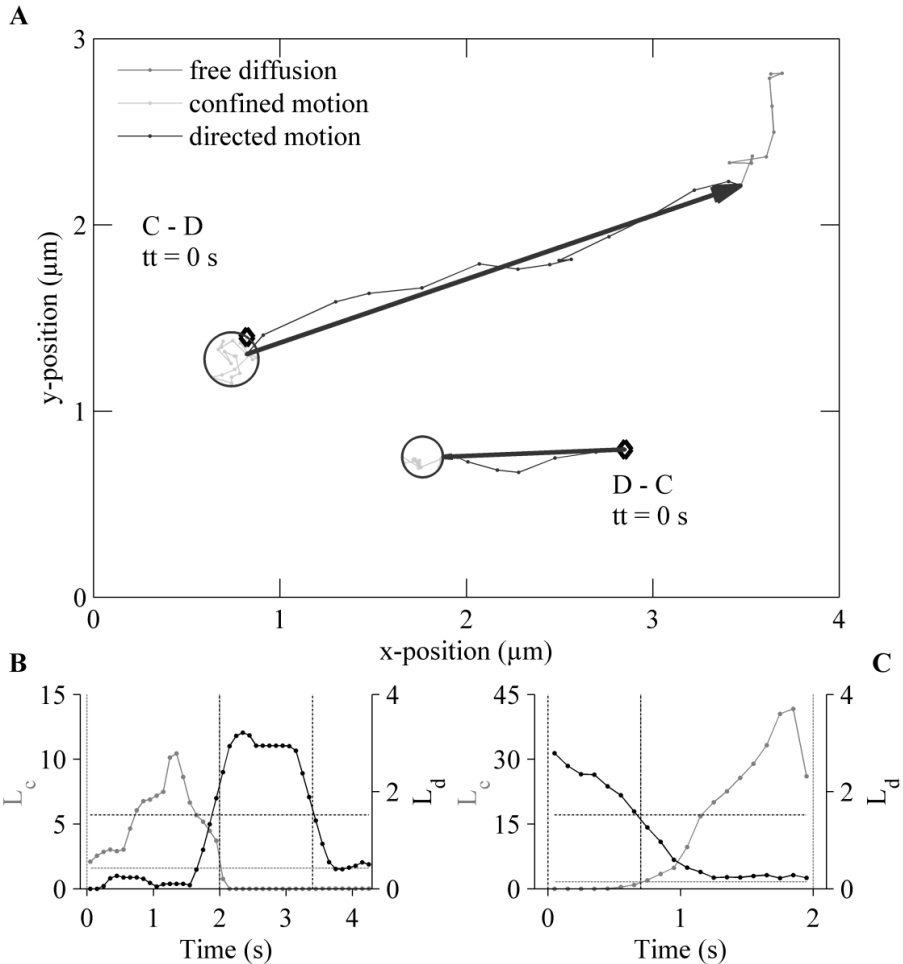


Figure 3.6: Two examples of trajectories displaying coincident confined and directed motion.

A. The GlyR $\alpha 3L$ trajectories were analyzed using the local displacement analysis and segmented into free diffusion, confined motion (circle) and directed motion (arrow). The starting point of each trajectory is indicated (\diamond). B. Plot of L_c and L_d over the course of a trajectory showing a confined to directed motion transition (C - D). The thresholds (horizontal lines) and anomalous segments (vertical lines) are indicated. In this case, $tt = 0$, notice that the first displacement exceeding the threshold of L_d is not selected because it also exceeds the L_c threshold. C. Plot of the L_c and L_d over the course of a trajectory showing a directed to confined motion transition (D - C). The thresholds (horizontal lines) and anomalous segments (vertical lines) indicate an instantaneous transition. (L_c = confinement probability level, L_d = directed motion probability level, tt = transition time)

3.5 Discussion

In this work we elaborate on the presence of anomalous diffusion in $\alpha 3$ GlyR membrane dynamics, as suggested in our earlier report [324]. Further evidence and quantification is obtained by applying advanced analysis of single particle tracking data. Moreover, the anomalous diffusion parameters reveal the nature of the differential dynamics between $\alpha 3K$ - and $\alpha 3L$ -containing GlyRs. Below, the conclusions are formed by stepwise interpretation of the subsequent analyses and placed in a physiological context.

3.5.1 Ensemble displacement analysis

In order to explore the heterogeneity of $\alpha 3$ GlyR motion, the populations of displacements were analyzed using a multi-component function [195,263]. For the $\alpha 3K$ GlyR displacements, two sub populations of displacement sizes were found, differing more than an order of magnitude. For the first and largest displacement component a linear MSD versus time relationship suggests free diffusion. The diffusion coefficient $D_e = 0.13 \pm 0.01 \mu\text{m}^2/\text{s}$ belonging to this component also corresponds well with previous fluorescence recovery after photobleaching (FRAP) measurements of GlyR $\alpha 3K$ diffusion in HEK 293 cells ($0.15 \pm 0.01 \mu\text{m}^2/\text{s}$) [324]. The FRAP measurements also reported normal diffusion with a large mobile component (0.93 ± 0.04). The order of magnitude for D_e is also in agreement with values retrieved for extrasynaptic $\alpha 1$ -containing GlyRs ($0.10 \pm 0.01 \mu\text{m}^2/\text{s}$), believed to mainly undergo free diffusion outside the synapse [150]. The smaller second displacement component did not fit to a linear model and corresponds to sub-diffusion. The fractions also indicate that the presence of the first component dominates over the second component. This confirms previous assumptions, stating that for $\alpha 3K$ GlyRs free diffusion is dominant [324]. The validity of using D_e from $\alpha 3K$ GlyRs as a measure of free diffusion for both variants can be affirmed. The 15 AA difference between the subunit variants, located in the large intracellular loop, is unlikely to influence the radius of the membrane spanning receptor segment, which determines the free diffusion coefficient [63,161,167]. On that premise, the discrepancy between the values of D_e for the two variants likely originates from an expression system-related sampling bias, introduced by applying SPT [324]. Thereby, extracting D_e from the $\alpha 3K$ GlyR was considered more reliable, given

the dominant fraction of free diffusion and the less complex nature of diffusion of the $\alpha 3K$ variant. The fact that using D_e from $\alpha 3L$ GlyRs does not change the inference of the local displacement analysis, also shows that the relative difference in D_e between the receptor variants is negligible when considering the full range of diffusion modes.

3.5.2 Local displacement analysis

Using local displacement analysis, trajectory sections deviating from free diffusion were identified. This strategy optimizes the use of single particle tracking, as anomalous diffusion events can be detected for individual particles [184,308,312]. A confinement probability based on the displacement and a directed motion probability based on the asymmetry properties were calculated [197,198]. Determining the input parameters for the analysis is an empirical process. The analysis is based on short trajectories given the use of a fluorescent dye as label. Furthermore, the approach had to accommodate the spatial and temporal properties of the anomalous processes, while limiting false positive detection.

For the detection of confined motion, the free diffusion coefficient was not estimated from the individual trajectories as done in other work [326], but from the ensemble analysis. In this way, the confined motion was not required to be transient of nature in order to be detected. The previously established presence of an immobile fraction of $\alpha 3$ GlyRs ($\alpha 3K$: 5%, $\alpha 3L$: 15%) warranted this approach, as immobile receptors were considered an extreme case of confined motion [324]. Based on the numerical proximity between the *confined motion prevalence* and the *confined fraction*, on average, confinement is dominant in trajectories containing a confinement zone. As the possibility to discriminate true confinement increases for longer observation times [197], a large sliding window was selected. We also chose to optimize detection of stable confinement zones, therefore setting a high minimally required *residence time* and allowing a less rigorous threshold of L_c to avoid false positives.

Confined motion of the GlyR has been described in most detail for the $\alpha 1$ -containing heteromeric GlyRs, as part of a diffusion and trapping model mediated by gephyrin anchoring [147,149,152]. For the heteromeric GlyR $\alpha 1$, binding to gephyrin leads to clustering of the receptor at the synapse [149,329].

However, gephyrin-independent clusters of $\alpha 1$ -, $\alpha 2$ - and $\alpha 3$ -containing homomeric GlyRs has also been established, with clustering of homomeric $\alpha 3$ -receptors being shown in both primary neurons and HEK 293 cells [152,170,330]. Here, it is demonstrated that $\alpha 3$ GlyR dynamics also involve a trapping mechanism for local $\alpha 3$ GlyR accumulation. ρ corresponds well to the sub-micrometer clustering found for $\alpha 3L$ GlyRs by super-resolution microscopy [324]. Mapping of $\alpha 3L$ GlyR diffusion reveals localized diffusion with areas showing high incidence of confined motion. Protein oligomerization, lipid raft association or clathrin-mediated stabilization are possible mechanism of GlyR trapping in HEK 293 cells, demonstrated previously for other transmembrane proteins [331-334]. With regards to biological signaling, confining receptors in specific membrane areas or in high density clusters can affect both the immediate electrophysiological response as well as the downstream signaling capacity [171,317,335,336].

Interestingly, the GlyR $\alpha 3K$ is also capable of being confined, yet the frequency and the stability of the confined state are not sufficient for outspoken local accumulation of this variant. The similar range of ρ suggests both variants are prone to the same confining interactions, yet with different efficiencies. Alternatively, $\alpha 3L$ may undergo an additional confining interaction, an argument supported by the increased number of components in the ensemble analysis. In that respect the 15 AA insert of $\alpha 3L$ can either indirectly stabilize interactions, as its absence leads to unstable folding of the large TM 3-4 intracellular domain [174]. On the other hand, the insert can also be a binding target, leading to additional confinement, similar to the gephyrin binding domain of the β -subunit [134].

The determination of directed motion was based on the asymmetry of the gyration matrix T , a measure independent of the displacement size. Thereby directed motion was initially independent of the diffusion coefficient and observation time [198]. This allowed a reduction of the sliding window size, making L_d less smooth but more sensitive to short time scale fluctuations. Considering the fast dynamics of directed motion, not dependent on Brownian motion, such a detection scheme was considered advantageous. However, the supposition of directed motion involved an elongated trajectory form [324], displaying a net displacement. As asymmetry is not exclusive to elongated

trajectories, incorporating a minimum square displacement improved detection of directed motion. A two parameter (asymmetry and minimum square displacement) detection scheme also allowed for a more efficient discrimination of directed motion from free diffusion.

The low directed motion *prevalence* could in part be attributed to the technical difficulties of tracking a fast moving particle in a heterogeneously diffusing particle population. The presence of micrometer scale saltatory motion at speeds of almost several micrometers per second is not common for transmembrane proteins. It has been reported for vesicular transport guided by motor proteins, which has been established in transmembrane receptor trafficking [77,80,337]. Vesicular transport by motor proteins is also a means of antero- and retrograde transport in neurons and is essential for GlyR trafficking [137,141,142,338,339]. With the TIRF set up it is only possible to monitor vesicular transport near and parallel to the cell membrane, biasing directed motion *prevalence* [191,340]. Regardless of the low prevalence, active (re-)distribution in the membrane is likely to be requisite for α 3L GlyRs given their stationary nature. The contrasting mobile nature of α 3K GlyRs, might explain the decreased occurrence or absence of directed motion dynamics.

The presence of confined and directed motion being explained by two independent processes is possible, but unlikely in this case. Mapping of the trajectories indicated steep gradients in confinement probability, resembling a transfer of motion type. Therefore the coincidence of directed and confined motion in single trajectories was investigated. Over half of the trajectories exhibiting directed motion also displayed confinement, confirming that a single receptor can be subjected to both types of anomalous diffusion. There was no particular order in the occurrence of directed and confined motion. However, analysis of the time span of the transitions indicated that, under the given temporal resolution, the different motion types occurred in almost immediate succession. The occurrence of different motion types in a transmembrane receptor population has been reported before [70,295]. The presence of coupled confined and directed motion, more specifically resembles clathrin-mediated receptor stabilization and dynamin-dependent endocytosis coupled to vesicular receptor trafficking/recycling as described for transferrin, epidermal growth factor receptors and AMPA receptors [333,341-345]. In fact, both α 3 RNA splice

variants harbor at the N-terminus of the TM 3-4 cytosolic loop a di-leucine motif involved in dynamin (AP-2)-dependent receptor internalization [145,167,346]. Furthermore cargo dependence of dynamin-regulated clathrin-coated pit maturation has been demonstrated [347]. In that respect, the diffuse $\alpha 3K$ GlyRs may, in contrast to the accumulating $\alpha 3L$ GlyRs, not be capable of producing sufficient cargo for endocytosis. Active removal and recycling of ligand-gated receptors from the membrane is an important mean to physiologically modulate their function [348]. Distinct pathways of transmembrane receptor endocytosis have even been shown to differentially impact the signaling cascade [349,350].

To summarize, advanced single particle tracking analysis has revealed new information on the membrane dynamics of homomeric $\alpha 3$ -containing GlyRs. The heterogeneous $\alpha 3$ GlyR motion pattern was quantified and interpreted using a combination of ensemble and local SPT analysis. The $\alpha 3$ GlyRs show exchange between states of local confinement and normal diffusion. RNA splicing exerts a major influence on the balance between these states and is associated with directed motion in the case of $\alpha 3L$ GlyRs. The speed of the directed motion matches that of saltatory vesicular motion and frequently occurs coupled to confined motion. These characteristic motion features strongly suggests that molecular interaction between a cellular component and the exon 8A-encoded sequence of the RNA splicing-dependent L-insert (TEFALEKFYRFSDT) is responsible for directed motion and anomalous diffusion of this GlyR $\alpha 3$ RNA splice variant. Differential desensitization and synaptic clustering of these receptor RNA variants implies that their biophysical membrane behavior strongly impacts GlyR $\alpha 3$ signaling. Consequently these results are also relevant to GlyR $\alpha 3$ pathophysiology in neurological disorders [175], e.g. in temporal lobe epilepsy where GlyR $\alpha 3$ RNA splicing is changed in patients with a severe disease course [166,170].

3.6 Supplementary material

3.6.1 Multi-component fit of the cumulative square displacement distribution for $\alpha 3K$ GlyRs

For each individual experiment the cumulative distribution of square displacements was fit using an exponential function (Eq. 3.1). A two-component function gave a superior fit of the data compared to a single-component function (**Figure 3.7**). This was anticipated given the previously suggested presence of anomalous diffusion.

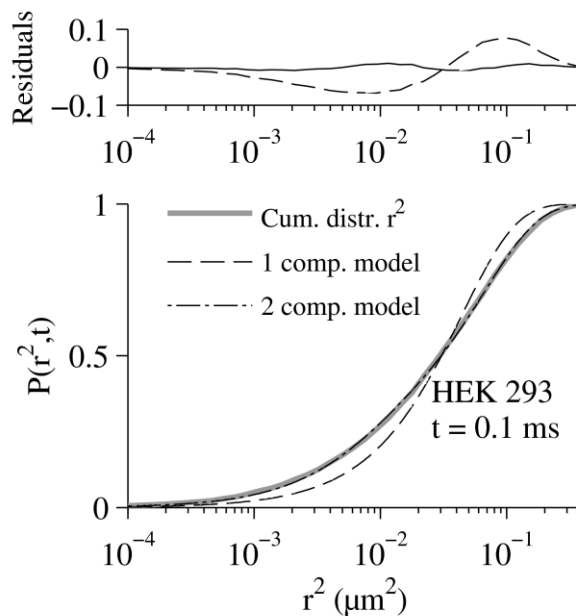


Figure 3.7: Fitting of the cumulative distribution of square displacements.

Representative data set from $\alpha 3K$ GlyR diffusion in HEK 293 cells. The distributions for the first order time lag are shown and a two-component fit is clearly superior to a single-component fit. (Cum. = cumulative, comp. = component)

3.6.2 Determination of thresholds for anomalous diffusion analysis

Simulations of free diffusion were done by generating random walk trajectories in Matlab. Trajectories were built by simulating particles with variable jump sizes at fixed time points, implying no interaction between particles. In each simulation 2000 trajectories were simulated containing 101 points (100 displacements). The displacements in x- and y-direction were generated independently, according to $\sqrt{(2Dt_s)}u$, where D is the diffusion coefficient, t_s is the time step and u is a standard normally distributed random number. The selected D was $0.135 \mu\text{m}^2/\text{s}$ and t_s was 0.1 s. Ten independent simulations were run. For each individual simulation, the local displacement analysis was applied exactly as described in the materials and methods. False positives displacements for directed and confined motion were determined and their percentage of the total number of displacements calculated. For each data set the values of L_c and L_d corresponding to 0.1% false positives were determined and the average was applied as threshold (**Figure 3.8**). The resulting thresholds were 1.60 ± 0.02 for L_c and 1.52 ± 0.02 for L_d .

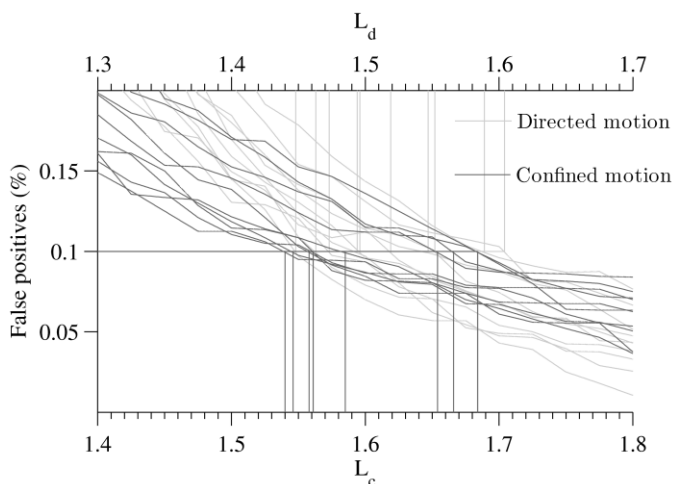


Figure 3.8: Determination of thresholds for confined and directed motion levels, respectively L_c and L_d .

Ten independent data sets of simulated random diffusion were analyzed for false positives. The threshold was selected based on generating $\leq 0.1\%$ false positives.

3.6.3 Ensemble displacement analysis for the α 3L GlyR

In order to accurately fit the cumulative distribution of square displacements, the exponential fitting was expanded to a three-component model:

$$P(r^2, t) = 1 - \sum_{i=1}^3 A_i \exp\left(-\frac{r^2}{r_i^2}\right) \quad \sum_{i=1}^3 A_i = 1 \quad (3.9)$$

The resulting MSDs yielded one large (r_1^2) and two small components (r_2^2, r_3^2) as shown below. The former was fit with a free diffusion model (Eq. 3.2), which yielded $D_e = 0.09 \pm 0.01 \mu\text{m}^2/\text{s}$ (**Figure 3.9A**). The first small component was fit with an anomalous diffusion model (Eq. 3.3), yielding $\alpha_e = 0.71 \pm 0.08$ and $D_e' = (7.6 \pm 0.7) \times 10^{-3} \mu\text{m}^2/\text{s}^\alpha$ (**Figure 3.9B**). The second small component showed little increase of MSD in time and was very close to the localization precession ($4\sigma^2$). A linear, free diffusion, model was applied for an estimate of the diffusion coefficient, yielding $D_e = (8 \pm 0.5) \times 10^{-4} \mu\text{m}^2/\text{s}$ (**Figure 3.9B**). For the α 3L variant the small components represent the largest fractions in the distribution (**Figure 3.9C**).

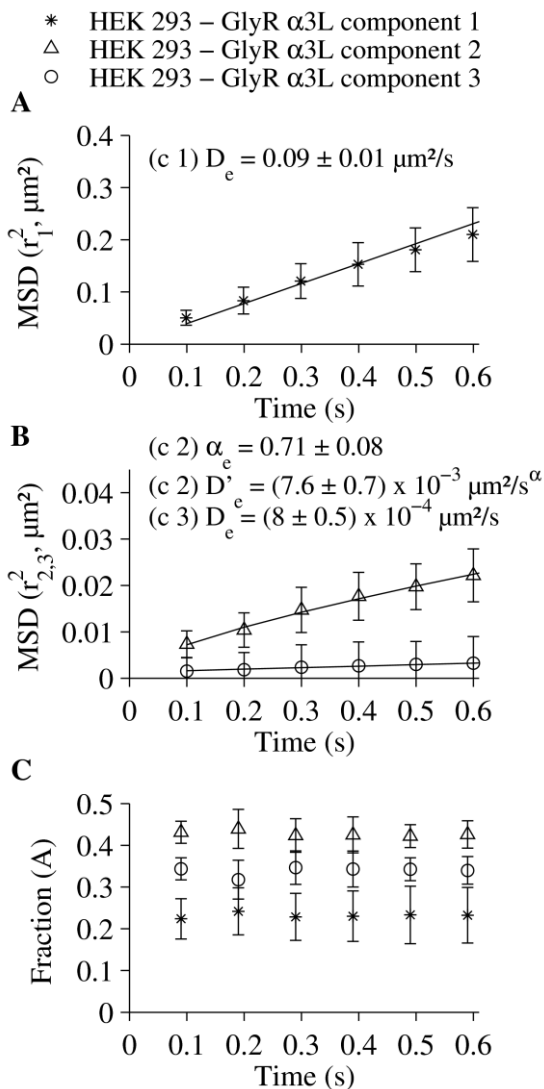


Figure 3.9: Ensemble displacement analysis of GlyR α 3L diffusion in HEK 293.

A three-component function was used, yielding three MSD components (c 1, c 2, c 3) with their respective fractions (error bars represent standard deviation). A. The MSD of the first component over consecutive time lags. A free diffusion model (Eq. 3.2, D_e indicated with 95% confidence interval). B. The MSD of the second and third component over consecutive time lags. For the second component an anomalous diffusion model was applied, (Eq. 3.3, α_e and D_e' indicated with 95% confidence interval). The third component showed nearly no increase in MSD over time. A linear, free diffusion model, was used to provide an estimate of the diffusion coefficient (D_e^e , indicated with 95% confidence interval). C. The relative fractions of each component in the ensemble population.

3.6.4 Local displacement analysis parameters using D_e derived from GlyR $\alpha 3L$ ensemble analysis.

The impact of D_e on the local displacement analysis was evaluated. The output parameters were calculated using the $\alpha 3K$ D_e ($0.13 \mu\text{m}^2/\text{s}$) and the $\alpha 3L$ D_e from the first component ($0.09 \mu\text{m}^2/\text{s}$). For most parameters no significant difference is detected. The only exception is ρ which is significantly decreased when applying the latter D_e . This is not unexpected, as L_c is directly dependent on the value of D_e and ρ is a direct measure of the trajectory extent evaluated by L_c . However the shift in ρ is not of an order that bears any significance to the biological inference.

Table 3.2: Summary of parameter averages from local displacement analysis of $\alpha 3L$ GlyR trajectories using different measures for free diffusion.

*For confined motion the residence time, the confined fraction and the radius are reported. For directed motion the residence time, the distance and the speed are reported. (***: p-value < 0.001)*

		HEK 293 - GlyR $\alpha 3L$	
Motion	Parameters ^a	$D_e = 0.13 \mu\text{m}^2/\text{s}$	$D_e = 0.09 \mu\text{m}^2/\text{s}$
Confined	Prevalence (%)	78 ± 4	70 ± 4
	Residence time (s)	2.8 ± 0.2	2.7 ± 0.1
	Confined fraction (%)	74 ± 4	66 ± 4
	ρ (μm)***	0.156 ± 0.003	0.133 ± 0.002
Directed	Prevalence (%)	2.7 ± 0.3	3.1 ± 0.4
	Travel time (s)	1.00 ± 0.04	1.02 ± 0.03
	Distance (μm)	1.7 ± 0.1	1.7 ± 0.1
	Speed ($\mu\text{m}/\text{s}$)	1.77 ± 0.09	1.68 ± 0.09

^a Mean \pm standard error (HEK 293 $\alpha 3L$ $n = 9$)

4 Membrane distribution of the glycine receptor $\alpha 3$ studied by optical super-resolution microscopy

Kristof Notelaers, Susana Rocha, Rik Paesen, Nina Swinnen, Jeroen Vangindertael, Jochen C. Meier, Jean-Michel Rigo, Marcel Ameloot, Johan Hofkens

Journal:

Histochemistry and cell biology 2014

Epub date: 20/02/2014

doi: 10.1007/s00418-014-1197-y

4.1 Abstract

In this study the effect of glycine receptor (GlyR) $\alpha 3$ alternative RNA splicing on the distribution of receptors in the membrane of HEK 293 cells is investigated using optical super-resolution microscopy. Direct stochastic optical reconstruction microscopy (dSTORM) is used to image both $\alpha 3K$ and $\alpha 3L$ splice variants individually and together using single- and dual-color imaging. Pair correlation analysis is used to extract quantitative measures from the resulting images. Autocorrelation analysis of the individually expressed variants reveals clustering of both variants, yet with differing properties. The cluster size is elevated for $\alpha 3L$ compared to $\alpha 3K$ (resp. mean radius 92 ± 4 nm and 56 ± 3 nm), yet an even bigger difference is found in the cluster density (resp. $9870 \pm 1433 \mu\text{m}^{-2}$ and $1747 \pm 200 \mu\text{m}^{-2}$). Furthermore cross-correlation analysis revealed that upon co-expression, clusters colocalize on the same spatial scales as for individually expressed receptors (mean co-cluster radius 94 ± 6 nm). These results demonstrate that RNA splicing determines GlyR $\alpha 3$ membrane distribution, which has consequences for neuronal GlyR physiology and function.

Key words

super-resolution microscopy, direct stochastic optical reconstruction microscopy, pair correlation analysis, glycine receptor, alpha3 subunit, RNA splicing,

4.2 Introduction

Imaging of cellular proteins by means of fluorescence microscopy has become a routine approach in biology, as it allows specific *in situ* labeling with strong signal to noise ratio. Nevertheless, the spatial resolution is limited to ca. 200 to 250 nm, the optical diffraction limit. This results in an uncertainty when determining the physical dimensions of nanoscale components in cell biology, such as proteins and nucleic acids. In recent years various super-resolution microscopic modalities have been developed to circumvent the diffraction limit: (fluorescence) photoactivation localization microscopy ((f)PALM) [208,351], stimulated emission depletion microscopy [352], structured illumination microscopy [353,354], (direct) stochastic optical reconstruction microscopy ((d)STORM) [210,211,355], and super-resolution optical fluctuation imaging [356,357], among others. For a more extensive review see Cremer *et al.* [358].

Both (f)PALM and (d)STORM use the stochastic activation of individual fluorophores and the precise localization of their position to render images with a higher resolution. With the design of brighter fluorescent probes and more sensitive detection devices, the position of single emitters can be calculated with nanometer accuracy by fitting their diffraction-limited point-spread function (PSF) [214,216,312]. However, in order to do so, the individual fluorescent molecules need to be well isolated from each other (densities ranging between 10 and 50 molecules/ μm^2). Through the use of photoswitching between two distinct fluorescence emissive states it is possible to achieve the necessary sparseness in densely labeled specimens [359]. Other approaches to obtain optical isolation take advantage of other spectral characteristics, such as fluorescence life times [360] or time invariant spectral differences [361-363]. In fact, optical isolation of closely adjacent point emitters can be achieved by exploring different excitation/emission properties of dye molecules [358].

In the case of dSTORM, applied in this work, photoswitching is performed by stabilizing an intermediate 'dark state' of a commercially available organic dye [215,217,364,365]. It is important to indicate that the 'dark state' does not necessarily imply a state with no photon emission, but rather a state where no emission is observed using a specific filter configuration in the detection. From this 'dark state' a small subset of dye molecules is stochastically allowed to go

back to the ground state from where they are excited. Repeating this process for multiple cycles, with each cycle generating a unique subset of activated fluorophores, enables the reconstruction of the image by plotting the calculated position of each molecule. The extension of the method to more than one color can provide information regarding the colocalization of molecules [221-223]. In fact, multicolor high resolution microscopy can resolve distances of 15 to 200 nm, bridging the gap between Förster resonance energy transfer and conventional diffraction limited fluorescence microscopy [221,223,364,366-370].

Recent studies have revealed heterogeneity in the spatial distribution of the lipid molecules composing the plasma membrane [92,236]. Such heterogeneities are often referred to as lipid rafts [92,371]. Some of the plasma membrane proteins are also not uniformly distributed, but appear organized in clusters commonly referred to as microdomains. It has been proposed that microdomains containing receptor molecules can serve as a platform for signaling cascades and can also play a role in endocytosis processes [50,372]. Microdomain signaling is an essential concept in neurotransmission, since sub-diffraction clustering of neurotransmitter receptors is required for efficient neuronal communication [228,257]. Hence, accurate quantification of neurotransmitter receptor membrane distribution is instrumental in understanding their signaling properties. Optical super-resolution microscopy and its concomitant analysis methods provide the tools to gain this understanding and have been successfully applied to the study of several membrane proteins, namely tetherin [222], arrestin [373], ryanodine receptors and caveolin [374], Her2/neu receptors [368], G-protein coupled receptors [375], P-Glycoproteins [376], SNAP receptors [366] and cytokine receptors [377]. In this work we have applied dSTORM to analyse the distribution of the glycine receptor (GlyR) in the plasma membrane.

The GlyR is a pentameric cys-loop ligand-gated ion channel (LGIC) permeable to chloride, inciting developmentally regulated neuronal hyperpolarisation upon activation [122,138]. For the GlyR $\alpha 3$, post-transcriptional processing has an important impact on membrane distribution and signaling [161]. RNA splicing of the *GLRA3* gene transcript generates two $\alpha 3$ -subunit variants, identified as the short $\alpha 3K$ and long $\alpha 3L$. The $\alpha 3L$ subunit contains an extra 15 amino acid (AA) insert in the large intracellular loop between transmembrane segments 3 and 4

(TM 3-4). With regard to signaling, the presence of the insert has an influence on channel gating and receptor desensitization [167,174]. Membrane distribution is also significantly influenced, as the insert regulates synaptic localization and membrane aggregation status [170]. Regarding physiology, the GlyR $\alpha 3$ is involved in pain sensitization, processing of visual and acoustic stimuli and epilepsy [162-164,168,175]. Imaging the higher order organization in the membrane distribution of the GlyR $\alpha 3$ will thereby advance our understanding of these signaling cascades.

In this work, pair correlation analysis is applied to quantify and compare the distribution of the GlyR $\alpha 3$ splice variants in the membrane of HEK 293 cells imaged by dSTORM. Pair correlation analysis is a well established method that evaluates receptor density fluctuations, using the autocorrelation of receptor localizations in order to identify clusters [244]. The capacity to compensate for repeated localizations of the same molecule, a known artifact of photoswitching based microscopy, makes this method preferable for analyzing dSTORM images [246]. Regarding the GlyR $\alpha 3$ membrane distribution, clustering is found for both splice variants. However, the clusters show marked differences in size and receptor content. Furthermore, the co-expression distribution properties were also examined by analyzing dual-color super-resolution images using pair correlation analysis. In this case, the cross-correlation was used to study the relative spatial organization of the two splice variants. Consequently, the presence of colocalized clustering of both splice variants is established and the spatial scale is determined.

4.3 Material & methods

4.3.1 Cell culture

Human embryonic kidney 293 cells (HEK 293, kindly provided by Dr. R. Koninckx, Jessa Hospital, Hasselt, Belgium) were maintained at 37°C in a humidified incubator at 5% CO₂ in Dulbecco's modified eagle's medium (Ref. 41966, Gibco, Paisley, UK) supplemented with 10% fetal calf serum (FCS, Biochrom AG, Berlin, Germany) and a penicillin (100 IU/ml)-streptomycin (100 µg/ml) mixture (Invitrogen, Carlsbad, CA, USA). The cells used for microscopic observation were plated two days before the experiment in 8-well Lab-Tek™ II chambered coverglass (Nalge Nunc International, Penfield, NY, USA), coated with 10 µg/ml fibronectin. Seeding was done at a density of 20,000 cells per well in transfection medium. This is Dulbecco's modified eagle's medium (Ref. 41965, Gibco) supplemented with 10% FCS.

4.3.2 Transfection

After overnight incubation, the cells were transfected using calcium phosphate co-precipitation with plasmids encoding for the haemagglutinin (HA) or FLAG-tagged splice variants α 3K and α 3L of the mouse GlyR α 3. The epitope-tags were inserted into the extracellular N-terminal domain between the second and third amino acid of the mature, signal-peptide cleaved receptor protein [170]. The plasmids were diluted in 250 mM CaCl₂ buffer at a concentration of 20 ng/µl and an equal amount of HEPES buffered saline solution (HBS, pH 7.05) was added dropwise. After 15 minutes of incubation, this mixture was added to the culture medium of the cells at a final concentration of 0.21 µg/cm² DNA. After 6 hours, the transfection medium was replaced with transfection medium supplemented with 200 nM strychnine. All measurements occurred within 24 to 36 hours after transfection.

4.3.3 Labeling

Labeling was done with an HA-tag mouse monoclonal antibody conjugated with Alexa Fluor® 647 and/or rabbit DYKDDDDK-tag (anti-FLAG) antibody conjugated with Alexa Fluor® 488 (Cell Signaling technologies, Danvers, MA, USA) according to the manufacturer's instructions. Selection of the epitope-tag (HA or FLAG) and subsequent labeling strategy, did not influence the clustering

properties of the receptors. Cells were fixed with 4% paraformaldehyde (PFA) for 15 minutes at room temperature. After fixation cells were rinsed with phosphate-buffered saline (PBS) and before imaging, the blinking buffer was applied. The latter consisted of TRIS buffer (pH 8) supplemented with 100 mM cysteamine [210].

4.3.4 Direct stochastic optical reconstruction microscopy

dSTORM was carried out at room temperature using an inverted epi-fluorescence microscope (Olympus IX83 frame S1F-3, Olympus Optical, Tokyo, Japan) equipped with a PlanApo TIRF 60x oil objective (NA 1.45; Olympus Optical). The sample was simultaneously irradiated by a 100 mW 405 nm (Cube Coherent Inc, Santa Clara, CA, USA), 200 mW 488nm (Coherent) and 100 mW 642 nm (Excelsior 642, Spectra-Physics, Irvine, CA, USA) diode laser. This light was directed by the DC (z488/561/638rdc, Chroma Inc., Bellow Falls, VT, USA) towards the objective in off-axis mode to obtain total internal reflection fluorescence (TIRF). Excitation light was removed using HQ655LP and HQ700/75 (Chroma) emission filters for the detection of Alexa647 and HQ505LP and HQ525/50m-2P (Chroma) for the emission of the Alexa488. For dual color imaging experiments, the emission was split in 2 channels using a 650dclp dichroic (Chroma). For image registration of the two channels, fluorescence images of beads (Molecular Probes, Invitrogen) were acquired. Image registration was performed as described previously [222,370], with a precision of 15 nm. The images were recorded at 20 Hz using an EM-CCD camera (ImageEM, Hamamatsu Photonics, Hamamatsu, Japan) with 50 ms integration time, an acquisition field of 512×512 pixels and an image pixel size of 107 nm. The peak position and the localization precision were determined for each individual emitter by Gaussian fitting analysis [189,312]. For each recording the average localization precision σ_{xy} of all emitters was determined by a skewed Gaussian fit. The mean (\pm standard error) localization precision $\langle \sigma_{xy} \rangle$ of all recordings was 17.6 ± 0.8 nm. A radius of $2.5 \times \sigma_{xy}$ was used to consolidate emitters present over multiple successive frames. The super-resolution images shown in this work were made by mapping peak locations to a pixel map with pixel size ~ 18 nm, corresponding to the localization precision. All image processing was done using home-built MATLAB® (R2010b, The Mathworks, Natick, MA, USA) routines.

4.3.5 Pair correlation analysis

Pair correlation analysis was used to analyze the high density distribution of the accumulated single molecule peaks. Membrane areas with uniform receptor distribution, measuring at least 5 μm by 5 μm , were selected allowing accurate determination of correlation. Both auto- and cross-correlation analysis of the receptor localizations were done as described in the following reference, where a detailed protocol and application of the method are illustrated [245]. The 2D autocorrelation $[g(u,v)]$, normalized to 1 for large radius, was calculated using Fast Fourier Transform (FFT), transformed to polar coordinates and binned by radius. Nonlinear functions were used for fitting of the calculated autocorrelation $(g(r), r > 0)$. The first function describes the autocorrelation of molecules distributed randomly across a 2D surface, with the sole correlation arising from the detection of multiple peaks from a single molecule. This is known as overcounting and can be modeled by a 2D Gaussian function $g(r)^{oc}$ as described in [244]:

$$g(r)^{peaks} = g(r)^{oc} + 1 = \frac{1}{4\pi\sigma_s^2\rho^{protein}} \exp\left(-\frac{r^2}{4\sigma_s^2}\right) + 1 \quad (4.1)$$

According to this function $\rho^{protein}$ is the overall protein density, constrained by the peak density of the selected membrane area $\rho^{protein} \leq \rho^{peaks}$. If $\rho^{protein} < \rho^{peaks}$ overcounting is present, with the percentage of data sets containing overcounting defining the *prevalence*. In the case of overcounting, the average repeated localization rate can be determined by $\rho^{peaks}/\rho^{protein}$. The parameter σ_s represents the single molecule localization uncertainty derived from repeated localizations, and effectively quantifies the super-resolution PSF (srPSF). These estimates are valid when overcounting arises from a random, Poisson distributed process. This is the case for overcounting arising both from stochastic blinking of fluorophores during dSTORM and the presence of multiple fluorophores per labeled protein [246].

If the proteins are non-randomly distributed over a 2D surface, the autocorrelation of the corresponding peaks will exceed 1 over the spatial scale of clustering. If this occurs via organization into randomly distributed domains with no specific shape, the autocorrelation can be analyzed by an exponential

approximation convoluted with the correlation function of the srPSF; if both overcounting and clustering are present, the following function can be applied to the autocorrelation:

$$\begin{aligned}
 g(r)^{peaks} &= g(r)^{oc} + g(r)^{cluster} \\
 &= \frac{1}{4\pi\sigma_s^2\rho^{protein}} \exp\left(-\frac{r^2}{4\sigma_s^2}\right) + \left(A \exp\left(-\frac{r}{\xi}\right) + 1\right) \quad (4.2) \\
 &* g(r)^{srPSF}
 \end{aligned}$$

This approach has been empirically determined and successfully applied to the research of heterogenic membrane protein distribution by Sengupta *et al.* [247]. The pre-factor A , is proportional to the density of proteins in the cluster and the correlation length ξ , proportional to the cluster size. The correlation function related to the localization uncertainty introduced by the 2D srPSF is as follows:

$$g(r)^{srSPF} = \frac{1}{4\pi\sigma_s^2} \exp\left(-\frac{r^2}{4\sigma_s^2}\right) \quad (4.3)$$

The fit parameters extracted from the cluster approximation (Eq. 4.2) allow for the determination of the average cluster occupancy, N :

$$N \approx 2A\pi\xi^2\rho^{protein} \quad (4.4)$$

and the ratio of the average density of proteins in clusters ($\rho^{cluster}$) to the overall protein density ($\rho^{protein}$), termed the density increment ψ :

$$\psi = \frac{\rho^{cluster}}{\rho^{protein}} = \frac{N}{\pi\xi^2\rho^{protein}} \approx 2A \quad (4.5)$$

These parameters were determined for multiple distinct bottom membrane areas ($\alpha 3K$, $n = 59$; $\alpha 3L$, $n = 55$).

Cross-correlation analysis was applied to dual-color super-resolution images of the α 3K and α 3L GlyR splice variants co-expressed in the membrane. Briefly, the 2D cross-correlation between the peaks in both channels was calculated using FFT, transformed to polar coordinates and averaged by radius using MATLAB. In order to assess the spatial scales of cross-correlation, a convoluted exponential function was fit to the decay phase of the cross-correlation:

$$c(r)^{peaks} = \left(A \exp\left(-\frac{r}{\xi^c}\right) + 1 \right) * c(r)^{srPSF} \quad (4.6)$$

In this equation, $c(r)^{srPSF}$ represents the cross-correlation of the srPSFs from the two individual channels. This results in a function similar to equation 4.3, where σ_s^2 is substituted by the sum of squares of the individual PSF sizes. These parameters were kept fixed at the respective σ_{xy}^2 of the peaks in each channel. The cross-correlation length, ξ^c , is proportional to the colocalization distance of the probes. This parameter was determined for multiple distinct areas of the bottom membrane measuring ($n = 33$).

4.4 Results

In order to better understand the effect of RNA splicing on GlyR $\alpha 3$ membrane distribution, optical super-resolution microscopy was applied. First micrographs are shown conveying a qualitative impression of GlyR $\alpha 3$ distribution in the membrane. This is followed by a representation of the quantification of the super-resolution images using pair correlation analysis. This autocorrelation-based analysis is used to provide quantitative measures of the distribution patterns. Furthermore dual-color super-resolution images were made to assess colocalization of the splice variants when co-expressed. This assessment was made by applying the cross-correlation feature also inherent to pair correlation analysis.

4.4.1 GlyR $\alpha 3$ RNA splice variants display differential organization in the membrane

Using TIRF microscopy, the labeled $\alpha 3$ GlyRs in the bottom layer of the cell membrane were imaged (**Figure 4.1**). The morphology of the cells expressing the $\alpha 3K$ variant, could be identified based on the fluorescence signal. Both the cell body and the small hair like filopodia around the membrane periphery, were shown to contain diffusely distributed receptors. Due to the overlapping PSFs of the individual emitters, little detail can be discerned from the TIRF image of the bottom membrane. In the super-resolution image, a ubiquitous receptor distribution is shown as expected. However, a few sites of low-level receptor aggregation appear to be present. The contrast in receptor distribution between the splice variants $\alpha 3K$ and $\alpha 3L$ is already apparent from the TIRF image. The $\alpha 3L$ GlyRs are not distributed diffusely over the cell, but appear as bright spots in the bottom membrane of the cell body. The size of the spots is in the nanometer range, yet an accurate description of the clusters is hard to produce from the diffraction-limited image. In the super-resolution image, the spots appear as well defined receptor clusters and the majority of the receptor population resides inside clusters.

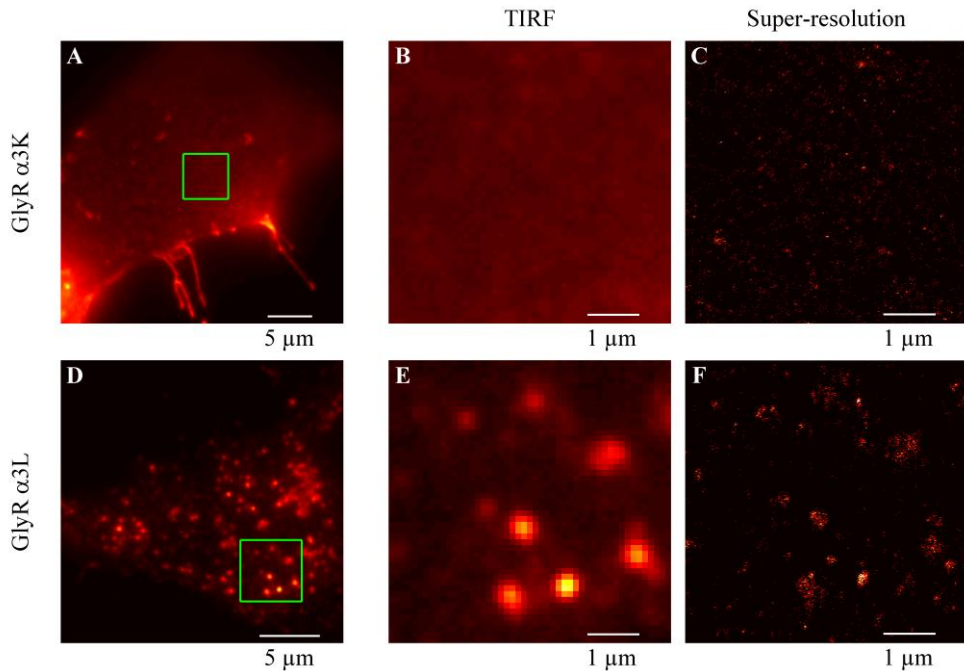


Figure 4.1: Micrographs showing the differential distribution of the HA-GlyR α 3K (A-C) and HA-GlyR α 3L (D-F) in the bottom membrane of HEK 293 cells (colormap hot).

The receptors were labeled with an anti-HA antibody conjugated with Alexa Fluor 647 and images were acquired using TIRF-microscopy (A,D). For each variant, a section of the bottom membrane image, typically used for analysis, was selected and magnified (B,E). Super-resolution images, obtained by applying dSTORM, allowed for an accurate visualization of the sub-diffraction organization of bottom membrane receptors (C,F).

4.4.2 Analysis of GlyR α 3 membrane distribution using pair correlation analysis

In order to access the sub-diffraction information, pair correlation analysis was applied (**Figure 4.2**). This method compares the probability of finding a receptor at a certain distance (r) of another receptor to that same probability expected from random distribution of receptors. Therefore, values of $g(r) > 1$, as found for both GlyR α 3 splice variants, indicate non-random distribution of receptors in the bottom membrane. This can occur through the clustering properties of the receptor or by repeated localization of identical molecules spaced in time. In the latter case, the autocorrelation should fit to a Gaussian function specifying the localization error and protein density (Eq. 4.1). However, in case of both α 3 splice variants the Gaussian model does not accurately describe the

autocorrelation, indicating that the detected correlation is not an artifact of the imaging modality. Instead, a long-range decay is present in the autocorrelation, approximated by a function defining the clusters (Eq. 4.2). The autocorrelation fit functions of $\alpha 3K$ and $\alpha 3L$ GlyRs differ in both length and amplitude, with the latter splice variant exhibiting a longer correlation range and elevated amplitude. Repeated localization of identical emitters was compensated in data sets of both splice variants, with more average repeated localizations for the $\alpha 3L$ variant (**Table 4.1**). In the instances with repeated localizations the average localization error was 19.0 ± 0.8 nm for the $\alpha 3K$ and 21.2 ± 0.7 nm for $\alpha 3L$ (mean \pm standard error).

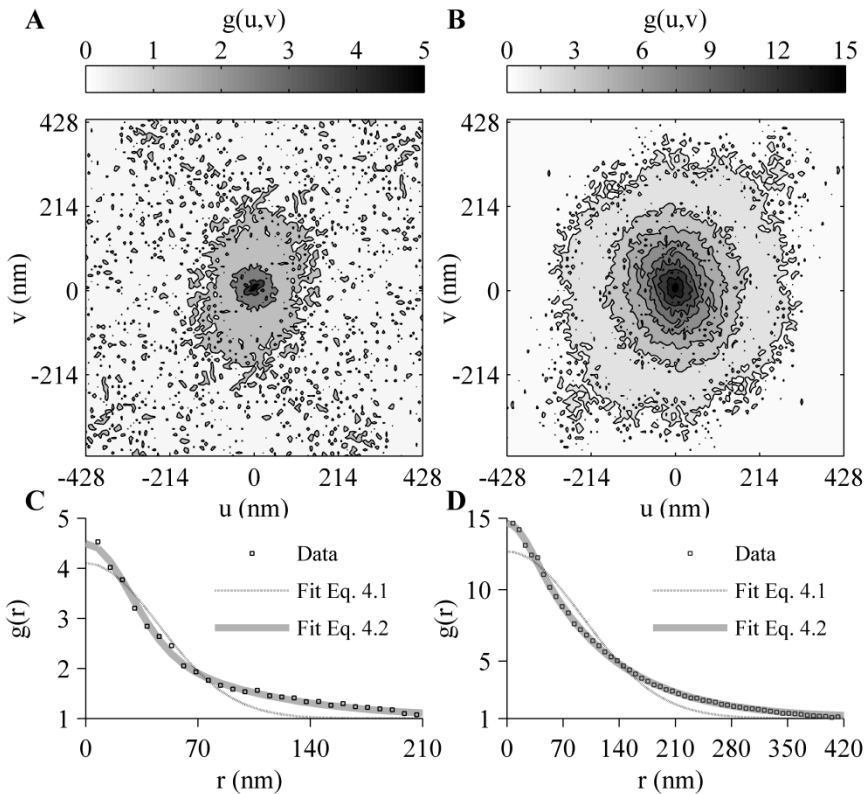


Figure 4.2: Pair correlation analysis of the GlyR $\alpha 3K$ (A,C) and GlyR $\alpha 3L$ (B,D) distribution in the bottom membrane.

The analysis is based on determining the 2D autocorrelation $g(u,v)$ of the receptor localizations obtained with dSTORM (A,B). The 2D autocorrelation is transformed (see M&M) and fitted using models for random (Eq. 4.1) and clustered (Eq. 4.2) distributions of receptors (C,D). For both variants a clustering model is better suited to describe the autocorrelation. Based on the more pronounced correlation ($g(r) \gg 1$) for $\alpha 3L$ (B,D) compared to $\alpha 3K$ (A,C), the $\alpha 3L$ GlyR density increase caused by clustering is more severe and occurs over longer spatial scales.

Table 4.1: Summary of parameters extracted from fitting the autocorrelation according to equation 4.2.

Overcounting refers to parameters extracted from $g(r)^{oc}$, related to repeated localization of identical emitters. Clustering refers to parameters extracted from $g(r)^{cluster}$, describing the spatial increment of receptor density by clustering.

Origin	Parameters	HEK 293	
		GlyR α 3K	GlyR α 3L
Overcounting	Prevalence	51 %	73 %
	$\rho^{peaks}/\rho^{protein}$	3.3 ± 0.5^a	8 ± 1.2
	σ_s^2	19.0 ± 0.8 nm	21.2 ± 0.7 nm
Clustering	ξ	56 ± 3 nm	92 ± 4 nm
	N	14 ± 2	220 ± 27
	$\rho^{cluster}$ [$N/(\xi^2\pi)$]	1747 ± 200 μm^{-2}	9870 ± 1433 μm^{-2}
	ψ	8 ± 1	34 ± 3

a Values are reported as mean \pm standard error

4.4.3 GlyR α 3 splice variant clustering properties

Pair autocorrelation analysis reveals information on both the cluster size and the cluster occupation. For all quantitative measures derived from the analysis the mean \pm standard error is given (**Table 4.1**). For the primary parameters the histogram is given (**Figure 4.3**) and minimum and maximum are reported. All parameter histograms resemble a lognormal distribution. The correlation length parameter (ξ) is used as a measure for the cluster radius. For the α 3K splice variant the concomitant distribution displays a mean of 56 ± 3 nm, with a minimum of 25 nm and maximum of 134 nm. For the α 3L splice variant the cluster size distribution is shifted towards larger radii. This is resembled by a mean value of 92 ± 4 nm, with a minimum of 51 nm and maximum of 197 nm. The average number of receptors in a cluster (N) is distributed between 3 and 72 for the α 3K splice variant. This parameter distribution shifted more than an order of magnitude for the α 3L splice variant, where the average cluster occupancy ranges from 22 to 895 receptors. The respective means of N for the α 3L and α 3K variants are 14 ± 2 and 220 ± 27 . In order to quantify cluster

occupation compensated for differences in cluster size, the cluster density was determined from N and ξ . Still the $\alpha 3L$ variant shows elevated values compared to $\alpha 3K$ with respective means of $9870 \pm 1433 \mu\text{m}^{-2}$ and $1747 \pm 200 \mu\text{m}^{-2}$. The last parameter ψ derived from the autocorrelation analysis shows the increased local density of receptors appearing in a cluster. For the $\alpha 3K$ splice variant the increased density ranges from 1 to 33 with a mean of 8 ± 1 . Also for this parameter the $\alpha 3L$ splice variant shows an elevated and wider range, starting at 5 and ending at 99 with a mean of 34 ± 3 .

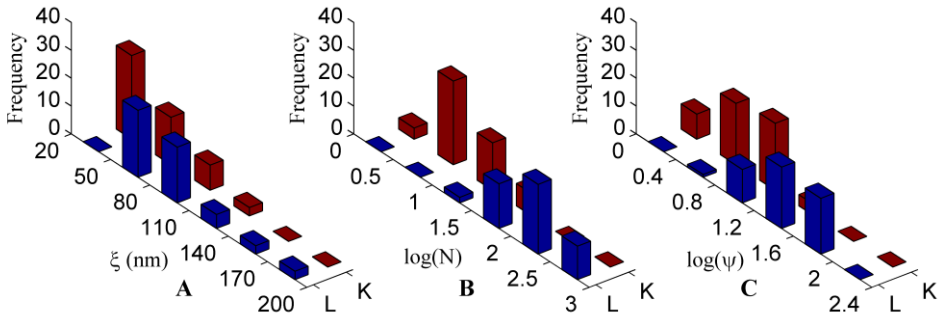


Figure 4.3: The clustering parameters derived from the autocorrelation fitting (Eq. 4.2) quantify the differential sub-diffraction organization of the GlyR $\alpha 3L$ (blue) and $\alpha 3K$ (red).

The parameters were determined for multiple bottom membrane areas ($\alpha 3K$, $n = 59$; $\alpha 3L$, $n = 55$) and show a lognormal distribution. The correlation length (ξ) is interpreted as the radius of the clusters and retrieved values range from ~ 20 nm to ~ 200 nm (A). N represents the average number of receptors in a cluster (B). As a relative measure, it shows the differential cluster occupation of the splice variants. Due to experimental limitations, it cannot be interpreted as an absolute measure. The parameter ψ (Eq. 4.5) is a measure of the local protein density increment in clusters, established by the ratio of the cluster protein density to the overall protein density of the membrane area (C). It shows the elevated affinity for the GlyR $\alpha 3L$ to enter into clusters compared to $\alpha 3K$.

4.4.4 Colocalization of the GlyR $\alpha 3$ splice variants

The dual-color super-resolution recordings show both GlyR $\alpha 3$ splice variants co-expressed in the bottom membrane of the same cell (Figure 4.4A,B). The $\alpha 3K$ receptor is still ubiquitously present in the cell membrane, yet there is a more grained appearance with the manifest presence of clusters. This is in contrast to the $\alpha 3L$ splice variant, which still shows strong clustering but is more distinctly spread out over the bottom membrane and the filopodia. More importantly, overlaying the super-resolution images reveals that some clusters from the two channels colocalize, meaning these clusters are actually occupied by both $\alpha 3K$

and $\alpha 3L$ splice variant receptors (**Figure 4.4C**). In order to quantify these clusters the correlation length of colocalization was determined by pair cross-correlation analysis (**Figure 4.4D**). Fitting of the cross-correlation (Eq. 4.6) yielded a spatial range of colocalization, which is interpreted as the radius of the colocalized clusters. The histogram of ξ^c resembles a lognormal distribution and has a minimum of 54 nm and a maximum of 205 nm with a mean of 94 ± 6 nm.

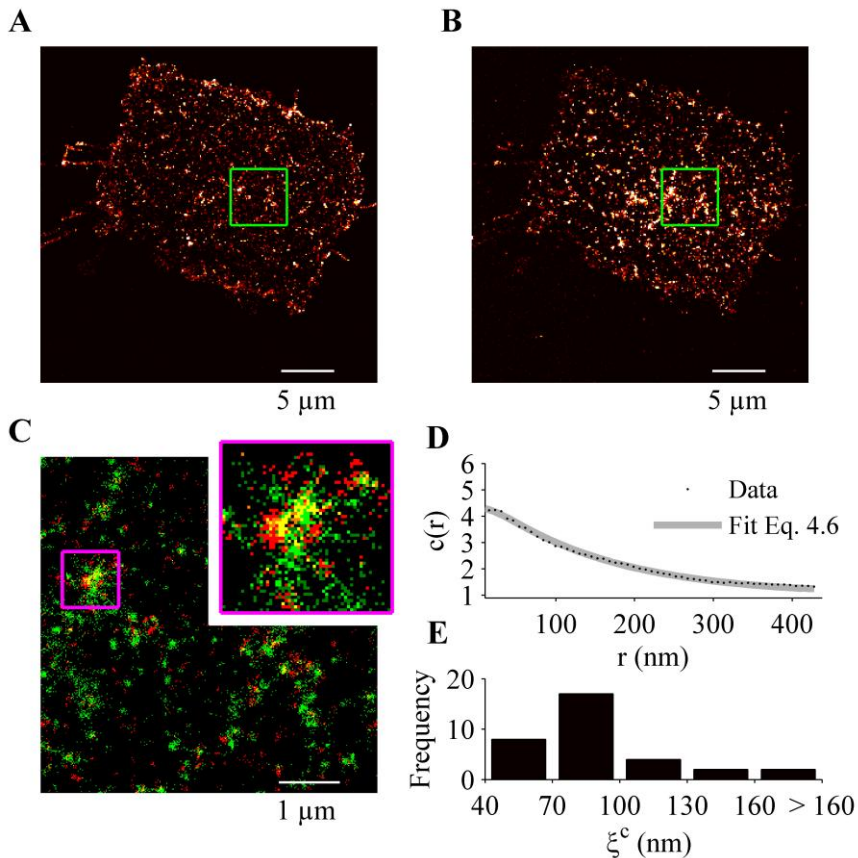


Figure 4.4: Co-expression of the GlyR $\alpha 3$ splice variants in HEK 293 cells, micrographs (A-C) and pair cross-correlation analysis (D,E).

The micrographs made from accumulated peaks in each individual channel, show the individual expression patterns for respectively the HA-GlyR $\alpha 3K$ and FLAG-GlyR $\alpha 3L$ upon co-expression (A,B). A bottom membrane area typically used for analysis is selected and the channels for the HA-GlyR $\alpha 3K$ (red) and FLAG- $\alpha 3L$ (green) splice variant are shown in overlay (C). The splice variants exhibit co-clustering (magenta inset). Fitting of the cross-correlation (Eq. 4.6) allows for the determination of the spatial scales of the co-clusters in the area selected in panel A and B (D). The cross-correlation length fit parameter (ξ^c), measured over multiple bottom membrane areas ($n = 33$) is shown in a histogram (E).

4.5 Discussion

The clustering state of GlyRs in the cell membrane has mainly been studied in relation to accumulation of neurotransmitter receptors at the postsynaptic terminal [378-381]. This process is facilitated by heteromeric assembly of GlyR channels, composed of ligand binding α -subunits and β -subunits required for anchoring to the gephyrin cytoskeletal matrix [147,152]. However, GlyR clustering has also been observed independently of gephyrin [149,330]. In our expression system we see clustering of homomeric $\alpha 3$ -subunit containing GlyRs. Given the homomeric nature of the GlyRs, the clustering phenomenon is probably not directly relevant to synaptic localization [138]. Nevertheless, evidence of a role for homomeric GlyRs as regulators of neurotransmitter release at presynaptic terminals has been found [157,159,160,175,382]. Moreover, it was shown that receptor clustering changes receptor desensitization [171], which may influence tonic inhibition of neuronal excitability through expression of weakly desensitizing non-synaptic GlyRs [166,168,169]. In this way modulation of GlyR electrophysiological properties via RNA splicing-dependent alteration of clustering properties can have profound effects on neuronal communication. Indeed, both on biophysical and physiological levels, RNA splicing has a profound impact on GlyR $\alpha 3$ properties [167,170,324]. In our experiments this is resembled by a distinct difference in membrane distribution. By diffraction-limited observation, it appears as if the $\alpha 3K$ splice variant is diffusely distributed while the $\alpha 3L$ is clustered. By applying dSTORM we see that both splice variants show non-random receptor distribution organized at a sub-diffraction level.

With accurate quantification, sub-diffraction information offers direct information on molecular organization and dynamics [229,263,383]. In this work pair correlation analysis is applied, which compensates for apparent clustering due to repeated localizations. In a large number of data sets for both splice variants, a measure of repeated localizations was identified and compensated. The reported measure (σ_s) of the localization uncertainty is elevated compared to precision derived from the Gaussian fitting profile ($\langle \sigma_{xy} \rangle = 17.6 \pm 0.8$ nm), but this is not unexpected as several experimental limitations lead to broadening of the PSF [246]. In addition the actual image resolution is also aggravated by limitations

imposed by labeling and photoswitching rates, making < 20 nm resolution hard to attain and obscuring features below this limit [384]. The introduction of a super-resolution PSF does however compensate for potential over-labeling of proteins due to multiple binding sites [246]. All GlyRs consist of pentameric subunit assemblies, thereby theoretically containing multiple binding sites for subunit targeting antibodies [106,170,301,385]. In case of PALM imaging this can be even more explicit, as in fusion constructs the fluorescent protein is incorporated at the level of the individual subunit [133,386].

The nature of the measured correlation was however not exclusively stochastic. For both GlyR $\alpha 3$ splice variants pair correlation analysis is able to describe clustering, regardless of the strong differences in membrane distribution apparent from the images. This demonstrates the flexibility of pair correlation analysis in objectively quantifying different clustering patterns. Furthermore, pair correlation analysis has also been applied to electron microscopy images, proving its general applicability for quantification of point maps [248]. The relative differences between the clustering properties of the GlyR $\alpha 3$ splice variants show that cluster occupation has the most distinction. The cluster size exhibits a clear shift in the distribution of the radii, yet a strong degree of overlap is present as the means remain in the same order of magnitude. Based solely on the cluster radius, the difference in clustering between the splice variants might be underestimated. The average number of receptors in a cluster however, displays a more differential view of clustering properties. Even when looking at the cluster density ($\rho^{cluster}$), thereby compensating for the smaller cluster size of the $\alpha 3K$ -variant, the $\alpha 3L$ -variant still shows strongly elevated values. The fact that $\alpha 3K$ -variant clusters are less dense is not due to a proportional decrease in membrane receptor density. Otherwise the cluster density increment (ψ) would be similar between the splice variants. Instead $\rho^{cluster}$ and $\psi = \rho^{cluster} / \rho^{protein}$ are both elevated for the $\alpha 3L$ -variant, revealing that the denser packing of the $\alpha 3L$ clusters is due to elevated affinity for clustering interactions. The receptor numbers reported here cannot be interpreted as an absolute number of receptors, given experimental limitations in photoswitching and labeling efficiency, but serve as a strongly differentiating relative measure [247]. Kinetic modeling allowing for counting of reversibly photoswitching fluorescent proteins with PALM has been established, however

comprehensive models for (d)STORM are lacking [387]. Calibration via reference structures can also be performed, yet limited knowledge about the GlyR clustering interactions impedes the formulation of such structures [245].

In physiological circumstances, both splice variants are expressed and their expression rates have patho-physiological implications. In severe cases of temporal lobe epilepsy the $\alpha 3K$ expression is upregulated at the expense of $\alpha 3L$ [170]. Information on colocalization of the splice variants is important with regard to pharmaceutical targeting of subunits. We find clear evidence that when co-expressed, both splice variants form clusters and these clusters can colocalize. Whether these co-clusters are the result of homomeric $\alpha 3$ variant GlyRs or heteromeric $\alpha 3K:\alpha 3L$ GlyRs cannot be determined here, yet other single molecule imaging strategies have been developed to resolve this matter [133]. The radius of the co-clusters is in the same order as the cluster radius identified for clusters of individually expressed receptors. This suggests that the splice variants, upon co-expression, cluster in the same microdomains as when individually expressed. However, the affinity for clustering in these microdomains still appears more dominant for the $\alpha 3L$ variant compared to $\alpha 3K$. These results do imply that any disruption of the receptor clustering will likely influence both splice variants, yet to a different extent.

The results from this work provide more information regarding the effect of RNA splicing on GlyR $\alpha 3$ biophysical membrane behavior. The local accumulation of the GlyR $\alpha 3$ splice variants corresponds proportionally to the immobile fraction detected with Single Particle Tracking (SPT) for the $\alpha 3K$ (5%) and $\alpha 3L$ variant (15%). Both SPT and temporal image correlation spectroscopy revealed the presence of multiple species in the diffusing population of $\alpha 3K$ and $\alpha 3L$ receptors [324,388]. This supports the notion that the GlyR $\alpha 3$ is capable of dynamically interacting in the membrane, with a splice variant-dependent affinity. The TM 3-4 region of cys-loop LGICs, where the 15 AA difference between the $\alpha 3$ splice variants is present, is known to determine receptor interactions in the membrane [389-391]. For the nicotinic acetyl choline receptor, lipid rafts are shown to be platforms mediating these interactions [392,393]. The cluster radii found here for the GlyR $\alpha 3$ are in the range (10 – 200 nm) of lipid raft domains [394]. However, future investigations will need to confirm whether RNA splicing effects on GlyR $\alpha 3$ membrane distribution are mediated via lipid rafts.

In summary, we used dSTORM to obtain super-resolution images of the membrane distribution of GlyR $\alpha 3$ splice variants. Both single- and dual-color imaging was applied to obtain information on the $\alpha 3K$ and $\alpha 3L$ variants expressed individually and together. Pair correlation analysis was used to quantify the membrane distribution using both the auto- and cross-correlation options. Repeated localization of emitters was successfully compensated and parameters on (co-)cluster size and cluster occupation were extracted. The results suggest both variants cluster via the same interactions, yet with strongly differing affinities. Although no definite clustering mechanism can be appointed yet, the role of RNA splicing in determining GlyR $\alpha 3$ distribution is better understood.

5 General discussion

5.1 Discussion

In order to put the work described in the previous chapters into perspective, referring to the main research question is a good starting point: Has optical sub-diffraction microscopy proven to be useful for the study of RNA splicing effects on GlyR $\alpha 3$ membrane properties? A confirmation of this can be found in the fact that both SPT and dSTORM imaging uncovered aspects of GlyR $\alpha 3$ membrane behavior previously obscured by the diffraction limit [324,388,395]. The direct observation of single particles allows for local observation of distinctive membrane properties. This is in contrast to ensemble average techniques designed to observe bulk signals and not capable of directly determining sub-diffraction anomalous characteristics [396-398]. However the heterogeneity found by single particle localization is best viewed together with the bulk image in order not to wrongfully interpret stochastic single particle behavior [324,399]. The extra post-processing required for extracting particle locations from images and forming trajectories can also introduce observation bias [192,246].

A major part of research involving localization based optical sub-diffraction microscopy is devoted to developing new and improved image processing and analysis algorithms. In this work local trajectory analysis, theoretical determination of the localization precision and pair correlation analysis were successfully applied to the GlyR $\alpha 3$ data [189,199,245,388,395]. Many publications now provide programmed algorithms or analysis modules as a supplement. This is an important step in unifying methodology, yet implementing the provided material in the existing work flow and extracting useful quantitative data are not trivial tasks. An apt reminder of this is found in the protocol published for pair correlation analysis, stating that a limitation for using the technique is [245]: “requires a skilled user with substantial knowledge of statistics, single-molecule photophysics and computer programming”. This quote accurately reflects the skills necessary for quantitative data extraction from biological systems studied by optical sub-diffraction microscopy.

Sub-diffraction quantitative data extraction of GlyR $\alpha 3$ membrane properties was used to test whether RNA splicing alters membrane order of the GlyR $\alpha 3$ on the nanoscopic scale, *i.e.* the primary hypothesis. Preceding, conventional microscopy and line intensity analysis had already established a quantitative

measure of the RNA splicing influence on membrane distribution of the GlyR $\alpha 3$ [170]. This approach was sufficient to confirm the immense difference in membrane distribution between the splice variants and even capable of detecting differences between homomeric ($\alpha 3L$) and heteromeric ($\alpha 3:\beta$) clusters. However, the diffraction limit is an obstacle for studying the nanoscale molecular architecture determining membrane receptor properties, such as the pre- and postsynaptic zones in neurons [400,401].

Before the advent of optical super-resolution microscopy and still today, ultrastructural analyses of the synapse are performed using electron microscopy and tomography [402,403]. To date, the resolution of electron microscopy is still considered superior to that of light microscopy [404]. However, comparative to electron microscopy, easy labeling and simultaneous 3D imaging of multiple synaptic components can readily be achieved with optical (fluorescent light) super-resolution microscopy [405]. A wide range of optical super-resolution microscopy strategies has now been used in the analysis of neuronal compartments and live neurons [406,407]. Regarding the inhibitory synapse, quantitative nanoscopy has been applied to study gephyrin assembly and GlyR binding sites [228]. No direct GlyR super-resolution imaging had been performed up until this work [395]. Here, GlyR $\alpha 3$ clustering in HEK 293 cells was extensively quantified, providing a direct correlation with the difference in desensitization relevant for extrasynaptic $\alpha 3$ GlyRs [166,169]. Clustering changes desensitization and may influence tonic inhibition of neuronal excitability [168,171]. Furthermore the intrinsic capability of the $\alpha 3$ splice variants to colocalize, is relevant in assessing the therapeutic potential of the GlyR in neuropsychiatric disorders [175,395,408].

Single particle tracking has recently also been applied as a super-resolution imaging technique, by combining it with PALM (sptPALM) [409]. Hereby high-density mapping of individual trajectories is used to extract dynamic information on a nanoscopic scale [410]. This kinematic analysis is not based on live-cell super-resolution microscopy achieving video-rate imaging of complete biological structures in 2 and 3D [411,412]. Instead individual organic fluorophores are tracked, which are cycled between ON and OFF states to obtain spatial label sparseness [413]. Classical single particle tracking studies are however not without merit in neuroscience, as they have elucidated many concepts in

synaptic biology [316]. Early studies described the dynamics of synaptic anchoring of glycine and glutamate receptors [147,150,318,322,414]. Later on single particle tracking was used to study homeostatic regulation of GABA, glycine and different types of glutamate receptors at synaptic sites and in relation to synaptic transmission [75,151,249,258,415,416].

Nearly all the aforementioned GlyR tracking studies applied quantum dots for tagging receptors, due to their long-term photostability [417]. The free diffusion coefficient retrieved in this work ($0.13 \mu\text{m}^2/\text{s}$) is in line with extrasynaptic diffusion coefficients measured for GlyRs expressed in primary neurons [150,152,388]. The transgenic expression level is expected to be higher in HEK 293 cells compared to primary neurons, yet the problem to identify single particles in live HEK 293 membranes with high receptor density was solved by managing the antibody concentration and pre-bleaching a fraction of the labeled receptors if required. Furthermore pentameric assembly is required for membrane trafficking of GlyRs expressed in mammalian cells, ensuring that the labeled GlyRs in the membrane are pentameric [126]. Both our own and other electrophysiological measurements of the GlyR $\alpha 3$ in HEK 293 cells also indicate a similar peak current amplitude for both $\alpha 3$ splice variants, suggesting similar numbers of functional pentameric receptors in the membrane [167,324]. This evidence contradicts the idea that functional pentameric receptors are only represented by the immobile or confined fraction of the receptor pool, which is significantly larger for the $\alpha 3L$ splice variant [324,395].

The essential role of sub-diffraction imaging and particle tracking in understanding neurotransmitter receptor signaling, is supported by the abundance of studies referenced in the work. Importantly these studies were based on previously established molecular interactions or physiological concepts in synaptic biology [418]. Regarding the non-synaptic or homomeric GlyR $\alpha 3$, a similar background was not available. Therefore, a more exploratory strategy, based on analyzing inherent receptor diffusion and distribution properties, was followed. Studying inherent receptor diffusion and distribution, meant that in both cases the randomness expected to govern these processes was evaluated. Establishing the occurrence of non-randomness does not directly provide information on the interfering mechanistic. Instead the available parameters are compared to known mechanisms leading to non-random membrane receptor

behavior. While doing so, the experimental limitations of the spatial and temporal range available to describe receptor properties are taken into account.

In the case of diffusion, the physical descriptors of Brownian motion are used to determine randomness, *e.g.* the diffusion coefficient and anomalous α -exponent. The accuracy of these statistical descriptors associated with an individual trajectory is limited due to the finite observation time [194]. This calls for an ensemble evaluation of many trajectories [192]. The ensemble analyses performed on the GlyR $\alpha 3$ trajectories in this work show the presence of non-random or anomalous diffusion by providing multiple lines of evidence for heterogeneous populations among the tracked receptors. First there is a broad distribution of short range diffusion coefficients and an immobile fraction [324]. Second, long-term evaluation of the MSD versus time relation shows significant deviations from linearity [324,388]. Finally the cumulative distribution function of the square displacements requires a multi-exponential approximation for accurate description and the slow diffusing sub-population of receptors shows a non-linear MSD versus time relation [388]. Together these findings suggest the heterogeneously diffusing receptor population is composed of receptors displaying free diffusion, no diffusion, sub-diffusion and super-diffusion over the available observation times. These four types of receptor diffusion have been identified in several single particle tracking diffusion studies of transmembrane proteins [70,255,308]. Furthermore, diffusion coefficients are in the expected range for fluorescently labeled transmembrane proteins which display free and confined diffusion at 37°C, among which the GlyR $\alpha 1$ [150,152,203,419,420].

The findings of anomalous diffusion were corroborated with the identification of transient confined and directed motion anomalies in the trajectories [388]. Mapping of the confinement anomalies showed locally reoccurring areas where the receptors resided much longer than expected for normal diffusion. Together with sub-diffusion on long time scales, this confinement is indicative of trapping via corralling or tethering and contra-indicates sub-diffusion due to obstacles [308]. Transient trapping on a time scale of seconds in areas defined by a diameter of 100-600 nm, strongly suggests an influence of previously defined transient confinement zones (TCZs) on receptor diffusion [85,199]. The model concept of a TCZ is a small obstacle rich membrane area, often considered to be a membrane raft, temporarily confining receptor motion [205,421]. This is

different from general sub-diffusion due to spaced obstacles, as with TCZs small dispersed obstacle fields act as corrals [422]. The non-linear diffusion behaviour of the slow diffusing species from the ensemble square displacement analysis could be representative of constrained diffusion inside highly dense obstacle fields [388,423]. On the other hand, cross-linking has also been implicated for TCZ association of transmembrane proteins. Cross-links could occur by oligomerization or tethering by sub-membranous components and subsequent receptor confinement could also explain the non-linear diffusion behaviour [95,152,421]. Some binding proteins important in neurotransmitter receptor tethering are known to be raft-associated proteins, thereby unifying raft association and tethering as a mechanism of TCZ association [393,424]. The classical membrane skeleton model as mediator of GlyR $\alpha 3$ confinement is contra-indicated by the fraction of freely diffusing molecules and the transient free and confined diffusion suggestive of large interdomain distances [70,255,422]. However, an influence of the cytoskeleton according to the modern "picket-fence" model cannot be excluded. This model describes millisecond confinement events, which can only be evaluated by microsecond frame rates [72,74]. The cytoskeleton is also related to rafts coalescence and stability, thereby possible having an indirect influence on TCZs [93,94,425].

The presence of super-diffusion derived from the ensemble analysis corresponds well with the detection of conveyor belt motion in the receptor trajectories [198,324,388]. The parameters quantifying this transport strongly suggest motor-driven vesicular transport along microtubules [77-80]. It must be mentioned that given the limited observation time and high free diffusion coefficient, fast long-range transport is likely to be the only type of directed motion detectable by the local trajectory analysis. The presence of slower ($\mu\text{m}/\text{min}$) forms of directed motion can thereby not be excluded, yet no motion patterns were observed to suspect their presence [75,76]. The appearance of back-to-back directed - confined motion and vice versa suggests the anomalous diffusion is related to a receptor transport process [388]. Membrane rafts have been suggested as important regulators of endo- and exocytic pathways, creating a possible link between TCZs and directed motion [426]. Endocytosis is a well studied process, usually divided into clathrin- and non-clathrin-mediated routes [427]. Lipid raft mediated endocytosis is considered a clathrin-

independent route of internalization, mediated via caveolins or other membrane proteins [49,426-428]. However, association of membrane proteins with developing clathrin-coated pits (CCPs) has also been suggested as a cause of transmembrane protein confinement, with the confinement domains similar in size to the TCZs of the GlyR $\alpha 3$ [388,420,429,430]. Furthermore, the dynamics of cargo recruitment to CCPs are described as a catch-and-release process, dependent on cargo affinity to the CCP [431]. This process is in agreement with the transient nature of GlyR $\alpha 3$ confinement and displays a similar time scale [388,431]. Receptor confinement could thus be regarded as a cargo accumulating maturation step for internalization or a transient phase in stop-and-go saltatory motion during sub-membranous receptor recycling. Directed motion would thereby occur directly after scission of the vesicle and as part of the receptor sorting process. A coalescence of GlyRs in relation to internalization and transport was not systematically observed. The low labelling density required for SPT may obscure other receptors recruited to the internalization site.

The presence of randomly distributed GlyR $\alpha 3$ clusters with no specific shape, as determined with dSTORM, supports the idea of a composite GlyR $\alpha 3$ receptor distribution [395]. This composite distribution exists of receptors randomly distributed and receptors ordered in clusters. It corresponds well with the composite diffusion pattern, displaying fast freely diffusing and slow confined receptors [388]. Furthermore, the spatial scales of the TCZs determined by diffusion measurements (~ 150 nm) and clusters determined by super-resolution imaging (~ 100 nm) are in the same order [388,395]. The values reported here correspond to domain radii, which makes the involvement of caveolae possessing a diameter of 60-80 nm unlikely [49]. Other types of membrane rafts, measuring >100 nm in size, have been reported, which would be better suited to underlie the GlyR $\alpha 3$ membrane domains [40,236]. Modern insights into raft dynamics suggest that raft coalescence is required in order to form domains with similar size and protein occupation as the GlyR $\alpha 3$ clusters [52,92,93]. Clathrin assemblies also have appropriate length scales to accommodate GlyR $\alpha 3$ clusters, as CCPs have a reported width of 150-200 nm and flat clathrin arrays can be even larger [225,432].

By executing each type of experiment using both GlyR $\alpha 3$ splice variants, we effectively studied the effect of the 15 AA insert differentiating the $\alpha 3K$ and $\alpha 3L$ variant. As the insert is only a small segment of the subunit (15 AA of 464 AA in total) and located in the cytoplasmatic loop, differences in receptor behavior can be considered as manifestations of differential interaction capabilities conveyed to the subunit [61,167,170]. These interaction capabilities refer to the many possibilities of membrane inserted GlyR association with itself or components in the membrane environment. Diffraction-limited and ensemble average techniques revealed completely differential membrane diffusion and distribution between the splice variants [170,324]. These results suggest the $\alpha 3L$ variant is capable of interacting, and the $\alpha 3K$ variant is not. The results obtained with optical sub-diffraction microscopy also reveal differential membrane properties between the splice variants, but offer more detail on their origin [388,395]. This is due to the possibility to analyze dynamics on a single receptor level and spatial distributions on a nanoscopic scale. Instead of suggesting an interacting and non-interacting variant, the conclusion of the sub-diffraction measurements is that both variants are capable of a similar interaction, yet with strongly differing efficiencies. This conclusion is based on the findings that both splice variants display differing degrees of sub-diffusion, local transient confined motion, sub-diffraction clustering and are capable of co-clustering.

How can the molecular biology of GlyR $\alpha 3$ RNA splicing account for the findings of sub-diffraction microscopy? The presence of the 15 AA insert is known to stabilize the fold of the cytoplasmatic loop of the GlyR $\alpha 3$ [174]. This domain is essential for trafficking, functional modulation and membrane localization of GlyRs [122,433]. Both variants harbor a di-leucine motif in the cytoplasmatic loop, required for AP-2 dependent clathrin endocytosis [167,434]. The GlyR $\alpha 1$ is prone to clathrin-mediated endocytosis and clathrin-mediated endocytic recycling of AMPA receptors has proven essential in synaptic potentiation [145,333]. On the other hand, the cytoplasmatic loop may also mediate translocation of the GlyR $\alpha 3$ to lipid rafts by interaction with raft associated components. Several ionotropic neurotransmitter receptors are shown to be associated with rafts and rafts play an important role in synapse receptor homeostasis [257,424,435,436]. The nAChR LGIC is shown to be anchored at the neuromuscular synapse by the raft associated protein rapsyn [393,437].

However, at present no GlyR specific molecular evidence has been reported to support this. RNA splicing could thus influence GlyR $\alpha 3$ signaling capabilities via regulating affinity for clathrin structures, rafts or other unknown components. Regulation of interaction affinity via RNA splicing has recently been demonstrated for the GlyR $\alpha 3$ interaction with Sec8, a vesicular transport protein involved in targeting membrane material to presynaptic sites [175,438]. Alternative splicing can thereby regulate GlyR $\alpha 3$ trafficking, shown by Sec8 driven axonal targeting of $\alpha 3L$ GlyRs [175]. This provides a strong precursor for the differential regulation of the GlyR $\alpha 3$ cytoplasmic loop interaction affinity by RNA splicing.

5.2 Future perspectives

Since the start of the research presented here, in 2010, many parallel advances have been made in the field of GlyR biology and optical sub-diffraction microscopy. The study of neurotransmitter receptor biology is ever more frequently performed using optical sub-diffraction imaging modalities, demonstrating the power of this experimental approach [204,228,409]. Continuation of the GlyR $\alpha 3$ research using optical sub-diffraction microscopy can proceed along two paths. First, the presented methodological approach of this work can be used to further explore the molecular interactions behind the current GlyR $\alpha 3$ membrane properties. Second, experimentation can be taken to the next level by applying new, more advanced methodology in biology and optical sub-diffraction microscopy.

The current experimental approach offers a platform to determine the molecular and physiological nature of the GlyR $\alpha 3$ interactions in the membrane. A standard approach is the use of chemical agents to selectively disrupt the relevant processes. A first example is the use of Latrunculin A and nocodazole for disruption of respectively actin and tubulin cytoskeletal components [69,142,151]. The effect of cytoskeletal disruption on confinement and clustering cannot readily be predicted, yet it should abolish the directed motion observed for the GlyR $\alpha 3L$. A second option is the application of cholesterol depletion by methyl- β -cyclodextrin or other agents in order to perturb cholesterol-based membrane rafts [393,419]. If such rafts serve as TCZs for GlyR $\alpha 3$ receptors, cholesterol depletion should significantly reduce receptor confinement. If receptor confinement in cholesterol based raft TCZs is prerequisite for internalization and trafficking, directed motion should also be influenced. The role of internalization processes can also be studied by applying inhibitors, such as dynasore or wortmannin which block clathrin-mediated endocytosis [439,440]. However, all these chemical treatments have pleiotropic effects due to the pivotal roles of the influenced components in general cell physiology [441-443]. Modulating specific interaction targets, such as performing knockdown of Sec8, would suffer less from this drawback. Problems with integrity of the bottom membrane during cellular modulation can be solved by selecting a more robust cell line for GlyR expression, *e.g.* HeLa cells [152].

A more elegant but less direct approach, would be to perform dual-color imaging of the GlyR $\alpha 3$ receptor and the expected interaction components. This approach would be similar to the co-localization experiments performed for the study of splice variant co-clustering by multi-color dSTORM [395]. Staining antibodies and fluorescent fusion-protein analogs are readily available for endocytosis machinery and cytoskeletal components. Even for different types of lipid rafts, optical super-resolution microscopy probes have been developed [236]. The evidence would be even more convincing if co-localization were established in dynamic live cell processes. Fluorescent fusion-protein analogs of intracellular components and antibody labeling of extracellular components would allow for the monitoring spatial interactions under physiological circumstances. In such instances, the use of quantum dots for tracking the GlyRs is favorable, as long term observation facilitates characterization of the interaction process [150,152,417].

A third possible approach is based on determining the effects of GlyR $\alpha 3$ subunit sequence modifications on membrane behaviour. A mutational study of the 15 AA insert already revealed important effects on channel gating and domain structure of the GlyR $\alpha 3$ [174]. A similar strategy can be applied to determine specific amino acids or motifs responsible for differential diffusion and distribution of the splice variants. Furthermore, the most important pathophysiological results for the GlyR $\alpha 3$ have been coupled to a gain-of-function GlyR $\alpha 3$ variant, showing upregulation in response to hyperexcitability and the capability to induce neuropsychiatric symptoms in a mouse model [168,175]. This RNA edited GlyR $\alpha 3$ variant has a change in amino acid position 185, where proline is substituted by leucine (GlyR $\alpha 3^{P185L}$)[169]. Studying the membrane properties of this variant would be more appropriate for relating membrane behavior to pathophysiology. However, the amino acid substitution occurs in the extracellular N-terminal domain, which is not expected to directly alter membrane properties [169].

The additional experiments suggested up to this point can be performed with relatively minor adaptations to protocols applied in this work. However, more efficient data processing and relevant quantitative measures can be extracted using new and more advanced methods. With regards to neurobiology, experiments using primary cultured neurons present an obvious next step

[316,418]. These experiments can provide more details on presynaptic targeting and the protein architecture of axonal Sec8 containing clusters of the GlyR $\alpha 3$. A drawback is that this will require repetitive isolation of primary cells, which are difficult to transfect and have limited culture capacity [444-446]. Nonetheless, moving closer to *in vivo* settings is essential if experimental findings are to be interpreted in a clinical setting such as epilepsy or anxiety [168,175].

The construction of a functional GlyR $\alpha 3$ fluorescent fusion subunit can also facilitate optical sub-diffraction microscopy, by superseding antibody labeling and thus avoiding antibody binding and labeling issues [447]. The fact that each subunit would contain a fluorescent protein can be used to evaluate a possible heteromeric GlyR stoichiometry in $\alpha 3L$ and $\alpha 3K$ co-expression experiments [133]. Furthermore, incorporation of a photoswitchable fluorescent protein, such as mEos 3.2, would allow us to apply the PALM and sptPALM [413,448]. With PALM more accurate estimates of receptor numbers can be obtained from super-resolution images via kinetic blinking models [387]. With sptPALM high-density dynamic and spatial information can be obtained, allowing more extensive quantification similar to AMPA receptor studies in neuronal dendrites [409,410]. For GlyR $\alpha 3$ RNA splicing research an N-terminal location of the fluorescent protein would be desired instead of the classic cytoplasmatic loop location, as the latter harbors the 15 AA insert critical in GlyR $\alpha 3$ RNA splicing [133,167,449,450].

In order to maximize information extraction, the algorithms used to identify particles and form trajectories can be improved [315,451-455]. Implementing a Bayesian approach to particle localization and subsequent data analysis can be particularly interesting, as it calculates the probability of *a priori* specified models instead of requiring arbitrary *a posteriori* model selection [456-459]. By such an approach, any user bias is documented in the *a priori* specified models, with further Bayesian inference occurring without user intervention [457]. Furthermore, optical sub-diffraction microscopy can explore the axial dimension by adapting the microscope optics and particle detection algorithms to the selected 3D imaging strategy [227,460]. A relatively old and straightforward strategy to achieve this, is based on placing a cylindrical lens in the emission path, creating an astigmatic PSF dependent on the axial position of the particle [461]. Astigmatism is now used again in modern localization based super-

resolution image reconstruction and particle tracking [225,462]. Obtaining accurate 3D information can be used to study the relation between the axial dimension and clustering-anomalous diffusion, as it can reveal the influence of membrane undulations or internalization processes even in live cells [412,463]. Live cell localization based super-resolution imaging of intra- and extracellular structures can be achieved using fluorescent proteins and synthetic fluorophores [464-466]. The latter class of fluorophores can be fused to transfected intracellular proteins in live cells via special tags [467,468]. The intracellular levels of oxygen and glutathione (GSH) allow photoswitching inside live cells, yet cellular damage due to radical formation must be considered in all live cell experiments using photoswitching of synthetic fluorophores [278].

5.3 Conclusion

In this work, localization based optical sub-diffraction microscopy is applied to measure the nanoscale membrane order of the GlyR $\alpha 3$ in HEK 293 cells. Both lateral membrane diffusion and spatial membrane distribution were measured to determine the effect of the $\alpha 3K$ and $\alpha 3L$ alternate splice variants. Diffusion measurements were performed by single particle tracking of fluorescently labeled GlyR $\alpha 3K$ or $\alpha 3L$ in the bottom cell membrane. Ensemble analysis of the trajectories revealed the presence of anomalous sub- and super-diffusion, which was confirmed by local trajectory analysis. Both splice variants showed anomalous sub-diffusion, identified as local receptor confinement in transient confinement zones. The $\alpha 3L$ variant receptors also showed a small fraction of super-diffusion. This directed motion was interpreted as transient conveyor belt type motion and was often preceded or followed by confined motion. The spatial distribution of the individual GlyR $\alpha 3$ splice variants in the membrane was studied by using dSTORM to create super-resolution localization maps. Analysis of these localization maps using pair correlation analysis revealed clustering of both variants. The cluster radius was slightly elevated for the $\alpha 3L$ variant, but $\alpha 3L$ clusters also revealed a higher density of receptors due to an increased affinity for clustering. Furthermore, dual-color dSTORM and pair correlation analysis revealed that, when co-expressed, the splice variant clusters partially colocalize. The co-clusters are of similar size as individual $\alpha 3L$ clusters. The aforementioned quantitative measures of diffusion and spatial distribution suggest RNA splicing determines GlyR $\alpha 3$ interaction efficiency in the membrane. More specifically, the measurement parameters suggest interaction with clathrin structures or membrane rafts. In the future, this work can be used as a foundation to uncover the actual molecular nature of GlyR $\alpha 3$ membrane interaction.

Reference list

Reference list

- [1] D. Deamer, J.P. Dworkin, S.A. Sandford, M.P. Bernstein, L.J. Allamandola, The first cell membranes, *Astrobiology*, 2 (2002) 371-381.
- [2] J.P. Schrum, T.F. Zhu, J.W. Szostak, The origins of cellular life, *Cold Spring Harbor perspectives in biology*, 2 (2010) a002212.
- [3] N. Lane, W.F. Martin, The origin of membrane bioenergetics, *Cell*, 151 (2012) 1406-1416.
- [4] B. Alberts, *Molecular biology of the cell*, 4th ed / Bruce Alberts ... [et al.] ed., Garland Science, New York, 2002.
- [5] C.E. Overton, *Studien über die Narkose zugleich ein Beitrag zur allgemeinen Pharmakologie*, Fischer, 1901.
- [6] H. Meyer, *Zur Theorie der Alkoholnarkose*, *Archiv f. experiment. Pathol. u. Pharmacol*, 42 (1899) 109-118.
- [7] G. Quincke, *Ueber die physikalischen Eigenschaften dünner, fester Lamellen*, *Annalen der Physik*, 271 (1888) 561-580.
- [8] B.A. Lewis, D.M. Engelman, Lipid bilayer thickness varies linearly with acyl chain length in fluid phosphatidylcholine vesicles, *J Mol Biol*, 166 (1983) 211-217.
- [9] G.M. Cooper, R.E. Hausman, *The cell : a molecular approach*, 3rd ed. / Geoffrey M. Cooper, Robert E. Hausman. ed., ASM Press, Washington, D.C., 2004.
- [10] E. Gorter, F. Grendel, *On Bimolecular Layers of Lipoids on the Chromocytes of the Blood*, *The Journal of experimental medicine*, 41 (1925) 439-443.
- [11] J.D. Robertson, *The molecular structure and contact relationships of cell membranes*, *Progress in biophysics and molecular biology*, 10 (1960) 343-418.
- [12] J.D. Robertson, *Membrane structure*, *The Journal of cell biology*, 91 (1981) 189s-204s.
- [13] C. Tanford, *The hydrophobic effect and the organization of living matter*, *Science*, 200 (1978) 1012-1018.
- [14] S.J. Singer, G.L. Nicolson, *The fluid mosaic model of the structure of cell membranes*, *Science*, 175 (1972) 720-731.
- [15] G. Guidotti, *Membrane proteins*, *Annual review of biochemistry*, 41 (1972) 731-752.
- [16] T.L. Steck, *The organization of proteins in the human red blood cell membrane. A review*, *The Journal of cell biology*, 62 (1974) 1-19.
- [17] S.J. Singer, *The molecular organization of membranes*, *Annual review of biochemistry*, 43 (1974) 805-833.
- [18] P.C. Driscoll, A.L. Vuidepot, *Peripheral membrane proteins: FYVE sticky fingers*, *Current biology : CB*, 9 (1999) R857-860.
- [19] G.A. Cross, *Glycolipid anchoring of plasma membrane proteins*, *Annual review of cell biology*, 6 (1990) 1-39.
- [20] J.P. Whitelegge, *Integral membrane proteins and bilayer proteomics*, *Analytical chemistry*, 85 (2013) 2558-2568.
- [21] D.M. Engelman, T.A. Steitz, A. Goldman, *Identifying nonpolar transbilayer helices in amino acid sequences of membrane proteins*, *Annual review of biophysics and biophysical chemistry*, 15 (1986) 321-353.
- [22] M.L. Jennings, *Topography of membrane proteins*, *Annual review of biochemistry*, 58 (1989) 999-1027.

-
- [23] S.K. Buchanan, Beta-barrel proteins from bacterial outer membranes: structure, function and refolding, *Current opinion in structural biology*, 9 (1999) 455-461.
- [24] A.N. Glazer, Energy and signal transduction by transmembrane protein complexes, *Nature*, 321 (1986) 646-647.
- [25] S. Ito, Form and function of the glycocalyx on free cell surfaces, *Philosophical transactions of the Royal Society of London. Series B, Biological sciences*, 268 (1974) 55-66.
- [26] W. Curatolo, The physical properties of glycolipids, *Biochimica et biophysica acta*, 906 (1987) 111-136.
- [27] R.K. Yu, Y.T. Tsai, T. Ariga, M. Yanagisawa, Structures, biosynthesis, and functions of gangliosides--an overview, *Journal of oleo science*, 60 (2011) 537-544.
- [28] C.G. Gahmberg, M. Tolvanen, Why mammalian cell surface proteins are glycoproteins, *Trends in biochemical sciences*, 21 (1996) 308-311.
- [29] S.M. Haslam, H.R. Morris, A. Dell, Mass spectrometric strategies: providing structural clues for helminth glycoproteins, *Trends in parasitology*, 17 (2001) 231-235.
- [30] L. Kjellen, U. Lindahl, Proteoglycans: structures and interactions, *Annual review of biochemistry*, 60 (1991) 443-475.
- [31] J.E. Rothman, J. Lenard, Membrane asymmetry, *Science*, 195 (1977) 743-753.
- [32] M.R. Clark, Flippin' lipids, *Nature immunology*, 12 (2011) 373-375.
- [33] F. Wunderlich, W. Kreutz, P. Mahler, A. Ronai, G. Heppeler, Thermotropic fluid goes to ordered "discontinuous" phase separation in microsomal lipids of *Tetrahymena*. An X-ray diffraction study, *Biochemistry*, 17 (1978) 2005-2010.
- [34] A. Wisniewska, J. Draus, W.K. Subczynski, Is a fluid-mosaic model of biological membranes fully relevant? Studies on lipid organization in model and biological membranes, *Cellular & molecular biology letters*, 8 (2003) 147-159.
- [35] M.J. Karnovsky, A.M. Kleinfeld, R.L. Hoover, R.D. Klausner, The concept of lipid domains in membranes, *The Journal of cell biology*, 94 (1982) 1-6.
- [36] J.H. Ipsen, G. Karlstrom, O.G. Mouritsen, H. Wennerstrom, M.J. Zuckermann, Phase equilibria in the phosphatidylcholine-cholesterol system, *Biochimica et biophysica acta*, 905 (1987) 162-172.
- [37] L.J. Pike, Lipid rafts: heterogeneity on the high seas, *The Biochemical journal*, 378 (2004) 281-292.
- [38] D.A. Brown, E. London, Structure and function of sphingolipid- and cholesterol-rich membrane rafts, *The Journal of biological chemistry*, 275 (2000) 17221-17224.
- [39] S. Munro, Lipid rafts: elusive or illusive?, *Cell*, 115 (2003) 377-388.
- [40] L.J. Pike, Rafts defined: a report on the Keystone Symposium on Lipid Rafts and Cell Function, *Journal of lipid research*, 47 (2006) 1597-1598.
- [41] M. Edidin, Lipid microdomains in cell surface membranes, *Current opinion in structural biology*, 7 (1997) 528-532.
- [42] D.A. Brown, J.K. Rose, Sorting of GPI-anchored proteins to glycolipid-enriched membrane subdomains during transport to the apical cell surface, *Cell*, 68 (1992) 533-544.
-

Reference list

- [43] K.A. Melkonian, A.G. Ostermeyer, J.Z. Chen, M.G. Roth, D.A. Brown, Role of lipid modifications in targeting proteins to detergent-resistant membrane rafts. Many raft proteins are acylated, while few are prenylated, *The Journal of biological chemistry*, 274 (1999) 3910-3917.
- [44] D.A. Zacharias, J.D. Violin, A.C. Newton, R.Y. Tsien, Partitioning of lipid-modified monomeric GFPs into membrane microdomains of live cells, *Science*, 296 (2002) 913-916.
- [45] F.A. Nezil, M. Bloom, Combined influence of cholesterol and synthetic amphiphilic peptides upon bilayer thickness in model membranes, *Biophys J*, 61 (1992) 1176-1183.
- [46] M. Gandhavadi, D. Allende, A. Vidal, S.A. Simon, T.J. McIntosh, Structure, composition, and peptide binding properties of detergent soluble bilayers and detergent resistant rafts, *Biophys J*, 82 (2002) 1469-1482.
- [47] A.G. Lee, Lipid-protein interactions, *Biochemical Society transactions*, 39 (2011) 761-766.
- [48] E.J. Smart, G.A. Graf, M.A. McNiven, W.C. Sessa, J.A. Engelman, P.E. Scherer, T. Okamoto, M.P. Lisanti, Caveolins, liquid-ordered domains, and signal transduction, *Molecular and cellular biology*, 19 (1999) 7289-7304.
- [49] R.G. Parton, K. Simons, The multiple faces of caveolae, *Nat Rev Mol Cell Biol*, 8 (2007) 185-194.
- [50] K. Simons, D. Toomre, Lipid rafts and signal transduction, *Nat. Rev. Mol. Cell. Biol.*, 1 (2000) 31-39.
- [51] K. Simons, E. Ikonen, Functional rafts in cell membranes, *Nature*, 387 (1997) 569-572.
- [52] K. Simons, J.L. Sampaio, Membrane organization and lipid rafts, *Cold Spring Harbor perspectives in biology*, 3 (2011) a004697.
- [53] H. Sprong, P. van der Sluijs, G. van Meer, How proteins move lipids and lipids move proteins, *Nat Rev Mol Cell Biol*, 2 (2001) 504-513.
- [54] M. Edidin, Lipids on the frontier: a century of cell-membrane bilayers, *Nat Rev Mol Cell Biol*, 4 (2003) 414-418.
- [55] H.C. Berg, *Random walks in biology*, Princeton University Press, Princeton ; Guildford, 1983.
- [56] A. Einstein, Über die von der molekularkinetischen Theorie der Wärme geforderte Bewegung von in ruhenden Flüssigkeiten suspendierten Teilchen, *Annalen der Physik*, 322 (1905) 549-560.
- [57] C. Bigg, Evident atoms: visibility in Jean Perrin's Brownian motion research, *Stud Hist Philos Sci*, 39 (2008) 312-322.
- [58] J.S. Perrin, *Les Atomes ... Avec 13 figures*. Deuxième édition, Paris, 1913.
- [59] L.D. Frye, M. Edidin, The rapid intermixing of cell surface antigens after formation of mouse-human heterokaryons, *J Cell Sci*, 7 (1970) 319-335.
- [60] M. Edidin, T.Y. Wei, Diffusion rates of cell surface antigens of mouse-human heterokaryons. I. Analysis of the population, *The Journal of cell biology*, 75 (1977) 475-482.
- [61] P.G. Saffman, M. Delbruck, Brownian motion in biological membranes, *Proc. Natl. Acad. Sci. U. S. A.*, 72 (1975) 3111-3113.
- [62] E.P. Petrov, P. Schwille, Translational diffusion in lipid membranes beyond the Saffman-Delbruck approximation, *Biophys J*, 94 (2008) L41-43.

-
- [63] Y. Gambin, R. Lopez-Esparza, M. Reffay, E. Sieracki, N.S. Gov, M. Genest, R.S. Hodges, W. Urbach, Lateral mobility of proteins in liquid membranes revisited, *Proc. Natl. Acad. Sci. U. S. A.*, 103 (2006) 2098-2102.
- [64] G. Vereb, J. Szollosi, J. Matko, P. Nagy, T. Farkas, L. Vigh, L. Matyus, T.A. Waldmann, S. Damjanovich, Dynamic, yet structured: The cell membrane three decades after the Singer-Nicolson model, *P Natl Acad Sci USA*, 100 (2003) 8053-8058.
- [65] A. Tsuji, S. Ohnishi, Restriction of the lateral motion of band 3 in the erythrocyte membrane by the cytoskeletal network: dependence on spectrin association state, *Biochemistry*, 25 (1986) 6133-6139.
- [66] M.P. Sheetz, S. Turney, H. Qian, E.L. Elson, Nanometre-level analysis demonstrates that lipid flow does not drive membrane glycoprotein movements, *Nature*, 340 (1989) 284-288.
- [67] G.J. Doherty, H.T. McMahon, Mediation, modulation, and consequences of membrane-cytoskeleton interactions, *Annual review of biophysics*, 37 (2008) 65-95.
- [68] D.W. Pumplin, R.J. Bloch, The membrane skeleton, *Trends Cell Biol*, 3 (1993) 113-117.
- [69] A. Kusumi, Y. Sako, Cell surface organization by the membrane skeleton, *Current opinion in cell biology*, 8 (1996) 566-574.
- [70] A. Kusumi, Y. Sako, M. Yamamoto, Confined lateral diffusion of membrane receptors as studied by single particle tracking (nanovid microscopy). Effects of calcium-induced differentiation in cultured epithelial cells, *Biophys. J.*, 65 (1993) 2021-2040.
- [71] A. Tsuji, K. Kawasaki, S. Ohnishi, H. Merkle, A. Kusumi, Regulation of band 3 mobilities in erythrocyte ghost membranes by protein association and cytoskeletal meshwork, *Biochemistry*, 27 (1988) 7447-7452.
- [72] T. Fujiwara, K. Ritchie, H. Murakoshi, K. Jacobson, A. Kusumi, Phospholipids undergo hop diffusion in compartmentalized cell membrane, *The Journal of cell biology*, 157 (2002) 1071-1081.
- [73] A. Kusumi, C. Nakada, K. Ritchie, K. Murase, K. Suzuki, H. Murakoshi, R.S. Kasai, J. Kondo, T. Fujiwara, Paradigm shift of the plasma membrane concept from the two-dimensional continuum fluid to the partitioned fluid: high-speed single-molecule tracking of membrane molecules, *Annu. Rev. Biophys. Biomol. Struct.*, 34 (2005) 351-378.
- [74] K. Suzuki, K. Ritchie, E. Kajikawa, T. Fujiwara, A. Kusumi, Rapid hop diffusion of a G-protein-coupled receptor in the plasma membrane as revealed by single-molecule techniques, *Biophys. J.*, 88 (2005) 3659-3680.
- [75] A. Serge, L. Fourgeaud, A. Hemar, D. Choquet, Active surface transport of metabotropic glutamate receptors through binding to microtubules and actin flow, *J Cell Sci*, 116 (2003) 5015-5022.
- [76] M. de Brabander, R. Nuydens, A. Ishihara, B. Holifield, K. Jacobson, H. Geerts, Lateral diffusion and retrograde movements of individual cell surface components on single motile cells observed with Nanovid microscopy, *The Journal of cell biology*, 112 (1991) 111-124.
- [77] J.P. Caviston, E.L. Holzbaur, Microtubule motors at the intersection of trafficking and transport, *Trends Cell Biol*, 16 (2006) 530-537.
- [78] S.P. Gross, Hither and yon: a review of bi-directional microtubule-based transport, *Physical biology*, 1 (2004) R1-11.
-

Reference list

- [79] M.C. Beckerle, Microinjected fluorescent polystyrene beads exhibit saltatory motion in tissue culture cells, *The Journal of cell biology*, 98 (1984) 2126-2132.
- [80] R.D. Vale, F. Malik, D. Brown, Directional instability of microtubule transport in the presence of kinesin and dynein, two opposite polarity motor proteins, *The Journal of cell biology*, 119 (1992) 1589-1596.
- [81] K. Jacobson, E.D. Sheets, R. Simson, Revisiting the fluid mosaic model of membranes, *Science*, 268 (1995) 1441-1442.
- [82] P.F. Almeida, W.L. Vaz, T.E. Thompson, Lateral diffusion in the liquid phases of dimyristoylphosphatidylcholine/cholesterol lipid bilayers: a free volume analysis, *Biochemistry*, 31 (1992) 6739-6747.
- [83] J. Korlach, P. Schwille, W.W. Webb, G.W. Feigenson, Characterization of lipid bilayer phases by confocal microscopy and fluorescence correlation spectroscopy, *P Natl Acad Sci USA*, 96 (1999) 8461-8466.
- [84] G.J. Schutz, G. Kada, V.P. Pastushenko, H. Schindler, Properties of lipid microdomains in a muscle cell membrane visualized by single molecule microscopy, *The EMBO journal*, 19 (2000) 892-901.
- [85] E.D. Sheets, G.M. Lee, R. Simson, K. Jacobson, Transient confinement of a glycosylphosphatidylinositol-anchored protein in the plasma membrane, *Biochemistry*, 36 (1997) 12449-12458.
- [86] A.K. Kenworthy, B.J. Nichols, C.L. Remmert, G.M. Hendrix, M. Kumar, J. Zimmerberg, J. Lippincott-Schwartz, Dynamics of putative raft-associated proteins at the cell surface, *The Journal of cell biology*, 165 (2004) 735-746.
- [87] K. Jacobson, C. Dietrich, Looking at lipid rafts?, *Trends Cell Biol*, 9 (1999) 87-91.
- [88] R.G. Anderson, K. Jacobson, A role for lipid shells in targeting proteins to caveolae, rafts, and other lipid domains, *Science*, 296 (2002) 1821-1825.
- [89] E. Pebay-Peyroula, J.P. Rosenbusch, High-resolution structures and dynamics of membrane protein--lipid complexes: a critique, *Current opinion in structural biology*, 11 (2001) 427-432.
- [90] A. Pralle, P. Keller, E.L. Florin, K. Simons, J.K. Horber, Sphingolipid-cholesterol rafts diffuse as small entities in the plasma membrane of mammalian cells, *The Journal of cell biology*, 148 (2000) 997-1008.
- [91] D. Lingwood, J. Ries, P. Schwille, K. Simons, Plasma membranes are poised for activation of raft phase coalescence at physiological temperature, *P Natl Acad Sci USA*, 105 (2008) 10005-10010.
- [92] D. Lingwood, H.J. Kaiser, I. Levental, K. Simons, Lipid rafts as functional heterogeneity in cell membranes, *Biochemical Society transactions*, 37 (2009) 955-960.
- [93] G.R. Chichili, W. Rodgers, Cytoskeleton-membrane interactions in membrane raft structure, *Cellular and molecular life sciences : CMLS*, 66 (2009) 2319-2328.
- [94] A. Viola, N. Gupta, Tether and trap: regulation of membrane-raft dynamics by actin-binding proteins, *Nature reviews. Immunology*, 7 (2007) 889-896.
- [95] R. Iino, I. Koyama, A. Kusumi, Single molecule imaging of green fluorescent proteins in living cells: E-cadherin forms oligomers on the free cell surface, *Biophys J*, 80 (2001) 2667-2677.

-
- [96] P. Sengupta, A. Hammond, D. Holowka, B. Baird, Structural determinants for partitioning of lipids and proteins between coexisting fluid phases in giant plasma membrane vesicles, *Biochimica et biophysica acta*, 1778 (2008) 20-32.
- [97] P. Legendre, The glycinergic inhibitory synapse, *Cellular and molecular life sciences* : CMLS, 58 (2001) 760-793.
- [98] A.B. Young, S.H. Snyder, Strychnine binding associated with glycine receptors of the central nervous system, *P Natl Acad Sci USA*, 70 (1973) 2832-2836.
- [99] F. Pfeiffer, H. Betz, Solubilization of the glycine receptor from rat spinal cord, *Brain research*, 226 (1981) 273-279.
- [100] D. Graham, F. Pfeiffer, H. Betz, UV light-induced cross-linking of strychnine to the glycine receptor of rat spinal cord membranes, *Biochemical and biophysical research communications*, 102 (1981) 1330-1335.
- [101] R.J. Callister, B.A. Graham, Early history of glycine receptor biology in Mammalian spinal cord circuits, *Front Mol Neurosci*, 3 (2010) 13.
- [102] F. Pfeiffer, D. Graham, H. Betz, Purification by affinity chromatography of the glycine receptor of rat spinal cord, *The Journal of biological chemistry*, 257 (1982) 9389-9393.
- [103] D. Graham, F. Pfeiffer, H. Betz, Photoaffinity-labelling of the glycine receptor of rat spinal cord, *European journal of biochemistry / FEBS*, 131 (1983) 519-525.
- [104] D. Graham, F. Pfeiffer, R. Simler, H. Betz, Purification and characterization of the glycine receptor of pig spinal cord, *Biochemistry*, 24 (1985) 990-994.
- [105] B. Schmitt, P. Knaus, C.M. Becker, H. Betz, The Mr 93,000 polypeptide of the postsynaptic glycine receptor complex is a peripheral membrane protein, *Biochemistry*, 26 (1987) 805-811.
- [106] F. Pfeiffer, R. Simler, G. Grenningloh, H. Betz, Monoclonal antibodies and peptide mapping reveal structural similarities between the subunits of the glycine receptor of rat spinal cord, *P Natl Acad Sci USA*, 81 (1984) 7224-7227.
- [107] A. Triller, F. Cluzeaud, F. Pfeiffer, H. Betz, H. Korn, Distribution of glycine receptors at central synapses: an immunoelectron microscopy study, *The Journal of cell biology*, 101 (1985) 683-688.
- [108] G. Grenningloh, A. Rienitz, B. Schmitt, C. Methfessel, M. Zensen, K. Beyreuther, E.D. Gundelfinger, H. Betz, The strychnine-binding subunit of the glycine receptor shows homology with nicotinic acetylcholine receptors, *Nature*, 328 (1987) 215-220.
- [109] M.O. Ortells, G.G. Lunt, Evolutionary history of the ligand-gated ion-channel superfamily of receptors, *Trends Neurosci*, 18 (1995) 121-127.
- [110] D. Langosch, L. Thomas, H. Betz, Conserved quaternary structure of ligand-gated ion channels: the postsynaptic glycine receptor is a pentamer, *P Natl Acad Sci USA*, 85 (1988) 7394-7398.
- [111] J. Bormann, N. Rundstrom, H. Betz, D. Langosch, Residues within transmembrane segment M2 determine chloride conductance of glycine receptor homo- and hetero-oligomers, *The EMBO journal*, 12 (1993) 3729-3737.
- [112] J. Bormann, O.P. Hamill, B. Sakmann, Mechanism of anion permeation through channels gated by glycine and gamma-aminobutyric acid in
-

- mouse cultured spinal neurones, *The Journal of physiology*, 385 (1987) 243-286.
- [113] A.C. Flint, X. Liu, A.R. Kriegstein, Nonsynaptic glycine receptor activation during early neocortical development, *Neuron*, 20 (1998) 43-53.
- [114] C. Rivera, J. Voipio, J.A. Payne, E. Ruusuvuori, H. Lahtinen, K. Lamsa, U. Pirvola, M. Saarma, K. Kaila, The K⁺/Cl⁻ co-transporter KCC2 renders GABA hyperpolarizing during neuronal maturation, *Nature*, 397 (1999) 251-255.
- [115] N.G. Bowery, T.G. Smart, GABA and glycine as neurotransmitters: a brief history, *British journal of pharmacology*, 147 Suppl 1 (2006) S109-119.
- [116] G. Grenningloh, I. Pribilla, P. Prior, G. Multhaup, K. Beyreuther, O. Taleb, H. Betz, Cloning and expression of the 58 kd beta subunit of the inhibitory glycine receptor, *Neuron*, 4 (1990) 963-970.
- [117] R.J. Harvey, V. Schmieden, A. Von Holst, B. Laube, H. Rohrer, H. Betz, Glycine receptors containing the alpha4 subunit in the embryonic sympathetic nervous system, spinal cord and male genital ridge, *The European journal of neuroscience*, 12 (2000) 994-1001.
- [118] J. Kuhse, C.M. Becker, V. Schmieden, W. Hoch, I. Pribilla, D. Langosch, M.L. Malosio, M. Muntz, H. Betz, Heterogeneity of the inhibitory glycine receptor, *Ann N Y Acad Sci*, 625 (1991) 129-135.
- [119] B. Matzenbach, Y. Maulet, L. Sefton, B. Courtier, P. Avner, J.L. Guenet, H. Betz, Structural analysis of mouse glycine receptor alpha subunit genes. Identification and chromosomal localization of a novel variant, *The Journal of biological chemistry*, 269 (1994) 2607-2612.
- [120] V. Devignot, L. Prado de Carvalho, P. Bregestovski, C. Goblet, A novel glycine receptor alpha Z1 subunit variant in the zebrafish brain, *Neuroscience*, 122 (2003) 449-457.
- [121] J. Simon, H. Wakimoto, N. Fujita, M. Lalande, E.A. Barnard, Analysis of the set of GABA(A) receptor genes in the human genome, *The Journal of biological chemistry*, 279 (2004) 41422-41435.
- [122] J.W. Lynch, Molecular structure and function of the glycine receptor chloride channel, *Physiol. Rev.*, 84 (2004) 1051-1095.
- [123] V. Schmieden, J. Kuhse, H. Betz, Agonist pharmacology of neonatal and adult glycine receptor alpha subunits: identification of amino acid residues involved in taurine activation, *The EMBO journal*, 11 (1992) 2025-2032.
- [124] H. Sontheimer, C.M. Becker, D.B. Pritchett, P.R. Schofield, G. Grenningloh, H. Kettenmann, H. Betz, P.H. Seeburg, Functional chloride channels by mammalian cell expression of rat glycine receptor subunit, *Neuron*, 2 (1989) 1491-1497.
- [125] J. Kuhse, B. Laube, D. Magalei, H. Betz, Assembly of the inhibitory glycine receptor: identification of amino acid sequence motifs governing subunit stoichiometry, *Neuron*, 11 (1993) 1049-1056.
- [126] N. Griffon, C. Buttner, A. Nicke, J. Kuhse, G. Schmalzing, H. Betz, Molecular determinants of glycine receptor subunit assembly, *The EMBO journal*, 18 (1999) 4711-4721.
- [127] M.L. Malosio, B. Marqueze-Pouey, J. Kuhse, H. Betz, Widespread expression of glycine receptor subunit mRNAs in the adult and developing rat brain, *The EMBO journal*, 10 (1991) 2401-2409.

-
- [128] C.M. Becker, W. Hoch, H. Betz, Glycine receptor heterogeneity in rat spinal cord during postnatal development, *The EMBO journal*, 7 (1988) 3717-3726.
- [129] I. Pribilla, T. Takagi, D. Langosch, J. Bormann, H. Betz, The atypical M2 segment of the beta subunit confers picrotoxinin resistance to inhibitory glycine receptor channels, *The EMBO journal*, 11 (1992) 4305-4311.
- [130] V. Burzomato, M. Beato, P.J. Groot-Kormelink, D. Colquhoun, L.G. Sivilotti, Single-channel behavior of heteromeric alpha1beta glycine receptors: an attempt to detect a conformational change before the channel opens, *The Journal of neuroscience : the official journal of the Society for Neuroscience*, 24 (2004) 10924-10940.
- [131] M. Beato, P.J. Groot-Kormelink, D. Colquhoun, L.G. Sivilotti, The activation mechanism of alpha1 homomeric glycine receptors, *The Journal of neuroscience : the official journal of the Society for Neuroscience*, 24 (2004) 895-906.
- [132] J. Grudzinska, R. Schemm, S. Haeger, A. Nicke, G. Schmalzing, H. Betz, B. Laube, The beta subunit determines the ligand binding properties of synaptic glycine receptors, *Neuron*, 45 (2005) 727-739.
- [133] N. Durisic, A.G. Godin, C.M. Wever, C.D. Heyes, M. Lakadamyali, J.A. Dent, Stoichiometry of the human glycine receptor revealed by direct subunit counting, *The Journal of neuroscience : the official journal of the Society for Neuroscience*, 32 (2012) 12915-12920.
- [134] G. Meyer, J. Kirsch, H. Betz, D. Langosch, Identification of a gephyrin binding motif on the glycine receptor beta subunit, *Neuron*, 15 (1995) 563-572.
- [135] J. Kirsch, D. Langosch, P. Prior, U.Z. Littauer, B. Schmitt, H. Betz, The 93-kDa glycine receptor-associated protein binds to tubulin, *The Journal of biological chemistry*, 266 (1991) 22242-22245.
- [136] P. Prior, B. Schmitt, G. Grenningloh, I. Pribilla, G. Multhaup, K. Beyreuther, Y. Maulet, P. Werner, D. Langosch, J. Kirsch, et al., Primary structure and alternative splice variants of gephyrin, a putative glycine receptor-tubulin linker protein, *Neuron*, 8 (1992) 1161-1170.
- [137] A. Dumoulin, A. Triller, M. Kneussel, Cellular transport and membrane dynamics of the glycine receptor, *Frontiers in molecular neuroscience*, 2 (2009) 28.
- [138] J.W. Lynch, Native glycine receptor subtypes and their physiological roles, *Neuropharmacology*, 56 (2009) 303-309.
- [139] C. Hanus, C. Vannier, A. Triller, Intracellular association of glycine receptor with gephyrin increases its plasma membrane accumulation rate, *The Journal of neuroscience : the official journal of the Society for Neuroscience*, 24 (2004) 1119-1128.
- [140] M. Kneussel, Postsynaptic scaffold proteins at non-synaptic sites. The role of postsynaptic scaffold proteins in motor-protein-receptor complexes, *EMBO reports*, 6 (2005) 22-27.
- [141] C. Maas, D. Belgardt, H.K. Lee, F.F. Heisler, C. Lappe-Siefke, M.M. Magiera, J. van Dijk, T.J. Hausrat, C. Janke, M. Kneussel, Synaptic activation modifies microtubules underlying transport of postsynaptic cargo, *P Natl Acad Sci USA*, 106 (2009) 8731-8736.
- [142] C. Maas, N. Tagnaouti, S. Loeblich, B. Behrend, C. Lappe-Siefke, M. Kneussel, Neuronal cotransport of glycine receptor and the scaffold protein gephyrin, *The Journal of cell biology*, 172 (2006) 441-451.
-

Reference list

- [143] P.C. Bridgman, Myosin-dependent transport in neurons, *Journal of neurobiology*, 58 (2004) 164-174.
- [144] C. Buttner, S. Sadtler, A. Leyendecker, B. Laube, N. Griffon, H. Betz, G. Schmalzing, Ubiquitination precedes internalization and proteolytic cleavage of plasma membrane-bound glycine receptors, *The Journal of biological chemistry*, 276 (2001) 42978-42985.
- [145] R. Huang, S. He, Z. Chen, G.H. Dillon, N.J. Leidenheimer, Mechanisms of homomeric alpha1 glycine receptor endocytosis, *Biochemistry*, 46 (2007) 11484-11493.
- [146] M. Rosenberg, J. Meier, A. Triller, C. Vannier, Dynamics of glycine receptor insertion in the neuronal plasma membrane, *The Journal of neuroscience : the official journal of the Society for Neuroscience*, 21 (2001) 5036-5044.
- [147] J. Meier, C. Vannier, A. Serge, A. Triller, D. Choquet, Fast and reversible trapping of surface glycine receptors by gephyrin, *Nat. Neurosci.*, 4 (2001) 253-260.
- [148] J. Kirsch, I. Wolters, A. Triller, H. Betz, Gephyrin antisense oligonucleotides prevent glycine receptor clustering in spinal neurons, *Nature*, 366 (1993) 745-748.
- [149] J. Meier, C. Meunier-Durmort, C. Forest, A. Triller, C. Vannier, Formation of glycine receptor clusters and their accumulation at synapses, *J Cell Sci*, 113 (Pt 15) (2000) 2783-2795.
- [150] M. Dahan, S. Levi, C. Luccardini, P. Rostaing, B. Riveau, A. Triller, Diffusion dynamics of glycine receptors revealed by single-quantum dot tracking, *Science*, 302 (2003) 442-445.
- [151] C. Charrier, M.V. Ehrensperger, M. Dahan, S. Levi, A. Triller, Cytoskeleton regulation of glycine receptor number at synapses and diffusion in the plasma membrane, *J. Neurosci.*, 26 (2006) 8502-8511.
- [152] M.V. Ehrensperger, C. Hanus, C. Vannier, A. Triller, M. Dahan, Multiple association states between glycine receptors and gephyrin identified by SPT analysis, *Biophys. J.*, 92 (2007) 3706-3718.
- [153] K. Gerrow, A. Triller, Synaptic stability and plasticity in a floating world, *Current opinion in neurobiology*, 20 (2010) 631-639.
- [154] T. Dresbach, R. Nawrotzki, T. Kremer, S. Schumacher, D. Quinones, M. Kluska, J. Kuhse, J. Kirsch, Molecular architecture of glycinergic synapses, *Histochem Cell Biol*, 130 (2008) 617-633.
- [155] M. Kneussel, H. Betz, Clustering of inhibitory neurotransmitter receptors at developing postsynaptic sites: the membrane activation model, *Trends Neurosci*, 23 (2000) 429-435.
- [156] C. Deleuze, M. Runquist, H. Orcel, A. Rabie, G. Dayanithi, G. Alonso, N. Hussy, Structural difference between heteromeric somatic and homomeric axonal glycine receptors in the hypothalamo-neurohypophysial system, *Neuroscience*, 135 (2005) 475-483.
- [157] H.J. Jeong, I.S. Jang, A.J. Moorhouse, N. Akaike, Activation of presynaptic glycine receptors facilitates glycine release from presynaptic terminals synapsing onto rat spinal sacral dorsal commissural nucleus neurons, *The Journal of physiology*, 550 (2003) 373-383.
- [158] R. Turecek, L.O. Trussell, Presynaptic glycine receptors enhance transmitter release at a mammalian central synapse, *Nature*, 411 (2001) 587-590.

-
- [159] R. Turecek, L.O. Trussell, Reciprocal developmental regulation of presynaptic ionotropic receptors, *P Natl Acad Sci USA*, 99 (2002) 13884-13889.
- [160] J.H. Ye, F. Wang, K. Krnjevic, W. Wang, Z.G. Xiong, J. Zhang, Presynaptic glycine receptors on GABAergic terminals facilitate discharge of dopaminergic neurons in ventral tegmental area, *The Journal of neuroscience : the official journal of the Society for Neuroscience*, 24 (2004) 8961-8974.
- [161] J. Kuhse, V. Schmieden, H. Betz, Identification and functional expression of a novel ligand binding subunit of the inhibitory glycine receptor, *J. Biol. Chem.*, 265 (1990) 22317-22320.
- [162] J. Dlugaiczyk, W. Singer, B. Schick, H. Iro, K. Becker, C.M. Becker, U. Zimmermann, K. Rohbock, M. Knipper, Expression of glycine receptors and gephyrin in the rat cochlea, *Histochem. Cell. Biol.*, 129 (2008) 513-523.
- [163] R.J. Harvey, U.B. Depner, H. Wassle, S. Ahmadi, C. Heindl, H. Reinold, T.G. Smart, K. Harvey, B. Schutz, O.M. Abo-Salem, A. Zimmer, P. Poisbeau, H. Welzl, D.P. Wolfner, H. Betz, H.U. Zeilhofer, U. Muller, GlyR alpha3: an essential target for spinal PGE2-mediated inflammatory pain sensitization, *Science*, 304 (2004) 884-887.
- [164] S. Haverkamp, U. Muller, K. Harvey, R.J. Harvey, H. Betz, H. Wassle, Diversity of glycine receptors in the mouse retina: localization of the alpha3 subunit, *J. Comp. Neurol.*, 465 (2003) 524-539.
- [165] A.K. Sharma, R.Y. Reams, W.H. Jordan, M.A. Miller, H.L. Thacker, P.W. Snyder, Mesial temporal lobe epilepsy: pathogenesis, induced rodent models and lesions, *Toxicologic pathology*, 35 (2007) 984-999.
- [166] P. Legendre, B. Forstera, R. Juttner, J.C. Meier, Glycine Receptors Caught between Genome and Proteome - Functional Implications of RNA Editing and Splicing, *Front. Mol. Neurosci.*, 2 (2009) 23.
- [167] Z. Nikolic, B. Laube, R.G. Weber, P. Lichter, P. Kioschis, A. Poustka, C. Mulhardt, C.M. Becker, The human glycine receptor subunit alpha3. Glra3 gene structure, chromosomal localization, and functional characterization of alternative transcripts, *J. Biol. Chem.*, 273 (1998) 19708-19714.
- [168] S.A. Eichler, S. Kirischuk, R. Juttner, P.K. Schaefermeier, P. Legendre, T.N. Lehmann, T. Gloveli, R. Grantyn, J.C. Meier, Glycinergic tonic inhibition of hippocampal neurons with depolarizing GABAergic transmission elicits histopathological signs of temporal lobe epilepsy, *J Cell Mol Med*, 12 (2008) 2848-2866.
- [169] J.C. Meier, C. Henneberger, I. Melnick, C. Racca, R.J. Harvey, U. Heinemann, V. Schmieden, R. Grantyn, RNA editing produces glycine receptor alpha3(P185L), resulting in high agonist potency, *Nat Neurosci*, 8 (2005) 736-744.
- [170] S.A. Eichler, B. Forstera, B. Smolinsky, R. Juttner, T.N. Lehmann, M. Fahling, G. Schwarz, P. Legendre, J.C. Meier, Splice-specific roles of glycine receptor alpha3 in the hippocampus, *Eur. J. Neurosci.*, 30 (2009) 1077-1091.
- [171] P. Legendre, E. Muller, C.I. Badiu, J. Meier, C. Vannier, A. Triller, Desensitization of homomeric alpha1 glycine receptor increases with receptor density, *Mol. Pharmacol.*, 62 (2002) 817-827.
-

Reference list

- [172] L. Han, S. Talwar, Q. Wang, Q. Shan, J.W. Lynch, Phosphorylation of alpha3 Glycine Receptors Induces a Conformational Change in the Glycine-Binding Site, *ACS chemical neuroscience*, (2013).
- [173] N. Melzer, C. Villmann, K. Becker, K. Harvey, R.J. Harvey, N. Vogel, C.J. Kluck, M. Kneussel, C.M. Becker, Multifunctional basic motif in the glycine receptor intracellular domain induces subunit-specific sorting, *The Journal of biological chemistry*, 285 (2010) 3730-3739.
- [174] H.G. Breiting, C. Villmann, N. Melzer, J. Rennert, U. Breiting, S. Schwarzinger, C.M. Becker, Novel regulatory site within the TM3-4 loop of human recombinant alpha3 glycine receptors determines channel gating and domain structure, *The Journal of biological chemistry*, 284 (2009) 28624-28633.
- [175] A. Winkelmann, N. Maggio, J. Eller, G. Caliskan, M. Semtner, U. Haussler, R. Juttner, T. Dugladze, B. Smolinsky, S. Kowalczyk, E. Chronowska, G. Schwarz, F.G. Rathjen, G. Rechavi, C.A. Haas, A. Kulik, T. Gloveli, U. Heinemann, J.C. Meier, Changes in neural network homeostasis trigger neuropsychiatric symptoms, *J Clin Invest*, 124 (2014) 696-711.
- [176] G. Patterson, M. Davidson, S. Manley, J. Lippincott-Schwartz, Superresolution imaging using single-molecule localization, *Annual review of physical chemistry*, 61 (2010) 345-367.
- [177] D.M. Jameson, J.C. Croney, P.D. Moens, Fluorescence: basic concepts, practical aspects, and some anecdotes, *Methods Enzymol*, 360 (2003) 1-43.
- [178] M. Sauer, J. Hofkens, J. Enderlein, *Handbook of fluorescence spectroscopy and imaging : from single molecules to ensembles*, Wiley-VCH, Weinheim, 2011.
- [179] G. Cox, *Optical imaging techniques in cell biology*, Taylor & Francis, Boca Raton, Fla. ; London, 2007.
- [180] M. Bruchez, Jr., M. Moronne, P. Gin, S. Weiss, A.P. Alivisatos, Semiconductor nanocrystals as fluorescent biological labels, *Science*, 281 (1998) 2013-2016.
- [181] E. Abbe, Beiträge zur Theorie des Mikroskops und der mikroskopischen Wahrnehmung, *Archiv f. mikrosk. Anatomie*, 9 (1873) 413-418.
- [182] M. Fernandez-Suarez, A.Y. Ting, Fluorescent probes for super-resolution imaging in living cells, *Nat Rev Mol Cell Biol*, 9 (2008) 929-943.
- [183] S.W. Hell, Microscopy and its focal switch, *Nat Methods*, 6 (2009) 24-32.
- [184] C.M. Anderson, G.N. Georgiou, I.E. Morrison, G.V. Stevenson, R.J. Cherry, Tracking of cell surface receptors by fluorescence digital imaging microscopy using a charge-coupled device camera. Low-density lipoprotein and influenza virus receptor mobility at 4 degrees C, *J. Cell. Sci.*, 101 (Pt 2) (1992) 415-425.
- [185] J. Gelles, B.J. Schnapp, M.P. Sheetz, Tracking kinesin-driven movements with nanometre-scale precision, *Nature*, 331 (1988) 450-453.
- [186] G.M. Lee, A. Ishihara, K.A. Jacobson, Direct observation of brownian motion of lipids in a membrane, *P Natl Acad Sci USA*, 88 (1991) 6274-6278.
- [187] H. Deschout, K. Neyts, K. Braeckmans, The influence of movement on the localization precision of sub-resolution particles in fluorescence microscopy, *J Biophotonics*, 5 (2012) 97-109.

-
- [188] M.K. Cheezum, W.F. Walker, W.H. Guilford, Quantitative comparison of algorithms for tracking single fluorescent particles, *Biophys J*, 81 (2001) 2378-2388.
- [189] K.I. Mortensen, L.S. Churchman, J.A. Spudich, H. Flyvbjerg, Optimized localization analysis for single-molecule tracking and super-resolution microscopy, *Nat. Methods*, 7 (2010) 377-381.
- [190] M. Tokunaga, N. Imamoto, K. Sakata-Sogawa, Highly inclined thin illumination enables clear single-molecule imaging in cells, *Nat Methods*, 5 (2008) 159-161.
- [191] D. Axelrod, Total internal reflection fluorescence microscopy in cell biology, *Traffic*, 2 (2001) 764-774.
- [192] S. Wieser, G.J. Schutz, Tracking single molecules in the live cell plasma membrane-Do's and Don't's, *Methods*, 46 (2008) 131-140.
- [193] S. Bonneau, M. Dahan, L.D. Cohen, Single quantum dot tracking based on perceptual grouping using minimal paths in a spatiotemporal volume, *IEEE transactions on image processing : a publication of the IEEE Signal Processing Society*, 14 (2005) 1384-1395.
- [194] H. Qian, M.P. Sheetz, E.L. Elson, Single particle tracking. Analysis of diffusion and flow in two-dimensional systems, *Biophys. J.*, 60 (1991) 910-921.
- [195] G.J. Schutz, H. Schindler, T. Schmidt, Single-molecule microscopy on model membranes reveals anomalous diffusion, *Biophys. J.*, 73 (1997) 1073-1080.
- [196] M.J. Saxton, Single-particle tracking: the distribution of diffusion coefficients, *Biophys. J.*, 72 (1997) 1744-1753.
- [197] M.J. Saxton, Lateral diffusion in an archipelago. Single-particle diffusion, *Biophys J*, 64 (1993) 1766-1780.
- [198] M.J. Saxton, Single-particle tracking: models of directed transport, *Biophys. J.*, 67 (1994) 2110-2119.
- [199] R. Simson, E.D. Sheets, K. Jacobson, Detection of temporary lateral confinement of membrane proteins using single-particle tracking analysis, *Biophys. J.*, 69 (1995) 989-993.
- [200] T.J. Feder, I. BrustMascher, J.P. Slattery, B. Baird, W.W. Webb, Constrained diffusion or immobile fraction on cell surfaces: A new interpretation, *Biophys. J.*, 70 (1996) 2767-2773.
- [201] P.R. Smith, I.E. Morrison, K.M. Wilson, N. Fernandez, R.J. Cherry, Anomalous diffusion of major histocompatibility complex class I molecules on HeLa cells determined by single particle tracking, *Biophys. J.*, 76 (1999) 3331-3344.
- [202] L.C. Elliott, M. Barhoum, J.M. Harris, P.W. Bohn, Trajectory analysis of single molecules exhibiting non-brownian motion, *Phys. Chem. Chem. Phys.*, 13 (2011) 4326-4334.
- [203] S. Wieser, M. Moertelmaier, E. Fuertbauer, H. Stockinger, G.J. Schutz, (Un)confined diffusion of CD59 in the plasma membrane determined by high-resolution single molecule microscopy, *Biophys. J.*, 92 (2007) 3719-3728.
- [204] D. Alcor, G. Gouzer, A. Triller, Single-particle tracking methods for the study of membrane receptors dynamics, *Eur. J. Neurosci.*, 30 (2009) 987-997.
-

- [205] C. Dietrich, B. Yang, T. Fujiwara, A. Kusumi, K. Jacobson, Relationship of lipid rafts to transient confinement zones detected by single particle tracking, *Biophys J*, 82 (2002) 274-284.
- [206] T. Savin, P.S. Doyle, Static and dynamic errors in particle tracking microrheology, *Biophys J*, 88 (2005) 623-638.
- [207] M. Bates, B. Huang, X. Zhuang, Super-resolution microscopy by nanoscale localization of photo-switchable fluorescent probes, *Current opinion in chemical biology*, 12 (2008) 505-514.
- [208] E. Betzig, G.H. Patterson, R. Sougrat, O.W. Lindwasser, S. Olenych, J.S. Bonifacio, M.W. Davidson, J. Lippincott-Schwartz, H.F. Hess, Imaging intracellular fluorescent proteins at nanometer resolution, *Science*, 313 (2006) 1642-1645.
- [209] S.T. Hess, T.P. Girirajan, M.D. Mason, Ultra-high resolution imaging by fluorescence photoactivation localization microscopy, *Biophys. J.*, 91 (2006) 4258-4272.
- [210] M. Heilemann, S. van de Linde, M. Schuttpelz, R. Kasper, B. Seefeldt, A. Mukherjee, P. Tinnefeld, M. Sauer, Subdiffraction-resolution fluorescence imaging with conventional fluorescent probes, *Angew. Chem. Int. Edit. Engl.*, 47 (2008) 6172-6176.
- [211] M.J. Rust, M. Bates, X. Zhuang, Sub-diffraction-limit imaging by stochastic optical reconstruction microscopy (STORM), *Nat Methods*, 3 (2006) 793-795.
- [212] M. Heilemann, P. Dedecker, J. Hofkens, M. Sauer, Photoswitches: Key molecules for subdiffraction-resolution fluorescence imaging and molecular quantification, *Laser Photonics Rev*, 3 (2009) 180-202.
- [213] V. Adam, B. Moeyaert, C.C. David, H. Mizuno, M. Lelimosin, P. Dedecker, R. Ando, A. Miyawaki, J. Michiels, Y. Engelborghs, J. Hofkens, Rational design of photoconvertible and biphotocchromic fluorescent proteins for advanced microscopy applications, *Chemistry & biology*, 18 (2011) 1241-1251.
- [214] H. Mizuno, P. Dedecker, R. Ando, T. Fukano, J. Hofkens, A. Miyawaki, Higher resolution in localization microscopy by slower switching of a photochromic protein, *Photochemical & photobiological sciences : Official journal of the European Photochemistry Association and the European Society for Photobiology*, 9 (2010) 239-248.
- [215] M. Heilemann, S. van de Linde, A. Mukherjee, M. Sauer, Super-Resolution Imaging with Small Organic Fluorophores, *Angew. Chem. Int. Edit. Engl.*, 48 (2009) 6903-6908.
- [216] G.T. Dempsey, J.C. Vaughan, K.H. Chen, M. Bates, X. Zhuang, Evaluation of fluorophores for optimal performance in localization-based super-resolution imaging, *Nat Methods*, 8 (2011) 1027-1036.
- [217] S. van de Linde, A. Loschberger, T. Klein, M. Heidbreder, S. Wolter, M. Heilemann, M. Sauer, Direct stochastic optical reconstruction microscopy with standard fluorescent probes, *Nat. Protoc.*, 6 (2011) 991-1009.
- [218] G.T. Dempsey, M. Bates, W.E. Kowtoniuk, D.R. Liu, R.Y. Tsien, X. Zhuang, Photoswitching mechanism of cyanine dyes, *J Am Chem Soc*, 131 (2009) 18192-18193.
- [219] S. van de Linde, M. Sauer, How to switch a fluorophore: from undesired blinking to controlled photoswitching, *Chemical Society Reviews*, (2014).

-
- [220] R.P. Nieuwenhuizen, K.A. Lidke, M. Bates, D.L. Puig, D. Grunwald, S. Stallinga, B. Rieger, Measuring image resolution in optical nanoscopy, *Nat Methods*, 10 (2013) 557-562.
- [221] F.V. Subach, G.H. Patterson, S. Manley, J.M. Gillette, J. Lippincott-Schwartz, V.V. Verkhusha, Photoactivatable mCherry for high-resolution two-color fluorescence microscopy, *Nat Methods*, 6 (2009) 153-159.
- [222] M. Lehmann, S. Rocha, B. Mangeat, F. Blanchet, I.H. Uji, J. Hofkens, V. Piguet, Quantitative multicolor super-resolution microscopy reveals tetherin HIV-1 interaction, *PLoS Pathog*, 7 (2011) e1002456.
- [223] S. van de Linde, U. Endesfelder, A. Mukherjee, M. Schuttpelz, G. Wiebusch, S. Wolter, M. Heilemann, M. Sauer, Multicolor photoswitching microscopy for subdiffraction-resolution fluorescence imaging, *Photoch. Photobio. Sci.*, 8 (2009) 465-469.
- [224] G. Shtengel, J.A. Galbraith, C.G. Galbraith, J. Lippincott-Schwartz, J.M. Gillette, S. Manley, R. Sougrat, C.M. Waterman, P. Kanchanawong, M.W. Davidson, R.D. Fetter, H.F. Hess, Interferometric fluorescent super-resolution microscopy resolves 3D cellular ultrastructure, *P Natl Acad Sci USA*, 106 (2009) 3125-3130.
- [225] B. Huang, W. Wang, M. Bates, X. Zhuang, Three-dimensional super-resolution imaging by stochastic optical reconstruction microscopy, *Science*, 319 (2008) 810-813.
- [226] M.F. Juette, T.J. Gould, M.D. Lessard, M.J. Mlodzianoski, B.S. Nagpure, B.T. Bennett, S.T. Hess, J. Bewersdorf, Three-dimensional sub-100 nm resolution fluorescence microscopy of thick samples, *Nat Methods*, 5 (2008) 527-529.
- [227] S.J. Sahl, W.E. Moerner, Super-resolution fluorescence imaging with single molecules, *Current opinion in structural biology*, 23 (2013) 778-787.
- [228] C.G. Specht, I. Izeddin, P.C. Rodriguez, M. El Beheiry, P. Rostaing, X. Darzacq, M. Dahan, A. Triller, Quantitative nanoscopy of inhibitory synapses: counting gephyrin molecules and receptor binding sites, *Neuron*, 79 (2013) 308-321.
- [229] K. Xu, G. Zhong, X. Zhuang, Actin, spectrin, and associated proteins form a periodic cytoskeletal structure in axons, *Science*, 339 (2013) 452-456.
- [230] A. Loschberger, S. van de Linde, M.C. Dabauvalle, B. Rieger, M. Heilemann, G. Krohne, M. Sauer, Super-resolution imaging visualizes the eightfold symmetry of gp210 proteins around the nuclear pore complex and resolves the central channel with nanometer resolution, *J Cell Sci*, 125 (2012) 570-575.
- [231] R.G. Parton, J.F. Hancock, Lipid rafts and plasma membrane microorganization: insights from Ras, *Trends Cell Biol*, 14 (2004) 141-147.
- [232] A. Rossi, T.J. Moritz, J. Ratelade, A.S. Verkman, Super-resolution imaging of aquaporin-4 orthogonal arrays of particles in cell membranes, *J Cell Sci*, 125 (2012) 4405-4412.
- [233] P. Sengupta, S. Van Engelenburg, J. Lippincott-Schwartz, Visualizing cell structure and function with point-localization superresolution imaging, *Developmental cell*, 23 (2012) 1092-1102.

- [234] D.M. Owen, C. Rentero, J. Rossy, A. Magenau, D. Williamson, M. Rodriguez, K. Gaus, PALM imaging and cluster analysis of protein heterogeneity at the cell surface, *J. Biophotonics.*, 3 (2010) 446-454.
- [235] R.R. Kellner, C.J. Baier, K.I. Willig, S.W. Hell, F.J. Barrantes, Nanoscale organization of nicotinic acetylcholine receptors revealed by stimulated emission depletion microscopy, *Neuroscience*, 144 (2007) 135-143.
- [236] H. Mizuno, M. Abe, P. Dedecker, A. Makino, S. Rocha, Y. Ohno-Iwashita, J. Hofkens, T. Kobayashi, A. Miyawaki, Fluorescent probes for superresolution imaging of lipid domains on the plasma membrane, *Chem. Sci.*, 2 (2011) 1548-1553.
- [237] D.J. Williamson, D.M. Owen, J. Rossy, A. Magenau, M. Wehrmann, J.J. Gooding, K. Gaus, Pre-existing clusters of the adaptor Lat do not participate in early T cell signaling events, *Nature immunology*, 12 (2011) 655-662.
- [238] B.D. Ripley, *Statistical inference for spatial processes : an essay awarded the Adams Prize of the University of Cambridge*, Cambridge University Press, Cambridge, 1988.
- [239] M.A. Kiskowski, J.F. Hancock, A.K. Kenworthy, On the use of Ripley's K-function and its derivatives to analyze domain size, *Biophys. J.*, 97 (2009) 1095-1103.
- [240] M. Ehrlich, W. Boll, A. van Oijen, R. Hariharan, K. Chandran, M.L. Nibert, T. Kirchhausen, Endocytosis by random initiation and stabilization of clathrin-coated pits, *Cell*, 118 (2004) 591-605.
- [241] B.D. Ripley, *Stochastic geometry and the analysis of spatial patterns*, in, University of Cambridge, [S.I.], 1976.
- [242] P. Annibale, S. Vanni, M. Scarselli, U. Rothlisberger, A. Radenovic, Identification of clustering artifacts in photoactivated localization microscopy, *Nat. Methods*, 8 (2011) 527-528.
- [243] T. Ha, P. Tinnefeld, Photophysics of fluorescent probes for single-molecule biophysics and super-resolution imaging, *Annual review of physical chemistry*, 63 (2012) 595-617.
- [244] P. Sengupta, J. Lippincott-Schwartz, Quantitative analysis of photoactivated localization microscopy (PALM) datasets using pair-correlation analysis, *BioEssays : news and reviews in molecular, cellular and developmental biology*, 34 (2012) 396-405.
- [245] P. Sengupta, T. Jovanovic-Talisman, J. Lippincott-Schwartz, Quantifying spatial organization in point-localization superresolution images using pair correlation analysis, *Nat Protoc*, 8 (2013) 345-354.
- [246] S.L. Veatch, B.B. Machta, S.A. Shelby, E.N. Chiang, D.A. Holowka, B.A. Baird, Correlation functions quantify super-resolution images and estimate apparent clustering due to over-counting, *PLoS one*, 7 (2012) e31457.
- [247] P. Sengupta, T. Jovanovic-Talisman, D. Skoko, M. Renz, S.L. Veatch, J. Lippincott-Schwartz, Probing protein heterogeneity in the plasma membrane using PALM and pair correlation analysis, *Nat Methods*, 8 (2011) 969-975.
- [248] S.L. Veatch, E.N. Chiang, P. Sengupta, D.A. Holowka, B.A. Baird, Quantitative nanoscale analysis of IgE-FcepsilonRI clustering and coupling to early signaling proteins, *The journal of physical chemistry. B*, 116 (2012) 6923-6935.

-
- [249] L. Groc, L. Bard, D. Choquet, Surface trafficking of N-methyl-D-aspartate receptors: physiological and pathological perspectives, *Neuroscience*, 158 (2009) 4-18.
- [250] F.J. Barrantes, Cholesterol effects on nicotinic acetylcholine receptor, *J. Neurochem.*, 103 Suppl 1 (2007) 72-80.
- [251] I. Chung, R. Akita, R. Vandlen, D. Toomre, J. Schlessinger, I. Mellman, Spatial control of EGF receptor activation by reversible dimerization on living cells, *Nature*, 464 (2010) 783-787.
- [252] Z.Q. Xu, X. Zhang, L. Scott, Regulation of G protein-coupled receptor trafficking, *Acta Physiol. (Oxf)*, 190 (2007) 39-45.
- [253] D. Lingwood, K. Simons, Lipid rafts as a membrane-organizing principle, *Science*, 327 (2010) 46-50.
- [254] K. Ritchie, R. Iino, T. Fujiwara, K. Murase, A. Kusumi, The fence and picket structure of the plasma membrane of live cells as revealed by single molecule techniques (Review), *Mol. Membr. Biol.*, 20 (2003) 13-18.
- [255] Y. Sako, A. Kusumi, Compartmentalized structure of the plasma membrane for receptor movements as revealed by a nanometer-level motion analysis, *J. Cell. Biol.*, 125 (1994) 1251-1264.
- [256] C. Bedet, J.C. Bruusgaard, S. Vergo, L. Groth-Pedersen, S. Eimer, A. Triller, C. Vannier, Regulation of gephyrin assembly and glycine receptor synaptic stability, *J. Biol. Chem.*, 281 (2006) 30046-30056.
- [257] J.A. Allen, R.A. Halverson-Tamboli, M.M. Rasenick, Lipid raft microdomains and neurotransmitter signalling, *Nat. Rev. Neurosci.*, 8 (2007) 128-140.
- [258] D. Choquet, Fast AMPAR trafficking for a high-frequency synaptic transmission, *The European journal of neuroscience*, 32 (2010) 250-260.
- [259] H.D. MacGillavry, J.M. Kerr, T.A. Blanpied, Lateral organization of the postsynaptic density, *Mol. Cell. Neurosci.*, 48 (2011) 321-331.
- [260] D. Axelrod, D.E. Koppel, J. Schlessinger, E. Elson, W.W. Webb, Mobility measurement by analysis of fluorescence photobleaching recovery kinetics, *Biophys. J.*, 16 (1976) 1055-1069.
- [261] N. Smisdom, K. Braeckmans, H. Deschout, M. vandeVen, J.-M. Rigo, S.C. De Smedt, M. Ameloot, Fluorescence recovery after photobleaching on the confocal laser-scanning microscope: generalized model without restriction on the size of the photobleached disk, *J. Biomed. Opt.*, 16 (2011) 046021-046028.
- [262] K. Peneva, G. Mihov, F. Nolde, S. Rocha, J. Hotta, K. Braeckmans, J. Hofkens, H. Uji-i, A. Herrmann, K. Mullen, Water-soluble monofunctional perylene and terrylene dyes: powerful labels for single-enzyme tracking, *Angew. Chem. Int. Edit. Engl.*, 47 (2008) 3372-3375.
- [263] S. Rocha, J.A. Hutchison, K. Peneva, A. Herrmann, K. Mullen, M. Skjot, C.I. Jorgensen, A. Svendsen, F.C. De Schryver, J. Hofkens, H. Uji-i, Linking phospholipase mobility to activity by single-molecule wide-field microscopy, *Chemphyschem*, 10 (2009) 151-161.
- [264] Q. Tang, M. Edidin, Lowering the barriers to random walks on the cell surface, *Biophys. J.*, 84 (2003) 400-407.
- [265] S.W. Paddock, Confocal laser scanning microscopy, *BioTechniques*, 27 (1999) 992-996, 998-1002, 1004.
- [266] W.B. Amos, J.G. White, How the confocal laser scanning microscope entered biological research, *Biol. Cell.*, 95 (2003) 335-342.
-

- [267] N.L. Thompson, J.K. Pero, Total Internal Reflection Fluorescence Microscopy: Applications in Biophysics, in: M. Hof, R. Hutterer, V. Fidler (Eds.) Fluorescence Spectroscopy in Biology, vol. 3, Springer Berlin Heidelberg, 2005, pp. 79-103.
- [268] S.M. Simon, Partial internal reflections on total internal reflection fluorescent microscopy, *Trends Cell. Biol.*, 19 (2009) 661-668.
- [269] N.O. Petersen, P.L. Hoddellius, P.W. Wiseman, O. Seger, K.E. Magnusson, Quantitation of membrane receptor distributions by image correlation spectroscopy: concept and application, *Biophys. J.*, 65 (1993) 1135-1146.
- [270] P.W. Wiseman, N.O. Petersen, Image correlation spectroscopy. II. Optimization for ultrasensitive detection of preexisting platelet-derived growth factor-beta receptor oligomers on intact cells, *Biophys. J.*, 76 (1999) 963-977.
- [271] C.M. Brown, R.B. Dalal, B. Hebert, M.A. Digman, A.R. Horwitz, E. Gratton, Raster image correlation spectroscopy (RICS) for measuring fast protein dynamics and concentrations with a commercial laser scanning confocal microscope, *J. Microsc.*, 229 (2008) 78-91.
- [272] M.J. Rossow, J.M. Sasaki, M.A. Digman, E. Gratton, Raster image correlation spectroscopy in live cells, *Nat. Protoc.*, 5 (2010) 1761-1774.
- [273] D.L. Kolin, S. Costantino, P.W. Wiseman, Sampling effects, noise, and photobleaching in temporal image correlation spectroscopy, *Biophys. J.*, 90 (2006) 628-639.
- [274] J. Sankaran, M. Manna, L. Guo, R. Kraut, T. Wohland, Diffusion, transport, and cell membrane organization investigated by imaging fluorescence cross-correlation spectroscopy, *Biophys. J.*, 97 (2009) 2630-2639.
- [275] C. Flors, J. Hotta, H. Uji-i, P. Dedecker, R. Ando, H. Mizuno, A. Miyawaki, J. Hofkens, A stroboscopic approach for fast photoactivation-localization microscopy with Dronpa mutants, *J. Am. Chem. Soc.*, 129 (2007) 13970-13977.
- [276] M.B. Roeffaers, G. De Cremer, J. Libeert, R. Ameloot, P. Dedecker, A.J. Bons, M. Buckins, J.A. Martens, B.F. Sels, D.E. De Vos, J. Hofkens, Super-resolution reactivity mapping of nanostructured catalyst particles, *Angew. Chem. Int. Edit. Engl.*, 48 (2009) 9285-9289.
- [277] M.J. Rust, M. Bates, X.W. Zhuang, Sub-diffraction-limit imaging by stochastic optical reconstruction microscopy (STORM), *Nat. Methods*, 3 (2006) 793-795.
- [278] S. van de Linde, I. Krstic, T. Prisner, S. Doose, M. Heilemann, M. Sauer, Photoinduced formation of reversible dye radicals and their impact on super-resolution imaging, *Photoch. Photobio. Sci.*, 10 (2011) 499-506.
- [279] R.E. Thompson, D.R. Larson, W.W. Webb, Precise nanometer localization analysis for individual fluorescent probes, *Biophys. J.*, 82 (2002) 2775-2783.
- [280] B.D. Ripley, 2nd-Order Analysis of Stationary Point Processes, *J. Appl. Probab.*, 13 (1976) 255-266.
- [281] B.D. Ripley, Modeling Spatial Patterns, *J Roy Stat Soc B Met*, 39 (1977) 172-212.
- [282] R.D. Phair, S.A. Gorski, T. Misteli, Measurement of dynamic protein binding to chromatin in vivo, using photobleaching microscopy, *Methods. Enzymol.*, 375 (2004) 393-414.

-
- [283] R.D. Phair, T. Misteli, High mobility of proteins in the mammalian cell nucleus, *Nature*, 404 (2000) 604-609.
- [284] K. Braeckmans, L. Peeters, N.N. Sanders, S.C. De Smedt, J. Demeester, Three-dimensional fluorescence recovery after photobleaching with the confocal scanning laser microscope, *Biophys. J.*, 85 (2003) 2240-2252.
- [285] E. Gielen, N. Smisdom, M. vandeVen, B. De Clercq, E. Gratton, M. Digman, J.M. Rigo, J. Hofkens, Y. Engelborghs, M. Ameloot, Measuring Diffusion of Lipid-like Probes in Artificial and Natural Membranes by Raster Image Correlation Spectroscopy (RICS): Use of a Commercial Laser-Scanning Microscope with Analog Detection, *Langmuir*, 25 (2009) 5209-5218.
- [286] J. Sankaran, X. Shi, L.Y. Ho, E.H. Stelzer, T. Wohland, ImFCS: a software for imaging FCS data analysis and visualization, *Opt. Express*, 18 (2010) 25468-25481.
- [287] T.Y. Kim, H. Uji-i, M. Moller, B. Muls, J. Hofkens, U. Alexiev, Monitoring the interaction of a single G-protein key binding site with rhodopsin disk membranes upon light activation, *Biochemistry*, 48 (2009) 3801-3803.
- [288] N. Unwin, Refined structure of the nicotinic acetylcholine receptor at 4A resolution, *J. Mol. Biol.*, 346 (2005) 967-989.
- [289] J. Kistler, R.M. Stroud, M.W. Klymkowsky, R.A. Lalancette, R.H. Fairclough, Structure and function of an acetylcholine receptor, *Biophys. J.*, 37 (1982) 371-383.
- [290] J.F. Nagle, Long tail kinetics in biophysics?, *Biophys. J.*, 63 (1992) 366-370.
- [291] D.E. Wolf, Designing, building, and using a fluorescence recovery after photobleaching instrument, *Methods. Cell. Biol.*, 30 (1989) 271-306.
- [292] M.A. Digman, C.M. Brown, P. Sengupta, P.W. Wiseman, A.R. Horwitz, E. Gratton, Measuring fast dynamics in solutions and cells with a laser scanning microscope, *Biophys. J.*, 89 (2005) 1317-1327.
- [293] E. Gielen, N. Smisdom, B. De Clercq, M. Vandeven, R. Gijssbers, Z. Debyser, J.M. Rigo, J. Hofkens, Y. Engelborghs, M. Ameloot, Diffusion of myelin oligodendrocyte glycoprotein in living OLN-93 cells investigated by raster-scanning image correlation spectroscopy (RICS), *J. Fluoresc.*, 18 (2008) 813-819.
- [294] M.J. Saxton, Single-particle tracking: effects of corrals, *Biophys. J.*, 69 (1995) 389-398.
- [295] K.M. Wilson, I.E. Morrison, P.R. Smith, N. Fernandez, R.J. Cherry, Single particle tracking of cell-surface HLA-DR molecules using R-phycoerythrin labeled monoclonal antibodies and fluorescence digital imaging, *J Cell Sci*, 109 (Pt 8) (1996) 2101-2109.
- [296] P. Thomas, T.G. Smart, HEK293 cell line: a vehicle for the expression of recombinant proteins, *J. Pharmacol. Toxicol. Methods.*, 51 (2005) 187-200.
- [297] M.D. Ehlers, M. Heine, L. Groc, M.C. Lee, D. Choquet, Diffusional trapping of GluR1 AMPA receptors by input-specific synaptic activity, *Neuron*, 54 (2007) 447-460.
- [298] H.G. Breiting, C.M. Becker, The inhibitory glycine receptor-simple views of a complicated channel, *ChemBiochem : a European journal of chemical biology*, 3 (2002) 1042-1052.

- [299] K. Burger, G. Gimpl, F. Fahrenholz, Regulation of receptor function by cholesterol, *Cellular and molecular life sciences : CMLS*, 57 (2000) 1577-1592.
- [300] R. Willmann, S. Pun, L. Stallmach, G. Sadasivam, A.F. Santos, P. Caroni, C. Fuhrer, Cholesterol and lipid microdomains stabilize the postsynapse at the neuromuscular junction, *The EMBO journal*, 25 (2006) 4050-4060.
- [301] S. Schroder, W. Hoch, C.M. Becker, G. Grenningloh, H. Betz, Mapping of antigenic epitopes on the alpha 1 subunit of the inhibitory glycine receptor, *Biochemistry*, 30 (1991) 42-47.
- [302] U. Grunert, H. Wassle, Immunocytochemical Localization of Glycine Receptors in the Mammalian Retina, *Journal of Comparative Neurology*, 335 (1993) 523-537.
- [303] Z.Q. Xu, X. Zhang, L. Scott, Regulation of G protein-coupled receptor trafficking, *Acta Physiol (Oxf)*, 190 (2007) 39-45.
- [304] J. Fantini, F.J. Barrantes, How cholesterol interacts with membrane proteins: an exploration of cholesterol-binding sites including CRAC, CARC, and tilted domains, *Frontiers in physiology*, 4 (2013) 31.
- [305] M.J. Saxton, Wanted: a positive control for anomalous subdiffusion, *Biophys J*, 103 (2012) 2411-2422.
- [306] P.R. Smith, I.E. Morrison, K.M. Wilson, N. Fernandez, R.J. Cherry, Anomalous diffusion of major histocompatibility complex class I molecules on HeLa cells determined by single particle tracking, *Biophysical journal*, 76 (1999) 3331-3344.
- [307] P.H. Lommerse, G.A. Blab, L. Cognet, G.S. Harms, B.E. Snaar-Jagalska, H.P. Spaank, T. Schmidt, Single-molecule imaging of the H-ras membrane-anchor reveals domains in the cytoplasmic leaflet of the cell membrane, *Biophysical journal*, 86 (2004) 609-616.
- [308] M.J. Saxton, K. Jacobson, Single-particle tracking: applications to membrane dynamics, *Annu. Rev. Biophys. Biomol. Struct.*, 26 (1997) 373-399.
- [309] F. Daumas, N. Destainville, C. Millot, A. Lopez, D. Dean, L. Salome, Interprotein interactions are responsible for the confined diffusion of a G-protein-coupled receptor at the cell surface, *Biochemical Society transactions*, 31 (2003) 1001-1005.
- [310] P.W. Wiseman, C.M. Brown, D.J. Webb, B. Hebert, N.L. Johnson, J.A. Squier, M.H. Ellisman, A.F. Horwitz, Spatial mapping of integrin interactions and dynamics during cell migration by image correlation microscopy, *J Cell Sci*, 117 (2004) 5521-5534.
- [311] C. Eggeling, C. Ringemann, R. Medda, G. Schwarzmann, K. Sandhoff, S. Polyakova, V.N. Belov, B. Hein, C. von Middendorff, A. Schonle, S.W. Hell, Direct observation of the nanoscale dynamics of membrane lipids in a living cell, *Nature*, 457 (2009) 1159-1162.
- [312] T. Schmidt, G.J. Schutz, W. Baumgartner, H.J. Gruber, H. Schindler, Imaging of single molecule diffusion, *Proc. Natl. Acad. Sci. U. S. A.*, 93 (1996) 2926-2929.
- [313] M. Heidbreder, C. Zander, S. Malkusch, D. Widera, B. Kaltschmidt, C. Kaltschmidt, D. Nair, D. Choquet, J.B. Sibarita, M. Heilemann, TNF-alpha influences the lateral dynamics of TNF receptor I in living cells, *Biochimica et biophysica acta*, 1823 (2012) 1984-1989.

-
- [314] S. Wieser, M. Axmann, G.J. Schutz, Versatile analysis of single-molecule tracking data by comprehensive testing against Monte Carlo simulations, *Biophys J*, 95 (2008) 5988-6001.
- [315] A. Serge, N. Bertaux, H. Rigneault, D. Marguet, Dynamic multiple-target tracing to probe spatiotemporal cartography of cell membranes, *Nat Methods*, 5 (2008) 687-694.
- [316] A. Triller, D. Choquet, New concepts in synaptic biology derived from single-molecule imaging, *Neuron*, 59 (2008) 359-374.
- [317] J.H. Kim, R.L. Huganir, Organization and regulation of proteins at synapses, *Current opinion in cell biology*, 11 (1999) 248-254.
- [318] A.J. Borgdorff, D. Choquet, Regulation of AMPA receptor lateral movements, *Nature*, 417 (2002) 649-653.
- [319] J. Kirsch, G. Meyer, H. Betz, Synaptic Targeting of Ionotropic Neurotransmitter Receptors, *Mol Cell Neurosci*, 8 (1996) 93-98.
- [320] H.D. MacGillavry, J.M. Kerr, T.A. Blanpied, Lateral organization of the postsynaptic density, *Molecular and cellular neurosciences*, 48 (2011) 321-331.
- [321] B. Zuber, N. Unwin, Structure and superorganization of acetylcholine receptor-rapsyn complexes, *P Natl Acad Sci USA*, 110 (2013) 10622-10627.
- [322] A. Triller, D. Choquet, Surface trafficking of receptors between synaptic and extrasynaptic membranes: and yet they do move!, *Trends Neurosci*, 28 (2005) 133-139.
- [323] J.W. Lynch, S. Rajendra, K.D. Pierce, C.A. Handford, P.H. Barry, P.R. Schofield, Identification of intracellular and extracellular domains mediating signal transduction in the inhibitory glycine receptor chloride channel, *The EMBO journal*, 16 (1997) 110-120.
- [324] K. Notelaers, N. Smisdom, S. Rocha, D. Janssen, J.C. Meier, J.-M. Rigo, J. Hofkens, M. Ameloot, Ensemble and single particle fluorimetric techniques in concerted action to study the diffusion and aggregation of the glycine receptor $\alpha 3$ isoforms in the cell plasma membrane, *Biochimica et Biophysica Acta (BBA) - Biomembranes*, 1818 (2012) 3131-3140.
- [325] N. Meilhac, L. Le Guyader, L. Salome, N. Destainville, Detection of confinement and jumps in single-molecule membrane trajectories, *Physical review. E, Statistical, nonlinear, and soft matter physics*, 73 (2006) 011915.
- [326] R. Simson, E.D. Sheets, K. Jacobson, Detection of temporary lateral confinement of membrane proteins using single-particle tracking analysis, *Biophysical journal*, 69 (1995) 989-993.
- [327] G.J. Schutz, H. Schindler, T. Schmidt, Single-molecule microscopy on model membranes reveals anomalous diffusion, *Biophysical journal*, 73 (1997) 1073-1080.
- [328] L.C. Elliott, M. Barhoum, J.M. Harris, P.W. Bohn, Trajectory analysis of single molecules exhibiting non-brownian motion, *Physical chemistry chemical physics : PCCP*, 13 (2011) 4326-4334.
- [329] J. Meier, R. Grantyn, A gephyrin-related mechanism restraining glycine receptor anchoring at GABAergic synapses, *The Journal of neuroscience : the official journal of the Society for Neuroscience*, 24 (2004) 1398-1405.
-

Reference list

- [330] R. Bluem, E. Schmidt, C. Corvey, M. Karas, A. Schlicksupp, J. Kirsch, J. Kuhse, Components of the translational machinery are associated with juvenile glycine receptors and are redistributed to the cytoskeleton upon aging and synaptic activity, *The Journal of biological chemistry*, 282 (2007) 37783-37793.
- [331] U. Schmidt, M. Weiss, Anomalous diffusion of oligomerized transmembrane proteins, *The Journal of chemical physics*, 134 (2011) 165101.
- [332] I. Kim, W. Pan, S.A. Jones, Y. Zhang, X. Zhuang, D. Wu, Clathrin and AP2 are required for PtdIns(4,5)P₂-mediated formation of LRP6 signalosomes, *The Journal of cell biology*, 200 (2013) 419-428.
- [333] E.M. Petrini, J. Lu, L. Cognet, B. Lounis, M.D. Ehlers, D. Choquet, Endocytic trafficking and recycling maintain a pool of mobile surface AMPA receptors required for synaptic potentiation, *Neuron*, 63 (2009) 92-105.
- [334] F.J. Barrantes, Cholesterol effects on nicotinic acetylcholine receptor, *Journal of neurochemistry*, 103 Suppl 1 (2007) 72-80.
- [335] E.M. Petrini, I. Marchionni, P. Zacchi, W. Sieghart, E. Cherubini, Clustering of extrasynaptic GABA(A) receptors modulates tonic inhibition in cultured hippocampal neurons, *The Journal of biological chemistry*, 279 (2004) 45833-45843.
- [336] P.Y. Law, L.J. Erickson, R. El-Kouhen, L. Dicker, J. Solberg, W. Wang, E. Miller, A.L. Burd, H.H. Loh, Receptor density and recycling affect the rate of agonist-induced desensitization of mu-opioid receptor, *Mol Pharmacol*, 58 (2000) 388-398.
- [337] C. Bouzigues, M. Dahan, Transient directed motions of GABA(A) receptors in growth cones detected by a speed correlation index, *Biophys J*, 92 (2007) 654-660.
- [338] N. Hirokawa, R. Takemura, Molecular motors and mechanisms of directional transport in neurons, *Nature reviews. Neuroscience*, 6 (2005) 201-214.
- [339] J.E. Lochner, M. Kingma, S. Kuhn, C.D. Meliza, B. Cutler, B.A. Scalettar, Real-time imaging of the axonal transport of granules containing a tissue plasminogen activator/green fluorescent protein hybrid, *Molecular biology of the cell*, 9 (1998) 2463-2476.
- [340] S.M. Simon, Partial internal reflections on total internal reflection fluorescent microscopy, *Trends in cell biology*, 19 (2009) 661-668.
- [341] A.V. Vieira, C. Lamaze, S.L. Schmid, Control of EGF receptor signaling by clathrin-mediated endocytosis, *Science*, 274 (1996) 2086-2089.
- [342] S. Felder, K. Miller, G. Moehren, A. Ullrich, J. Schlessinger, C.R. Hopkins, Kinase activity controls the sorting of the epidermal growth factor receptor within the multivesicular body, *Cell*, 61 (1990) 623-634.
- [343] S. Chi, H. Cao, Y. Wang, M.A. McNiven, Recycling of the epidermal growth factor receptor is mediated by a novel form of the clathrin adaptor protein Eps15, *The Journal of biological chemistry*, 286 (2011) 35196-35208.
- [344] E.M. van Dam, W. Stoorvogel, Dynamin-dependent transferrin receptor recycling by endosome-derived clathrin-coated vesicles, *Molecular biology of the cell*, 13 (2002) 169-182.
- [345] F. Huang, A. Khvorova, W. Marshall, A. Sorkin, Analysis of clathrin-mediated endocytosis of epidermal growth factor receptor by RNA

- interference, *The Journal of biological chemistry*, 279 (2004) 16657-16661.
- [346] R. Le Borgne, B. Hoflack, Mechanisms of protein sorting and coat assembly: insights from the clathrin-coated vesicle pathway, *Current opinion in cell biology*, 10 (1998) 499-503.
- [347] D. Loeke, M. Mettlen, D. Yarar, K. Jaqaman, H. Jaqaman, G. Danuser, S.L. Schmid, Cargo and dynamin regulate clathrin-coated pit maturation, *PLoS biology*, 7 (2009) e57.
- [348] A.C. Magalhaes, K.D. Holmes, L.B. Dale, L. Comps-Agrar, D. Lee, P.N. Yadav, L. Drysdale, M.O. Poulter, B.L. Roth, J.P. Pin, H. Anisman, S.S. Ferguson, CRF receptor 1 regulates anxiety behavior via sensitization of 5-HT₂ receptor signaling, *Nat Neurosci*, 13 (2010) 622-629.
- [349] G.M. Di Guglielmo, C. Le Roy, A.F. Goodfellow, J.L. Wrana, Distinct endocytic pathways regulate TGF-beta receptor signalling and turnover, *Nature cell biology*, 5 (2003) 410-421.
- [350] Z.Y. Chen, A. Ieraci, M. Tanowitz, F.S. Lee, A novel endocytic recycling signal distinguishes biological responses of Trk neurotrophin receptors, *Molecular biology of the cell*, 16 (2005) 5761-5772.
- [351] S.T. Hess, T.P. Girirajan, M.D. Mason, Ultra-high resolution imaging by fluorescence photoactivation localization microscopy, *Biophysical journal*, 91 (2006) 4258-4272.
- [352] S.W. Hell, J. Wichmann, Breaking the diffraction resolution limit by stimulated emission: stimulated-emission-depletion fluorescence microscopy, *Optics letters*, 19 (1994) 780-782.
- [353] M.G. Gustafsson, Surpassing the lateral resolution limit by a factor of two using structured illumination microscopy, *J Microsc-Oxford*, 198 (2000) 82-87.
- [354] R. Heintzmann, C. Cremer, Laterally modulated excitation microscopy: Improvement of resolution by using a diffraction grating, *P Soc Photo-Opt Ins*, 3568 (1999) 185-196.
- [355] X. Zhuang, Nano-imaging with Storm, *Nature photonics*, 3 (2009) 365-367.
- [356] T. Dertinger, R. Colyer, R. Vogel, M. Heilemann, M. Sauer, J. Enderlein, S. Weiss, Superresolution optical fluctuation imaging (SOFI), *Advances in experimental medicine and biology*, 733 (2012) 17-21.
- [357] P. Dedecker, G.C. Mo, T. Dertinger, J. Zhang, Widely accessible method for superresolution fluorescence imaging of living systems, *P Natl Acad Sci USA*, 109 (2012) 10909-10914.
- [358] C. Cremer, B.R. Masters, Resolution enhancement techniques in microscopy, *Eur Phys J H*, 38 (2013) 281-344.
- [359] S. Rocha, H. De Keersmaecker, I.H. Uji, J. Hofkens, H. Mizuno, Photoswitchable fluorescent proteins for superresolution fluorescence microscopy circumventing the diffraction limit of light, *Methods Mol Biol*, 1076 (2014) 793-812.
- [360] M. Heilemann, D.P. Herten, R. Heintzmann, C. Cremer, C. Muller, P. Tinnefeld, K.D. Weston, J. Wolfrum, M. Sauer, High-resolution colocalization of single dye molecules by fluorescence lifetime imaging microscopy, *Analytical chemistry*, 74 (2002) 3511-3517.
- [361] E. Betzig, Proposed Method for Molecular Optical Imaging, *Optics letters*, 20 (1995) 237-239.

Reference list

- [362] A.M. van Oijen, J. Kohler, J. Schmidt, M. Muller, G.J. Brakenhoff, 3-Dimensional super-resolution by spectrally selective imaging, *Chem Phys Lett*, 292 (1998) 183-187.
- [363] H. Bornfleth, K. Satzler, R. Eils, C. Cremer, High-precision distance measurements and volume-conserving segmentation of objects near and below the resolution limit in three-dimensional confocal fluorescence microscopy, *J Microsc-Oxford*, 189 (1998) 118-136.
- [364] H. Bock, C. Geisler, C.A. Wurm, C. Von Middendorff, S. Jakobs, A. Schonle, A. Egner, S.W. Hell, C. Eggeling, Two-color far-field fluorescence nanoscopy based on photoswitchable emitters, *Appl Phys B-Lasers O*, 88 (2007) 161-165.
- [365] P. Lemmer, M. Gunkel, Y. Weiland, P. Muller, D. Baddeley, R. Kaufmann, A. Urich, H. Eipel, R. Amberger, M. Hausmann, C. Cremer, Using conventional fluorescent markers for far-field fluorescence localization nanoscopy allows resolution in the 10-nm range, *J Microsc-Oxford*, 235 (2009) 163-171.
- [366] A. Pertsinidis, K. Mukherjee, M. Sharma, Z.P.P. Pang, S.R. Park, Y.X. Zhang, A.T. Brunger, T.C. Sudhof, S. Chu, Ultrahigh-resolution imaging reveals formation of neuronal SNARE/Munc18 complexes in situ, *P Natl Acad Sci USA*, 110 (2013) E2812-E2820.
- [367] T. Klein, S. van de Linde, M. Sauer, Live-Cell Super-Resolution Imaging Goes Multicolor, *Chembiochem : a European journal of chemical biology*, 13 (2012) 1861-1863.
- [368] R. Kaufmann, P. Muller, G. Hildenbrand, M. Hausmann, C. Cremer, Analysis of Her2/neu membrane protein clusters in different types of breast cancer cells using localization microscopy, *J Microsc-Oxford*, 242 (2011) 46-54.
- [369] M. Brunstein, K. Wicker, K. Heraldt, R. Heintzmann, M. Oheim, Full-field dual-color 100-nm super-resolution imaging reveals organization and dynamics of mitochondrial and ER networks, *Opt. Express*, 21 (2013) 26162-26173.
- [370] L.S. Churchman, Z. Okten, R.S. Rock, J.F. Dawson, J.A. Spudich, Single molecule high-resolution colocalization of Cy3 and Cy5 attached to macromolecules measures intramolecular distances through time, *P Natl Acad Sci USA*, 102 (2005) 1419-1423.
- [371] L.J. Pike, Lipid rafts: bringing order to chaos, *Journal of lipid research*, 44 (2003) 655-667.
- [372] R.G. Parton, A.A. Richards, Lipid rafts and caveolae as portals for endocytosis: new insights and common mechanisms, *Traffic*, 4 (2003) 724-738.
- [373] Z. Truan, L.T. Diez, C. Bonsch, S. Malkusch, U. Endesfelder, M. Munteanu, O. Hartley, M. Heilemann, A. Furstenberg, Quantitative morphological analysis of arrestin2 clustering upon G protein-coupled receptor stimulation by super-resolution microscopy, *J Struct Biol*, 184 (2013) 329-334.
- [374] J. Wong, D. Baddeley, E.A. Bushong, Z.Y. Yu, M.H. Ellisman, M. Hoshijima, C. Soeller, Nanoscale Distribution of Ryanodine Receptors and Caveolin-3 in Mouse Ventricular Myocytes: Dilatation of T-Tubules near Junctions, *Biophys J*, 104 (2013) L22-L24.
- [375] M. Scarselli, P. Annibale, C. Gerace, A. Radenovic, Enlightening G-protein-coupled receptors on the plasma membrane using super-

- resolution photoactivated localization microscopy, *Biochemical Society transactions*, 41 (2013) 191-196.
- [376] O. Huber, A. Brunner, P. Maier, R. Kaufmann, P.O. Couraud, C. Cremer, G. Fricker, Localization Microscopy (SPDM) Reveals Clustered Formations of P-Glycoprotein in a Human Blood-Brain Barrier Model, *PLoS one*, 7 (2012).
- [377] K.A. Gabor, C.R. Stevens, M.J. Pietraszewski, T.J. Gould, J. Shim, J.A. Yoder, S.H. Lam, Z.Y. Gong, S.T. Hess, C.H. Kim, Super Resolution Microscopy Reveals that Caveolin-1 Is Required for Spatial Organization of CRFB1 and Subsequent Antiviral Signaling in Zebrafish, *PLoS one*, 8 (2013).
- [378] J. Meier, The enigma of transmitter-selective receptor accumulation at developing inhibitory synapses, *Cell and tissue research*, 311 (2003) 271-276.
- [379] L. Danglot, P. Rostaing, A. Triller, A. Bessis, Morphologically identified glycinergic synapses in the hippocampus, *Mol Cell Neurosci*, 27 (2004) 394-403.
- [380] C. Bedet, J.C. Bruusgaard, S. Vergo, L. Groth-Pedersen, S. Eimer, A. Triller, C. Vannier, Regulation of gephyrin assembly and glycine receptor synaptic stability, *The Journal of biological chemistry*, 281 (2006) 30046-30056.
- [381] C.A. Haselwandter, M. Calamai, M. Kardar, A. Triller, R.A. da Silveira, Formation and stability of synaptic receptor domains, *Physical review letters*, 106 (2011) 238104.
- [382] R. Turecek, L.O. Trussell, Control of synaptic depression by glutamate transporters, *The Journal of neuroscience : the official journal of the Society for Neuroscience*, 20 (2000) 2054-2063.
- [383] E. Sherman, V. Barr, S. Manley, G. Patterson, L. Balagopalan, I. Akpan, C.K. Regan, R.K. Merrill, C.L. Sommers, J. Lippincott-Schwartz, L.E. Samelson, Functional nanoscale organization of signaling molecules downstream of the T cell antigen receptor, *Immunity*, 35 (2011) 705-720.
- [384] S. van de Linde, S. Wolter, M. Heilemann, M. Sauer, The effect of photoswitching kinetics and labeling densities on super-resolution fluorescence imaging, *Journal of biotechnology*, 149 (2010) 260-266.
- [385] F. Weltzien, C. Puller, G.A. O'Sullivan, I. Paarmann, H. Betz, Distribution of the glycine receptor beta-subunit in the mouse CNS as revealed by a novel monoclonal antibody, *J Comp Neurol*, 520 (2012) 3962-3981.
- [386] M. Mukhtarov, O. Markova, E. Real, Y. Jacob, S. Buldakova, P. Bregestovski, Monitoring of chloride and activity of glycine receptor channels using genetically encoded fluorescent sensors, *Philosophical transactions. Series A, Mathematical, physical, and engineering sciences*, 366 (2008) 3445-3462.
- [387] P. Annibale, S. Vanni, M. Scarselli, U. Rothlisberger, A. Radenovic, Quantitative photo activated localization microscopy: unraveling the effects of photoblinking, *PLoS one*, 6 (2011) e22678.
- [388] K. Notelaers, S. Rocha, R. Paesen, N. Smisdom, B. De Clercq, J.C. Meier, J.-M. Rigo, J. Hofkens, M. Ameloot, Analysis of $\alpha 3$ GlyR single particle tracking in the cell membrane, *Biochimica et Biophysica Acta (BBA) - Molecular Cell Research*, 1843 (2014) 544-553.

Reference list

- [389] B.M. Williams, M.K. Temburni, M.S. Levey, S. Bertrand, D. Bertrand, M.H. Jacob, The long internal loop of the alpha 3 subunit targets nAChRs to subdomains within individual synapses on neurons in vivo, *Nat Neurosci*, 1 (1998) 557-562.
- [390] J. Nymann-Andersen, H. Wang, L. Chen, J.T. Kittler, S.J. Moss, R.W. Olsen, Subunit specificity and interaction domain between GABA(A) receptor-associated protein (GABARAP) and GABA(A) receptors, *J Neurochem*, 80 (2002) 815-823.
- [391] J. Nymann-Andersen, G.W. Sawyer, R.W. Olsen, Interaction between GABAA receptor subunit intracellular loops: implications for higher order complex formation, *J Neurochem*, 83 (2002) 1164-1171.
- [392] J. Oshikawa, Y. Toya, T. Fujita, M. Egawa, J. Kawabe, S. Umemura, Y. Ishikawa, Nicotinic acetylcholine receptor alpha 7 regulates cAMP signal within lipid rafts, *American journal of physiology. Cell physiology*, 285 (2003) C567-574.
- [393] D. Zhu, W.C. Xiong, L. Mei, Lipid rafts serve as a signaling platform for nicotinic acetylcholine receptor clustering, *The Journal of neuroscience : the official journal of the Society for Neuroscience*, 26 (2006) 4841-4851.
- [394] L.J. Pike, The challenge of lipid rafts, *Journal of lipid research*, 50 Suppl (2009) S323-328.
- [395] K. Notelaers, S. Rocha, R. Paesen, N. Swinnen, J. Vangindertael, J. Meier, J.-M. Rigo, M. Ameloot, J. Hofkens, Membrane distribution of the glycine receptor $\alpha 3$ studied by optical super-resolution microscopy, *Histochem. Cell. Biol.*, (2014) 1-12.
- [396] L. Salome, J.L. Cazeils, A. Lopez, J.F. Tocanne, Characterization of membrane domains by FRAP experiments at variable observation areas, *European biophysics journal : EBJ*, 27 (1998) 391-402.
- [397] L. Wawrezynieck, H. Rigneault, D. Marguet, P.F. Lenne, Fluorescence correlation spectroscopy diffusion laws to probe the submicron cell membrane organization, *Biophys J*, 89 (2005) 4029-4042.
- [398] B. De Clercq, B. Cleuren, H. Deschout, K. Braeckmans, M. Ameloot, Distinguishing free and anomalous diffusion by rectangular fluorescence recovery after photobleaching: a Monte Carlo study, *J Biomed Opt*, 18 (2013) 76012.
- [399] D. Marguet, P.F. Lenne, H. Rigneault, H.T. He, Dynamics in the plasma membrane: how to combine fluidity and order, *The EMBO journal*, 25 (2006) 3446-3457.
- [400] S. Schoch, E.D. Gundelfinger, Molecular organization of the presynaptic active zone, *Cell and tissue research*, 326 (2006) 379-391.
- [401] S. Okabe, Molecular anatomy of the postsynaptic density, *Mol Cell Neurosci*, 34 (2007) 503-518.
- [402] A. Peters, S.L. Palay, H.d. Webster, *The fine structure of the nervous system : neurons and their supporting cells*, 3rd ed. ed., OUP, New York, 1991.
- [403] X. Chen, C.A. Winters, T.S. Reese, Life inside a thin section: tomography, *The Journal of neuroscience : the official journal of the Society for Neuroscience*, 28 (2008) 9321-9327.
- [404] C.A. Diebold, A.J. Koster, R.I. Koning, Pushing the resolution limits in cryo electron tomography of biological structures, *J Microsc-Oxford*, 248 (2012) 1-5.

-
- [405] A. Dani, B. Huang, J. Bergan, C. Dulac, X. Zhuang, Superresolution imaging of chemical synapses in the brain, *Neuron*, 68 (2010) 843-856.
- [406] M. Maglione, S.J. Sigrist, Seeing the forest tree by tree: super-resolution light microscopy meets the neurosciences, *Nat Neurosci*, 16 (2013) 790-797.
- [407] U.V. Nagerl, K.I. Willig, B. Hein, S.W. Hell, T. Bonhoeffer, Live-cell imaging of dendritic spines by STED microscopy, *P Natl Acad Sci USA*, 105 (2008) 18982-18987.
- [408] S. Beyenburg, A.J. Mitchell, D. Schmidt, C.E. Elger, M. Reuber, Anxiety in patients with epilepsy: systematic review and suggestions for clinical management, *Epilepsy & behavior : E&B*, 7 (2005) 161-171.
- [409] D. Nair, E. Hosity, J.D. Petersen, A. Constals, G. Giannone, D. Choquet, J.B. Sibarita, Super-resolution imaging reveals that AMPA receptors inside synapses are dynamically organized in nanodomains regulated by PSD95, *The Journal of neuroscience : the official journal of the Society for Neuroscience*, 33 (2013) 13204-13224.
- [410] N. Hoze, D. Nair, E. Hosity, C. Sieben, S. Manley, A. Herrmann, J.B. Sibarita, D. Choquet, D. Holcman, Heterogeneity of AMPA receptor trafficking and molecular interactions revealed by superresolution analysis of live cell imaging, *P Natl Acad Sci USA*, 109 (2012) 17052-17057.
- [411] S.H. Shim, C. Xia, G. Zhong, H.P. Babcock, J.C. Vaughan, B. Huang, X. Wang, C. Xu, G.Q. Bi, X. Zhuang, Super-resolution fluorescence imaging of organelles in live cells with photoswitchable membrane probes, *P Natl Acad Sci USA*, 109 (2012) 13978-13983.
- [412] S.A. Jones, S.H. Shim, J. He, X. Zhuang, Fast, three-dimensional super-resolution imaging of live cells, *Nat Methods*, 8 (2011) 499-508.
- [413] S. Manley, J.M. Gillette, G.H. Patterson, H. Shroff, H.F. Hess, E. Betzig, J. Lippincott-Schwartz, High-density mapping of single-molecule trajectories with photoactivated localization microscopy, *Nat Methods*, 5 (2008) 155-157.
- [414] C. Tardin, L. Cognet, C. Bats, B. Lounis, D. Choquet, Direct imaging of lateral movements of AMPA receptors inside synapses, *The EMBO journal*, 22 (2003) 4656-4665.
- [415] S. Levi, C. Schweizer, H. Bannai, O. Pascual, C. Charrier, A. Triller, Homeostatic regulation of synaptic GlyR numbers driven by lateral diffusion, *Neuron*, 59 (2008) 261-273.
- [416] H. Bannai, S. Levi, C. Schweizer, T. Inoue, T. Launey, V. Racine, J.B. Sibarita, K. Mikoshiba, A. Triller, Activity-dependent tuning of inhibitory neurotransmission based on GABAAR diffusion dynamics, *Neuron*, 62 (2009) 670-682.
- [417] H. Bannai, S. Levi, C. Schweizer, M. Dahan, A. Triller, Imaging the lateral diffusion of membrane molecules with quantum dots, *Nat Protoc*, 1 (2006) 2628-2634.
- [418] D. Choquet, A. Triller, The role of receptor diffusion in the organization of the postsynaptic membrane, *Nature reviews. Neuroscience*, 4 (2003) 251-265.
- [419] C. Espenel, E. Margeat, P. Dosset, C. Arduise, C. Le Grimmellec, C.A. Royer, C. Boucheix, E. Rubinstein, P.E. Milhiet, Single-molecule analysis of CD9 dynamics and partitioning reveals multiple modes of interaction in the tetraspanin web, *J. Cell. Biol.*, 182 (2008) 765-776.
-

Reference list

- [420] Z. Xiao, W. Zhang, Y. Yang, L. Xu, X. Fang, Single-molecule diffusion study of activated EGFR implicates its endocytic pathway, *Biochemical and biophysical research communications*, 369 (2008) 730-734.
- [421] Y. Chen, B. Yang, K. Jacobson, Transient confinement zones: a type of lipid raft?, *Lipids*, 39 (2004) 1115-1119.
- [422] R. Simson, B. Yang, S.E. Moore, P. Doherty, F.S. Walsh, K.A. Jacobson, Structural mosaicism on the submicron scale in the plasma membrane, *Biophys J*, 74 (1998) 297-308.
- [423] M.J. Saxton, Anomalous diffusion due to obstacles: a Monte Carlo study, *Biophys J*, 66 (1994) 394-401.
- [424] H. Hering, C.C. Lin, M. Sheng, Lipid rafts in the maintenance of synapses, dendritic spines, and surface AMPA receptor stability, *The Journal of neuroscience : the official journal of the Society for Neuroscience*, 23 (2003) 3262-3271.
- [425] A. Kusumi, K. Suzuki, Toward understanding the dynamics of membrane-raft-based molecular interactions, *Biochimica et biophysica acta*, 1746 (2005) 234-251.
- [426] L. Rajendran, K. Simons, Lipid rafts and membrane dynamics, *J. Cell. Sci.*, 118 (2005) 1099-1102.
- [427] C. Le Roy, J.L. Wrana, Clathrin- and non-clathrin-mediated endocytic regulation of cell signalling, *Nat Rev Mol Cell Bio*, 6 (2005) 112-126.
- [428] B. Nichols, Caveosomes and endocytosis of lipid rafts, *J. Cell. Sci.*, 116 (2003) 4707-4714.
- [429] F. Daumas, N. Destainville, C. Millot, A. Lopez, D. Dean, L. Salome, Confined diffusion without fences of a g-protein-coupled receptor as revealed by single particle tracking, *Biophys J*, 84 (2003) 356-366.
- [430] L. Cezanne, S. Lecat, B. Lagane, C. Millot, J.Y. Vollmer, H. Matthes, J.L. Galzi, A. Lopez, Dynamic confinement of NK2 receptors in the plasma membrane - Improved frap analysis and biological relevance, *J. Biol. Chem.*, 279 (2004) 45057-45067.
- [431] A.V. Weigel, M.M. Tamkun, D. Krapf, Quantifying the dynamic interactions between a clathrin-coated pit and cargo molecules, *Proc. Natl. Acad. Sci. U. S. A.*, 110 (2013) E4591-E4600.
- [432] T. Kirchhausen, Imaging endocytic clathrin structures in living cells, *Trends Cell Biol*, 19 (2009) 596-605.
- [433] H. Betz, B. Laube, Glycine receptors: recent insights into their structural organization and functional diversity, *J Neurochem*, 97 (2006) 1600-1610.
- [434] B.T. Kelly, A.J. McCoy, K. Spate, S.E. Miller, P.R. Evans, S. Honing, D.J. Owen, A structural explanation for the binding of endocytic dileucine motifs by the AP2 complex, *Nature*, 456 (2008) 976-979.
- [435] T. Suzuki, J. Zhang, S. Miyazawa, Q. Liu, M.R. Farzan, W.D. Yao, Association of membrane rafts and postsynaptic density: proteomics, biochemical, and ultrastructural analyses, *J Neurochem*, 119 (2011) 64-77.
- [436] B. Zonta, L. Minichiello, Synaptic membrane rafts: traffic lights for local neurotrophin signaling?, *Frontiers in synaptic neuroscience*, 5 (2013) 9.
- [437] L.S. Borges, S. Yechikhov, Y.I. Lee, J.B. Rudell, M.B. Friese, S.J. Burden, M.J. Ferns, Identification of a motif in the acetylcholine receptor beta subunit whose phosphorylation regulates rapsyn association and

- postsynaptic receptor localization, *The Journal of neuroscience : the official journal of the Society for Neuroscience*, 28 (2008) 11468-11476.
- [438] E.O. Vik-Mo, L. Oltedal, E.A. Hoivik, H. Kleivdal, J. Eidet, S. Davanger, Sec6 is localized to the plasma membrane of mature synaptic terminals and is transported with secretogranin II-containing vesicles, *Neuroscience*, 119 (2003) 73-85.
- [439] E. Macia, M. Ehrlich, R. Massol, E. Boucrot, C. Brunner, T. Kirchhausen, Dynasore, a cell-permeable inhibitor of dynamin, *Developmental cell*, 10 (2006) 839-850.
- [440] D.A. Richards, S.O. Rizzoli, W.J. Betz, Effects of wortmannin and latrunculin A on slow endocytosis at the frog neuromuscular junction, *The Journal of physiology*, 557 (2004) 77-91.
- [441] M. Edidin, The state of lipid rafts: from model membranes to cells, *Annu Rev Biophys Biomol Struct*, 32 (2003) 257-283.
- [442] R. Zidovetzki, I. Levitan, Use of cyclodextrins to manipulate plasma membrane cholesterol content: evidence, misconceptions and control strategies, *Biochimica et biophysica acta*, 1768 (2007) 1311-1324.
- [443] D. Weihs, T.G. Mason, M.A. Teitell, Effects of cytoskeletal disruption on transport, structure, and rheology within mammalian cells, *Phys Fluids* (1994), 19 (2007) 103102.
- [444] B. Goetze, B. Grunewald, S. Baldassa, M. Kiebler, Chemically controlled formation of a DNA/calcium phosphate coprecipitate: application for transfection of mature hippocampal neurons, *Journal of neurobiology*, 60 (2004) 517-525.
- [445] P. Washbourne, A.K. McAllister, Techniques for gene transfer into neurons, *Current opinion in neurobiology*, 12 (2002) 566-573.
- [446] S. Kaech, G. Banker, Culturing hippocampal neurons, *Nat Protoc*, 1 (2006) 2406-2415.
- [447] S. Vira, E. Mekhedov, G. Humphrey, P.S. Blank, Fluorescent-labeled antibodies: Balancing functionality and degree of labeling, *Analytical biochemistry*, 402 (2010) 146-150.
- [448] M.S. Zhang, H. Chang, Y.D. Zhang, J.W. Yu, L.J. Wu, W. Ji, J.J. Chen, B. Liu, J.Z. Lu, Y.F. Liu, J.L. Zhang, P.Y. Xu, T. Xu, Rational design of true monomeric and bright photoactivatable fluorescent proteins, *Nat. Methods*, 9 (2012) 727-U297.
- [449] B. David-Watine, S.L. Shorte, S. Fucile, D. de Saint Jan, H. Korn, P. Bregestovski, Functional integrity of green fluorescent protein conjugated glycine receptor channels, *Neuropharmacology*, 38 (1999) 785-792.
- [450] T. Waseem, M. Mukhtarov, S. Buldakova, I. Medina, P. Bregestovski, Genetically encoded Cl-Sensor as a tool for monitoring of Cl-dependent processes in small neuronal compartments, *Journal of neuroscience methods*, 193 (2010) 14-23.
- [451] S. Wolter, M. Schuttpelz, M. Tscherepanow, V.D.L. S, M. Heilemann, M. Sauer, Real-time computation of subdiffraction-resolution fluorescence images, *J Microsc-Oxford*, 237 (2010) 12-22.
- [452] K. Jaqaman, D. Loerke, M. Mettlen, H. Kuwata, S. Grinstein, S.L. Schmid, G. Danuser, Robust single-particle tracking in live-cell time-lapse sequences, *Nat Methods*, 5 (2008) 695-702.

Reference list

- [453] S.J. Holden, S. Uphoff, A.N. Kapanidis, DAOSTORM: an algorithm for high- density super-resolution microscopy, *Nat Methods*, 8 (2011) 279-280.
- [454] F. Huang, S.L. Schwartz, J.M. Byars, K.A. Lidke, Simultaneous multiple-emitter fitting for single molecule super-resolution imaging, *Biomedical optics express*, 2 (2011) 1377-1393.
- [455] M. Roding, H. Deschout, T. Martens, K. Notelaers, J. Hofkens, M. Ameloot, K. Braeckmans, A. Sarkka, M. Rudemo, Automatic particle detection in microscopy using temporal correlations, *Microscopy research and technique*, 76 (2013) 997-1006.
- [456] S. Cox, E. Rosten, J. Monypenny, T. Jovanovic-Talisman, D.T. Burnette, J. Lippincott-Schwartz, G.E. Jones, R. Heintzmann, Bayesian localization microscopy reveals nanoscale podosome dynamics, *Nat Methods*, 9 (2012) 195-200.
- [457] N. Monnier, S.M. Guo, M. Mori, J. He, P. Lenart, M. Bathe, Bayesian approach to MSD-based analysis of particle motion in live cells, *Biophys J*, 103 (2012) 616-626.
- [458] D.J. Rolfe, C.I. McLachlan, M. Hirsch, S.R. Needham, C.J. Tynan, S.E. Webb, M.L. Martin-Fernandez, M.P. Hobson, Automated multidimensional single molecule fluorescence microscopy feature detection and tracking, *European biophysics journal : EBJ*, 40 (2011) 1167-1186.
- [459] J.W. Yoon, A. Bruckbauer, W.J. Fitzgerald, D. Klenerman, Bayesian inference for improved single molecule fluorescence tracking, *Biophys J*, 94 (2008) 4932-4947.
- [460] H. Babcock, Y. Sigal, X. Zhuang, A high-density 3D localization algorithm for stochastic optical reconstruction microscopy, *Opt Nano*, 1 (2012) 1-10.
- [461] H.P. Kao, A.S. Verkman, Tracking of single fluorescent particles in three dimensions: use of cylindrical optics to encode particle position, *Biophys J*, 67 (1994) 1291-1300.
- [462] L. Holtzer, T. Meckel, T. Schmidt, Nanometric three-dimensional tracking of individual quantum dots in cells, *Appl Phys Lett*, 90 (2007).
- [463] D.M. Owen, D.J. Williamson, L. Boelen, A. Magenau, J. Rossy, K. Gaus, Quantitative analysis of three-dimensional fluorescence localization microscopy data, *Biophys J*, 105 (2013) L05-07.
- [464] S. van de Linde, M. Heilemann, M. Sauer, Live-cell super-resolution imaging with synthetic fluorophores, *Annual review of physical chemistry*, 63 (2012) 519-540.
- [465] P. Sengupta, S.B. van Engelenburg, J. Lippincott-Schwartz, Superresolution Imaging of Biological Systems Using Photoactivated Localization Microscopy, *Chemical reviews*, (2014).
- [466] D.M. Owen, A. Magenau, D.J. Williamson, K. Gaus, Super-resolution imaging by localization microscopy, *Methods Mol Biol*, 950 (2013) 81-93.
- [467] T. Klein, A. Loschberger, S. Proppert, S. Wolter, S. van de Linde, M. Sauer, Live-cell dSTORM with SNAP-tag fusion proteins, *Nat Methods*, 8 (2011) 7-9.
- [468] R. Wombacher, M. Heidbreder, S. van de Linde, M.P. Sheetz, M. Heilemann, V.W. Cornish, M. Sauer, Live-cell super-resolution imaging with trimethoprim conjugates, *Nat Methods*, 7 (2010) 717-719.

Nederlandse samenvatting

Membraaneiwwitten zijn mobiel in het vlak van het celmembraan en ondergaan een Brownse beweging. Gezien de stochastische aard van deze beweging verwacht men een willekeurige diffusie en verdeling van eiwwitten in het membraan. Voor veel membraaneiwwitten is dit echter niet het geval, omdat er membraangerelateerde interactieprocessen zijn die interfereren. Deze processen vormen vaak een essentieel onderdeel van de fysiologische signalisatie, zoals het clusteren van neurotransmitterreceptoren in de synaptische membraan ter bevordering van de neurontransmissie. Een van de populaties van neurotransmitterreceptoren zijn de ligandgeactiveerde ionkanalen, verantwoordelijk voor het koppelen van een chemisch signaal naar een elektrische puls. Zo zorgt binding van glycine op de glycinereceptor (GlyR) voor een verhoogde permeabilisatie van de membraan voor negatief geladen chloorionen. Er bestaan meerdere vormen van de GlyR, waaronder de $\alpha 3$ -vorm. Deze vorm is het meest gekend om zijn rol in pijnsignalisatie, maar is ook betrokken bij de pathofysiologie van epilepsie.

Bij temporale-kwab-epilepsie is er een rol vastgesteld voor extrasynaptische $\alpha 3$ -GlyR, waarbij de membraankarakteristieken van de receptor een mogelijke rol spelen. Het doel van dit onderzoek is om de diffusie en de verdeling van de $\alpha 3$ -GlyR in kaart te brengen. Hierbij wordt de hypothese gesteld dat optische nanoscopie een meerwaarde kan leveren. Deze hypothese is gebaseerd op de observatieschaal van nanoscopie, die dichter aanleunt bij de effectieve afmetingen van de betrokken eiwwitten. Zowel voor het bestuderen van de diffusie als de verdeling werd gekozen voor het visualiseren van de $\alpha 3$ -GlyR door middel van immunolabeling met fluorescente antilichamen.

Voor het bepalen van de membraandiffusie van de receptor werd 'single particle tracking' (SPT) toegepast en voor het bepalen van de ruimtelijke verdeling van de $\alpha 3$ -GlyR 'direct Stochastic Optical Reconstruction Microscopy' (dSTORM). In beide gevallen werd de nanoscopie oorspronkelijk parallel uitgevoerd met microfluorimetrische bepalingen (**hoofdstuk 2**). Vergelijking van de resultaten illustreerde de complementaire aard van nano- en microscopische metingen, maar benadrukte ook de aanwezigheid van submicroscopische fenomenen die buiten het directe observatiebereik liggen van microfluorimetrische bepalingen. Deze fenomenen werden verder onderzocht door middel van een uitgebreide analyse van de nanoscopische observaties. Zo werden er, met betrekking tot

diffusie, significante afwijkingen gevonden van de willekeurige beweging van $\alpha 3$ -GlyR in het membraan (**hoofdstuk 3**). Anderzijds vertoonde de $\alpha 3$ -GlyR ook een niet-willekeurige membraan verdeling, weerspiegeld in de aanwezigheid van clustering met verschillende dichtheden (**hoofdstuk 4**). De parameters gebonden aan de afwijkende diffusie en clustering werden gekwantificeerd en in verband gebracht met gekende biologische interactieprocessen (**hoofdstuk 3, 4, 5**). Zo wordt het nut van optische nanoscopie in de biologie beklemtoond en kunnen nieuwe doelen voor toekomstig onderzoek worden gesteld.

Curriculum Vitae

Kristof Notelaers werd geboren op 19 september 1986 te Bilzen. In 2004 behaalde hij zijn diploma Algemeen Secundair Onderwijs (ASO) in de studierichting wetenschappen-wiskunde aan het Heilig-Grafinstituut te Bilzen. In datzelfde jaar begon hij zijn studies aan de Universiteit Hasselt/transnationale Universiteit Limburg (tUL) waar hij in 2009 met grote onderscheiding afstudeerde als master in de Biomedische Wetenschappen. Zijn eindwerk getiteld "Glycine enhances microglial calcium fluxes: A possible role for neutral amino acid transporters" voerde hij uit in het lab van Prof. dr. Jean-Michel Rigo. In februari 2010 ging hij van start met zijn doctoraat aan het Biomedisch Onderzoeksinstituut van de Universiteit Hasselt en het departement Chemie Afdeling Moleculaire Visualisatie en Fotonica aan de KULeuven. Tijdens deze periode nam hij deel aan verschillende opdrachten en cursussen gekaderd binnen de Doctoral School for Medicine and Life Sciences en de Leuven Arenberg Doctoral School. De resultaten bekomen tijdens zijn doctoraat werden gepubliceerd in internationale tijdschriften en gepresenteerd op (inter)nationale congressen.

Bibliography

Publications

- **Notelaers K**, Rocha S, Paesen R, Smisdom N, Swinnen N, Vangindertael J, Meier JC, Rigo JM, Ameloot M, Hofkens J. *Membrane distribution of the glycine receptor $\alpha 3$ studied by optical super-resolution microscopy. Histochem Cell Biol.* 2014 Feb 20. [Epub ahead of print]
- **Notelaers K**, Rocha S, Paesen R, Smisdom N, De Clercq B, Meier JC, Rigo JM, Hofkens J, Ameloot M. *Analysis of $\alpha 3$ GlyR single particle tracking in the cell membrane. Biochim Biophys Acta.* 2013 Dec 4;1843(3):544-553.
- Rödning M, Deschout H, Martens T, **Notelaers K**, Hofkens J, Ameloot M, Braeckmans K, Särkkä A, Rudemo M. *Automatic particle detection in microscopy using temporal correlations. Microsc Res Tech.* 2013 Oct;76(10):997-1006.
- Swinnen N, Smolders S, Avila A, **Notelaers K**, Paesen R, Ameloot M, Brône B, Legendre P*, Rigo JM*. (* contributed equally) *Complex invasion pattern of the cerebral cortex by microglial cells during development of the mouse embryo. Glia.* 2013 Feb;61(2):150-63.
- **Notelaers K***, Smisdom N*, Rocha S, Janssen D, Meier JC, Rigo JM, Hofkens J, Ameloot M. *Ensemble and single particle fluorimetric techniques in concerted action to study the diffusion and aggregation of the glycine receptor $\alpha 3$ isoforms in the cell plasma membrane. Biochim Biophys Acta, Biomembranes.* 2012 Dec;1818(12):3131-40. *Equally contributing first authors
- Van den Eynden J, **Notelaers K**, Brône B, Janssen D, Nelissen K, Sahebali S, Smolders I, Hellings N, Steels P, Rigo JM. *Glycine enhances microglial intracellular calcium signaling. A role for sodium-coupled neutral amino acid transporters. Pflugers Arch.* 2011 Apr;461(4):481-91.

Selected oral presentations

Dynamics and organization of $\alpha 3$ -containing glycine receptors using single molecule detection

K Notelaers, S Rocha, JC Meier, JM Rigo, J Hofkens, M Ameloot

- BBS, Young Scientist Day (2011), *Ghent, Belgium*
- Joint autumn meeting BSCDB-BSM (2011), *Antwerp, Belgium*
- European Light Microscopy Initiative Meeting (2012), *Leuven, Belgium*

Selected poster presentations

Diffusion and clustering of the glycine receptor $\alpha 3$ in the plasma membrane

K Notelaers, N Smisdom, S Rocha, D Janssen, JC Meier, Jean-Michel Rigo, J Hofkens, M Ameloot

- Advanced Light Microscopy Symposium (2010), *Ghent, Belgium*

Dynamics and organization of the glycine receptor $\alpha 3$ using single molecule detection

K Notelaers, N Smisdom, S Rocha, D Janssen, JC Meier, Jean-Michel Rigo, J Hofkens, M Ameloot

- 14th EURON PhD Days (2010), *Diepenbeek, Belgium*
- Annual Dutch meeting on molecular and cellular biophysics (2012), *Veldhoven, The Netherlands*
- M.G. memorial symposium on high resolution microscopy (2012), *Ashburn, VA, The United States of America*
- ICREA international symposium (2013), *Barcelona, Spain*
- ICP 2013 (2013), *Leuven, Belgium*

Grants

Lasers for Science access to the Functional Biosystems Imaging facility at the Rutherford Appleton Laboratory, Harwell Science and Innovation Campus, Didcot, UK

Dankwoord

Graag wil ik beginnen met het erkennen van de instellingen, die het mij mogelijk gemaakt hebben om de gepresenteerde doctoraatsstudie uit te voeren: de Universiteit Hasselt, transnationale Universiteit Limburg en de Katholieke Universiteit Leuven. Ik heb deze opportuniteit te danken aan de "cross-fertilization" tussen de biofysicagroep van BIOMED aan de UHasselt en het departement Chemie afdeling Moleculaire Visualisatie en Fotonica van de KULeuven. Hiervoor wil ik de promotoren van deze samenwerking, professor Marcel Ameloot en professor Johan Hofkens, bedanken. Verder dank ik ook volgende professoren voor hun input bij de vormgeving van de wetenschappelijk inhoud: Jean-Michel Rigo, Bert Brône, Hideaki Mizuno en Jochen Meier. Bovendien ben ik hen allen ook dankbaar voor hun rol in mijn doctoraatsjury, net als professor Luc Michiels, professor Thomas Gensch en professor Frans Ramaekers. Jullie adviezen zijn steeds goed ontvangen en hebben de kwaliteit van het werk versterkt.

De bidiplomering bracht naast een leerrijke ervaring veel papierwerk met zich mee. Toch werd er steeds de nodige flexibiliteit geboden in de afhandeling hiervan. Ik wil hierbij zeker de mensen van de UHasselt en Arenberg doctoral schools vermelden, met name: Stefanie Kerkhofs, Kim Pannemans, Natalie Ghys, Leen Cuypers en Indra Hautekiet. Certificaten en handtekeningen, het was me wat! Verder ook een pluim voor de mensen van de GLW facultaire administratieve dienst. Er is op korte tijd veel veranderd in de administratie, toch waren raad en daad nooit veraf. In het lab kon ik dan weer rekenen op de praktische ondersteuning van Jo Janssen, Rosette Beenaerts en Petra Bex. Ook de bewakers van het natuurkundelab René Liberloo, Rik Lempens en Michel De Roeve wil ik bedanken voor me wegwijs te maken en de toffe praat tijdens de lunch. Verder bedank ik ook de mensen van XOD en de centrale administratieve dienst voor de hulp bij het drukken van de thesis.

Door de interdisciplinaire aard van mijn onderzoek ben ik in contact gekomen met veel verschillende onderzoeksgroepen. Het is niet altijd even evident geweest om iedereen op één lijn te trekken en ik wil alvast al mijn collega's bedanken voor hun geduld. Het begon allemaal zeer klein in de toenmalige, all male, biofysica groep. Nick Smisdom en Ben De Clercq als de ervaren doctoraatsstudenten en Marcel als professor. Ik voelde me een beetje zoals d'Artagnan die zich aansluit bij de drie musketiers. Af en toe eens de degens

kruisen, maar uiteindelijk één voor allen en allen voor één. De biofysica groep kende nadien een snelle expansie met Rik Paesen, Kathleen Sanen, Sarah Deville, Rozhin Penjweini, Hannelore Bové en Eli Slenders. Vanuit het buitenland kwamen ook Mihaela Bacalum en Daniel Hadraba om ons team te verrijken. Naast een nieuwe dimensie van wetenschappelijke samenwerking, werd ook het concept biofysica teambuilding leven in geblazen. Niet altijd even gemakkelijk om te organiseren, maar wel stevast een plezierige bezigheid. Ik hoop verder dat iedereen van de biofysica groep iets heeft kunnen leren uit ons contact, daarom niet noodzakelijk op de labmeetings. Voor mij is ons reilen en zeilen een zeer leerrijke ervaring geweest, waarvoor bedankt. Ik wil ook graag al de studenten die onder mijn begeleiding hebben gestaan bedanken. Hierbij een speciale knipooq naar Sarah Deville, die nu zelf een gedreven doctoraatsstudente van de biofysica groep is.

Naast de mensen van biofysica, heb ik ook met de leden van de fysiologiegroep graag samengewerkt. Ik bedank jullie voor de ondersteuning bij het patchen en voor de verwittigingen bij het arriveren van de crèmekar! Ik hoop ook dat jullie nog veel plezier beleven aan de confocale en niet teveel mysterieuze haperingen tegenkomen. Voorts bedank ik alle collega's van BIOMED, voor de lach en de traan die we gedeeld hebben. Ik wil Veronique Pousset nog veel sterkte wensen bij het ondersteunen van de afleggende doctoraatsstudenten.

Buiten BIOMED zijn er ook veel mensen die ik wil bedanken. Niet in het minst mijn collega's van de afdeling moleculaire visualisatie en fotonica. Jullie weten hoe een feestje moet gebouwd worden! Susana, je was mijn mentor in de nanoscopie en mijn helpende hand voor het papierwerk. Jouw inspirerende woorden en golden touch aan de microscoop hebben me dikwijls moed gegeven. Ik bedank je uit de grond van mijn hart en ik wens je nog veel succes met je carrière en je gezin. Aan Jeroen Vangindertael wens ik de moed en volharding om zijn doctoraat en occasioneel dieet af te ronden. Bedankt om voor me klaar te staan als de opstelling moeilijk deed. Op mijn buitenlandse excursies heb ik ook veel mensen leren kennen die ik bij deze wil bedanken. Van 's ochtend rennen op het strand van Arcachon tot gin tonic en tapas 's nachts in Barcelona. Stuk voor stuk geweldige ervaringen die ik voor het leven zal meedragen. Ohja, jullie posters en presentaties waren ook geweldig!

Het kan natuurlijk niet altijd werk zijn waar het om draait. De steun van familie en vrienden gaat veel verder dan dat. Wat ik precies bestudeerd heb zullen jullie misschien nooit weten, maar dat ik het niet zonder jullie had kunnen doen staat vast. Bedankt aan de mannen van de volleybal, ik heb op het veld dikwijls kunnen ventileren. Bedankt aan de mannen van Diest en omstreken, op stap gaan en van het leven genieten deed deugd. Alle internet- en gamingvrienden, de skillz die jullie me leerden zijn nog steeds nuttig. Thx!!! Mijn twee grote families wil ik bedanken voor hun interesse en de geborgenheid. Jullie samenkomst op ons trouwfeest was een memorabel en heugelijk moment. Meter en Peter, bedankt voor de babbels en het advies tijdens mijn bezoeken. Els en Dries, ik kan het niet neerschrijven, maar jullie weten dat onze band voor altijd is. Mijn geweldige schoonfamilie wil ik ook bedanken, voor mij op te nemen in hun kring. Met plezier kijk ik steeds uit naar onze samenkomsten, een moment om even alle zorgen te laten varen en te genieten van het leven.

De laatste paragraaf is opgedragen aan de mensen die het meeste met mij hebben afgezien. Te beginnen bij mijn ouderlijk gezinnetje. Onze matriarch oftewel ons Bonneke, die altijd klaarstond voor mij. De jaren hebben hun tol geëist, maar die grote jong is erg trots om jou als oma te hebben. Ma en Pa, jullie hebben altijd klaargestaan voor mij met een luisterend oor, raad en daad. De kinderen vliegen uit, maar het ouderlijke nest blijft nog steeds een warme en gezellige plaats. Duizendmaal bedankt voor alles, van bakjes troost tot bakjes chinees. Zussemus en Lodewijk, jullie beginnen zelf een nieuw hoofdstuk. Bedankt voor alle steun en leuke activiteiten, van quizzen tot race against nature. Sofie, het is een hele eer om je broer te zijn en ik zal altijd naar je opkijken. Last but not least, is er nog mijn 'fabulous' vrouwtje met wie ik alle lief en leed deel. Nina Swinnen, je brengt kleur in mijn leven en je bent mijn rots in de branding. Met jou aan mijn zijde trotseer ik het leven, en bij elke nieuwe stap sta je mij bij. Bedankt, ik hou van je!

Plaudite, amici, comedia finita est